UNIVERSITEIT VAN PRETORIA
UNIVERSITY OF PRETORIA
YUNIBESITHI YA PRETORIA

Discovery and radiopharmaceutical development of probes for prospective positron emission tomography imaging of malaria

by

Janie Duvenhage

Submitted in the partial fulfilment of the requirements for the degree

Philosophiae Doctor in Biochemistry

In the Faculty of Natural and Agricultural Sciences
Department of Biochemistry, Genetics and Microbiology
University of Pretoria
Pretoria
South Africa

22 November 2021

I, Janie Duvenhage, declare that the thesis, which I hereby submit for the degree *Philosophiae Doctor* in the Department of Biochemistry, at the University of Pretoria, is my own work and has not previously been submitted by me for the degree at this or any other tertiary institution.

SIGNATURE:

DATE:

22 November 2021

Plagiarism declaration

University of Pretoria

Faculty of Natural and Agricultural Science

Department of Biochemistry, Genetics and Microbiology

Full names of student: Janie Duvenhage

Student number: 28003960

Title of work: Discovery and radiopharmaceutical development of probes for prospective positron emission tomography imaging of malaria

Declaration

1. I understand what plagiarism is and I am aware of the University‘s policy in this regard.
2. I declare that this thesis is my own original work. Where other people‘s work has been used (either from a printed source, internet or any other source), due acknowledgement was given, and reference was made according to departmental requirements.
3. I did not make use of another student‘s previous work and submit it as my own.
4. I did not allow and will not allow anyone to copy my work with the intention of presenting it as his or her own work.

SIGNATURE STUDENT:

DATE:

22 November 2021

Acknowledgements

First and foremost, I would like to thank our Almighty God for the strength and determination to fulfil my dreams to do this degree. I could never have achieved this without God's endless love, grace, and guidance. Amen.

I would like to thank all my supervisors, Prof. T. Ebenhan, Dr. J. Fehrsen, Prof. JR. Zeevaart and Prof. LM. Birkholtz, for guidance and support during this research. Especially Prof. T. Ebenhan, for the invaluable input on the completion of this thesis. I would wish to thank Dr J. Fehrsen for all the assistance in the laboratory and making me feel welcome at the ARC. I thank Prof. JR. Zeevaart for never stopping in believing in this project. I would like to thank each NuMeRI and Necsa member which have assisted in the animal studies.

I would like to express my sincere gratitude to my family. To my parents, Jan and Marika, thank you for being my biggest supporters, always encouraging me to pursue my dreams in life. Without you, none of this would have been possible. I thank my siblings for all the motivation throughout this degree. A special thanks to my niece, Megan, for supporting me through all the highs and lows; especially at the final stages of this research.

I would wish to thank all my friends for all their support. Fiona and Cathryn, thank you for the encouragement throughout my studies. Cecille, all the phone calls in the morning just to say you are proud of me, has been invaluable. To Jessica, thank you for all your support and patience when I needed to hear "just keep swimming".

I would like to thank Cola for her unconditional love and for always cheering me up when needed. And lastly, special thanks to my fiancé, Jacques, for all the patience, support, and encouragement, but most importantly, for always believing in me.

"Rejoice always, pray continually, give thanks in all circumstances; for this is God's will for you in Christ Jesus"

1 Thessalonians 5:16-18

Summary

Plasmodium falciparum is not only the most predominant human malaria parasite species in Africa but is additionally responsible for causing the most severe cases of the disease. This species' ability to modify the host's erythrocytes not only permits the parasite's survival within the erythrocyte and evasion of the host's immune system, but also results in the manifestation of devastating lethal cases of the disease known as severe malaria. There is a lack in knowledge regarding the molecular mechanisms underlying the pathogenesis of severe malaria, however, research has shown that a major role is played by the sequestration of the altered infected erythrocytes in organs and tissues of the host. Research of severe malaria has relied mostly on post-mortem studies and animal models, both of which lack translatability to the disease in humans in real time.

In vivo imaging is a non-invasive technique that has been used to gain insights into numerous pathologies in real time. Nuclear imaging has been employed clinically to evaluate organ and tissue functionally and track pathophysiology and disease progression at a cellular level. Immuno-PET, in particular, combines the high sensitivity and resolution of PET imaging with the superb target specificity and affinity of monoclonal antibodies, producing functional imaging of the specific target. However, there is a lack of development of malaria-specific tracers due to the complexity of the disease. This underlines the need to develop *P. falciparum*-specific tracers that could be used for immuno-PET imaging and thereby achieve new perceptions into severe malaria.

This doctoral study set out to develop a malaria-specific tracer that would display favourable pharmacokinetic and biodistribution properties for PET imaging. We focussed on developing radiotracer candidates that would be specific for the *P. falciparum*-infected erythrocyte stages that are known to sequester in tissues and cause severe malaria.

Firstly, a *P. falciparum*-specific antibody and antibody fragment were radiolabelled with ^{89}Zr and assessed in healthy mice for their potential for future imaging of malaria. Our efficient radiosynthesis of [^{89}Zr]Zr-Pf-Fab and [^{89}Zr]Zr-IIIB6 allowed further pre-clinical characterisation of the pharmacokinetics and biodistribution of these tracers with PET imaging. The favourable pharmacokinetics of [^{89}Zr]Zr-Pf-Fab further supports PET

imaging studies in malaria-infected mice, and thereby validating whether this radiotracer could be used for further clinical trial investigations.

Additionally, we used phage display technology aiming to discover scFvs specific towards *P. falciparum*-infected erythrocytes. However, this objective was hindered by inadequate detection strategies to verify the specificity of the selected scFv clones to *P. falciparum*-infected erythrocytes .

Furthermore, we focused on ^{68}Ga-radiolabelling of a *P. falciparum*-specific peptide ([^{68}Ga]Ga-DOTA-P1) to evaluate its potential for future *in vivo* imaging or antimalarial drug development. The high-quality radiosynthesis of [^{68}Ga]Ga-DOTA-P1 granted characterisation of this radiotracer in terms of serum stability and erythrocyte binding. Both, selective binding to *P. falciparum*-infected erythrocytes and exquisite serum stability supports future pre-clinical characterisation by way of [^{68}Ga]Ga-DOTA-P1-PET imaging.

The overall findings in this doctoral study demonstrate innovative development of *P. falciparum*-specific radiotracers for prospective *in vivo* imaging in the clinical setting towards better understanding of severe malaria, or future research in drug development.

Table of Contents

List of figures

Chapter 1

Chapter 2

Chapter 3

Chapter 4

List of tables

Chapter 1

Chapter 4

Appendix

List of abbreviations

^{18}F-FDG	2-deoxy-2-[^{18}F]fluoro-D-glucose
AIDS	acquired immune-deficiency syndrome
AKI	acute kidney injury
ALI	acute lung injury
AMA1	apical membrane antigen-1
AP	alkaline phosphatase
APC	activated protein C
ARDS	acute respiratory distress syndrome
ATS	intracellular acidic terminal segment
BLI	bioluminescent imaging
BSA	bovine serum albumin
BT	bench-top
CD36	cluster of differentiation 36
CH	constant domain of heavy chain
CIDR	cysteine rich interdomain regions domains
CL	constant domain of the light chain
CM	cerebral malaria
CR1	complement receptor
CSA	chondroitin sulfate a
CT	computed tomography
CV	cardiovascular
DBL	duffy binding like
DBP	duffy binding protein
DC	domain cassettes
DFO-Bz-NCS	*p*-isothiocyanatobenzyl-desferrioxamine
DOTA	1,4,7,10-tetraazacyclododecane-1,4,7,10-tetraacetic acid
DV	digestive vacuole
EBL-1	erythrocyte binding ligand-1
ECG	electrocardiogram
ECM	experimental cerebral malaria
EEG	electroencephalography
ELISA	enzyme-linked immunosorbent assay

EPCR	endothelial protein c receptor
ER	endoplasmic reticulum
EXP2	export protein 2
Fab	fragment antigen binding
FACS	fluorescence-activated cell sorting
Fc	fragment crystallisable
FDA	Food and Drug Administration
FITC	fluorescein-5-isothiocyanate
FLI	fluorescent imaging
FOV	field of view
Fv	variable fragment
GFP	green fluorescent protein
HEPES	4-(2-hydroxymethyl)-1-piperazineethanesulfonate
HIV	human immune-deficiency virus
HPLC	high performance liquid chromatography
h-R3	nimotuzumab
HRP	horseradish peroxidase
ICAM-1	intercellular adhesion molecule 1
ID	injected dose
IDC	intra erythrocytic developmental cycle
IgG	immunoglobulin type G
IPCIF	Interim Preclinical Imaging Facility
IPTG	isopropyl-thio-β-d-galactosidase
iRBC	infected red blood cells
IVC	individual ventilated cages
IVM	intravital microscopy
KAHRP	knob associated histidine rich protein
LAIR	leukocyte-associated ig-like receptor
LE	labelling efficiency
mAb	monoclonal antibody
MC	Maurer’s cleft
MIP	maximum intensity projections
MRI	magnetic resonance imaging

MSP	merozoite surface protein
Necsa	South African Nuclear Energy Corporation
NHP	non-human primate
NPP	new permeability pathways
NSG	NOD/SCID/IL2Rγ^{null}
NTS	N terminal segment
NWU	North West University
OPD	o-phenylenediamine dihydrochloride
PAM	pregnancy associated malaria
PBS	phosphate buffered saline
PDL	peptide phage display library
PEG	polyethylene glycol
PET	positron emission tomography
PEXEL	*Plasmodium* export element
PfEMP1	*Plasmodium falciparum* erythrocyte protein 1
PM	placental malaria
pNPP	para-nitrophenylphosphate
PPM	parasite plasma membrane
PTEX	*Plasmodium* translocon of exported proteins
PV	parasitophorous vacuole
PVM	parasitophorous vacuole membrane
Radio-HPLC	radioactive high performance liquid chromatography
Radio-iTLC	radioactive instant thin-layer chromatography
RBC	red blood cell
RCP	radiochemical purity
RCY	radiochemical yield
RESA	ring-infected erythrocyte surface antigen
RIFINs	*Plasmodium falciparum*-encoded repetitive interspersed families of polypeptides
SANS	South African National Standards
scFv	single-chain variable fragment
SEC	size exclusion chromatography
SG-iTLC	silica-gel-plated instant thin-layer chromatography

SM	severe malaria
SMA	severe malaria anaemia
SPECT	single-photon emission computerised tomography
SPF	specific pathogen-free
STEVOR	subtelomeric variable open reading frame
SUV	standard uptake value
TAC	time-activity curve
TB	tuberculosis
T-iRBCs	trophozoite- and schizont-infected erythrocytes
TMB	3,3',5,5'-tetramethylbenzidine
TMD	transmembrane domain
TU	transducing units
TVN	tubular vesicular network
UM	uncomplicated malaria
var	variant gene family
VH	variable heavy chains
VL	variable light chains
VOI	volume of interest
VSA	variant surface antigens

Chapter 1

Literature review

1.1 General introduction to malaria

Beyond the discernible morbidity and public health threats of malaria, this disease severely affects the intellectual development and economy of a country and as such is classified as a poverty-related disease. Despite significant progress in the global control of malaria, around 228 million people suffered from this blood-borne, deadly disease in 2018 alone. Of these cases, ~93% occurred in Africa where pregnant women and children were the most severely affected [1-3]. Although the global incidence rate has lessened dramatically over the last 7 years, malaria is still annually responsible for 409 000 deaths worldwide [2].

Malaria is caused by protozoan parasites belonging to the *Plasmodium* genus, of which five species are known to cause the disease in humans: *Plasmodium falciparum, Plasmodium vivax, Plasmodium knowlesi, Plasmodium ovale* and *Plasmodium malariae* [4, 5]. *P. falciparum* is predominant of the five species and causes the most severe cases of the disease leading to more than 90% of all human malaria cases in Africa [6].

1.2 *P. falciparum*

1.2.1 The life cycle of *P. falciparum*

P. falciparum has a complex life cycle where the parasite uses an *Anopheles* mosquito as a vector to transmit itself to the human host (Figure 1.1). During a blood meal, sporozoites are injected into the human host as part of the anticoagulation bolus secreted by the feeding mosquito [7]. These sporozoites rapidly migrate to the liver where they enter the pre-erythrocytic stages. During this stage, sporozoites differentiate and multiply asexually to form up to 30 000 daughter merozoites [8]. Infected hepatocytes then rupture releasing these motile merozoites into the blood stream where they rapidly invade host erythrocytes to initiate the exponential formation of new parasites during the asexual intra-erythrocytic developmental cycle (IDC).

During the 48 h IDC, the parasites develop through ring, trophozoite and schizont stages by biochemical and metabolic maturation [9]. The ring-stage parasite matures into metabolically active trophozoites. Sequential nuclear divisions signal schizogony, a process that produces multi-nucleated schizonts, each consisting of up to 36 daughter merozoites. The merozoites are released when the host erythrocyte ruptures and in turn re-invade erythrocytes and re-initiate the IDC, leading to exponential increase of parasitaemia in the host [10, 11]. A small proportion of these asexual parasites (<10%) undergo gametocytogenesis to develop into sexual blood stages (either male or female gametocytes) [12]. During gametocytogenesis, the *P. falciparum* parasite takes 10-14 days (post erythrocyte invasion) to develop through five morphologically distinct stages (I-V) [13]. The immature gametocyte stages (stage I-IV) sequester in the bone marrow and are absent from blood circulation while they mature [14]. Only mature (stage V) gametocytes are released into the peripheral circulation where they can be ingested by a mosquito when it feeds on a human host [12, 15]. After the uptake of the gametocytes by the mosquito, the change in microenvironment (a drop in temperature, increase in pH and exposure to xanthurenic acid) stimulates the activation of gametogenesis where male gametocytes form microgametes and female gametocytes form macrogametes [16]. In the mosquito's midgut, a microgamete and macrogamete from different hosts fuse to form a diploid zygote [16]. The zygote undergoes meiosis and transforms into an ookinete, which is motile and migrates to the mosquito's midgut wall where it subsequently matures into an oocyst [17, 18]. The oocyst undergoes several mitotic divisions producing multiple sporozoites, the infectious stage of the parasite, that subsequently migrate to the mosquito's salivary glands for injection into the human host [19].

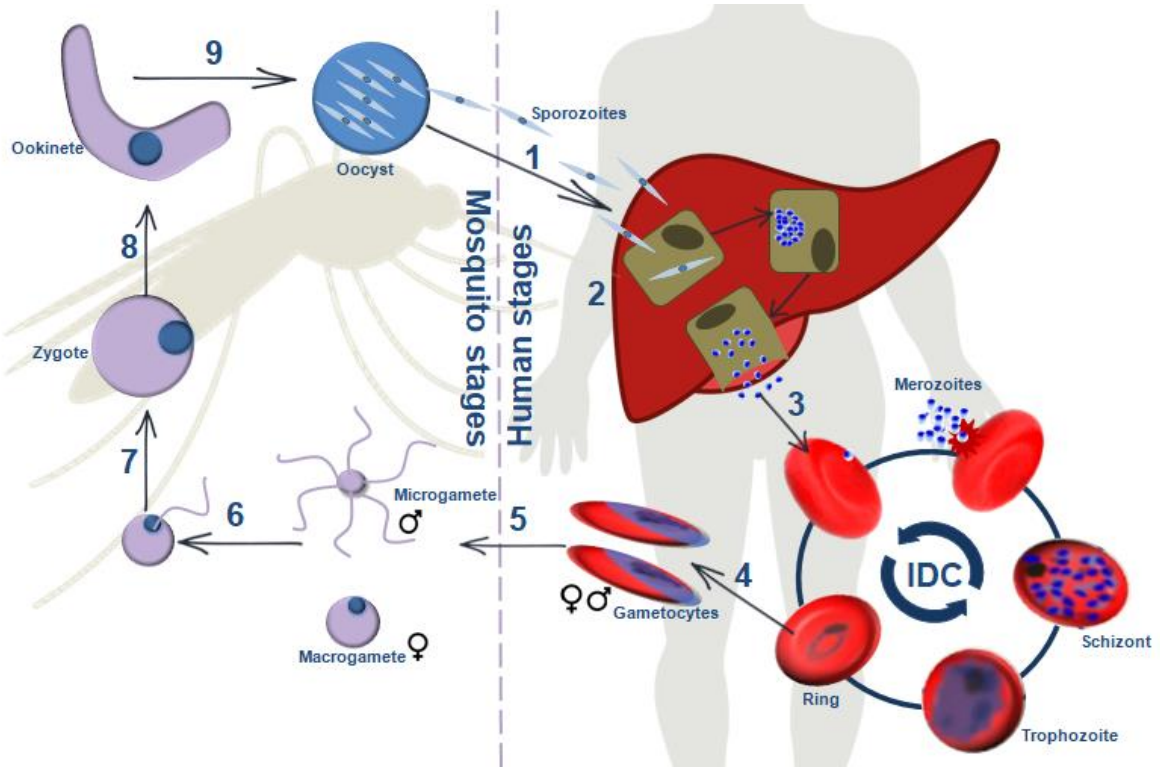

Figure 1.1. The life cycle of *P. falciparum*. A female *Anopheles* mosquito bites and injects the *P. falciparum* sporozoites into the human host (1). The sporozoites travel in the blood stream to the liver where they infect liver cells and mature into merozoites (2). The liver cell bursts and releases merozoites into the blood stream which then infect erythrocytes (3) to initiate the asexual intra-erythrocytic development cycle (IDC). During the asexual cycle, the parasite develops into rings, trophozoites and schizonts. Schizonts will then cause the erythrocyte to rupture and release multiple merozoites again into the bloodstream. A small proportion of schizonts commit to enter the sexual developmental cycle and gametocytogenesis is initiated where stage I-V gametocytes will form (4). Mature male and female stage V gametocytes will be taken up by a mosquito when it feeds on the human host and develop into a macrogamete and microgamete respectively (5) that fuse with each other (6) to form a zygote (7). The zygote transforms into an ookinete (8) which travels to the midgut of the mosquito and matures into oocyst (9). The oocyst produces sporozoites (9) which can then be injected into the human host, starting the cycle again.

1.2.2 An introduction to the clinical manifestations of *P. falciparum* malaria

P. falciparum parasite infections present clinically as either uncomplicated malaria (UM) or severe malaria (SM). The pathophysiology of malaria is induced as soon as the schizont-infected erythrocyte ruptures to release merozoites. This leads to the manifestation of the initial clinical flu-like symptoms including fever, headaches, muscle aches, dry cough, nausea and vomiting [20, 21]. UM is defined when only these typical flu-like symptoms occur in the presence of asexual blood-stage parasites. If the patient is non-immune and/or left untreated, UM can develop into a lethal multisystem disease – severe malaria (Figure 1.2). SM is mostly associated with *P.*

falciparum infections where the asexual IDC is responsible for the pathogenicity and severity of the disease [1]. Classification of SM is when the influenza-based symptoms occurs in combination with other features associated with the risk of death [22]. Once SM develops, the case-fatality rate increases dramatically despite malaria treatment [23]. The severity of malaria depends on a number of factors including the state of immunity, age, general health and nutritional status of the patient [24, 25]. SM usually affects the hosts' organs and can lead to serious complications and disease syndromes including cerebral malaria (CM), severe malarial anaemia (SMA), metabolic acidosis, pregnancy associated malaria (PAM), acute respiratory distress syndrome (ARDS), acute lung injury (ALI), pulmonary oedema, placental malaria (PM), cardiac shock, acute kidney injury (AKI) and jaundice [24, 26, 27].

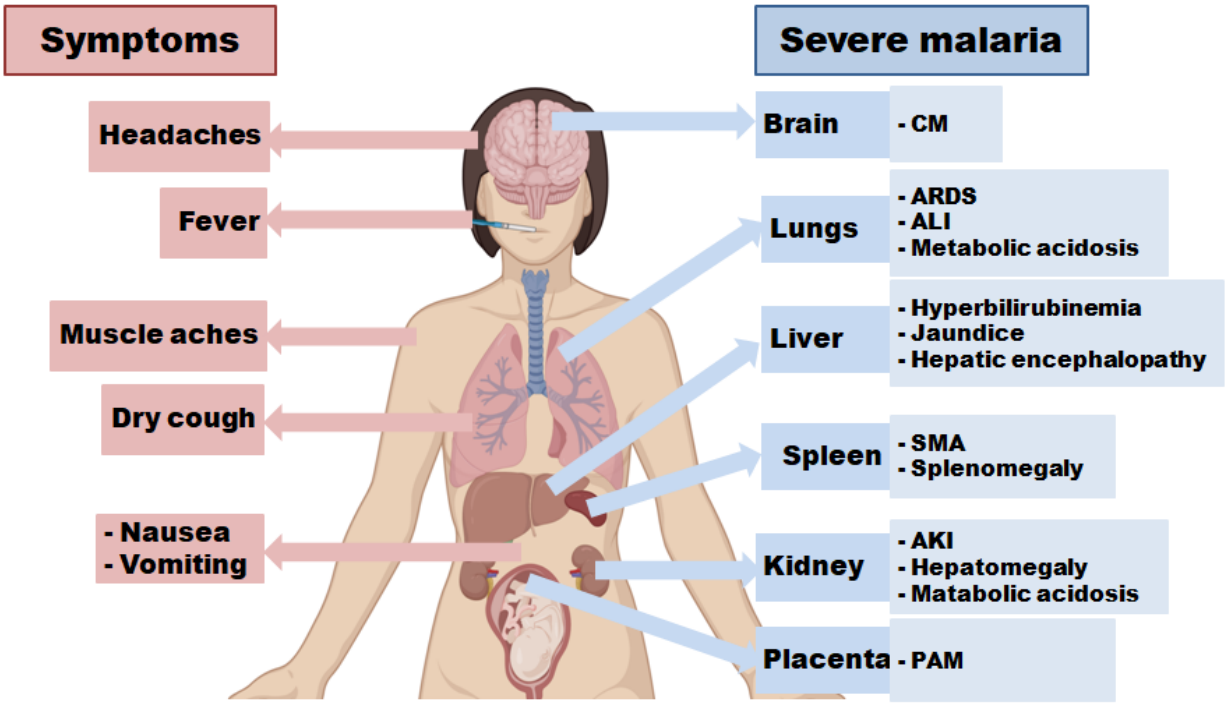

Figure 1.2. Predictive symptoms and severe malaria complications following infection with *P. falciparum* parasites. Cerebral malaria (CM); acute respiratory distress syndrome (ARDS); acute lung injury (ALI); severe malaria anaemia (SMA); acute kidney injury (AKI); pregnancy associated malaria (PAM). Created with BioRender.com.

The pathogenesis of SMA is multifactorial with one of the most common complications of SM, which occurs mostly in children and pregnant women [28]. Malaria anaemia develops via three mechanisms: 1) intravascular haemolysis, 2) clearance of parasite-infected erythrocytes and 3) dysregulated erythropoiesis leading to reduced erythrocyte production [29]. The destruction of infected erythrocytes at schizont

rupture accounts for only a small fraction of red blood cell loss. Rather, uninfected erythrocytes haemolysis and reduced erythropoiesis are the principal contributors to anaemia [30-32]. It has been found that, in the presence of infected erythrocytes, uninfected erythrocytes also get eliminated due to various suggested mechanisms [33-36]. This loss of the erythrocytes serves as a major contributor (~90%) in the development of SMA [37, 38]. Furthermore, *P. falciparum* infections cause dyserythropoiesis (defective development of erythrocytes) which further reduces erythrocyte production [28, 32, 39, 40].

CM is characterised as SM complicated with seizures and coma that are not associated with convulsions, other medication, hypoglycaemia or any non-malarial disease [41]. CM is a life-threatening complication caused by *P. falciparum* infection that leads to coma, retinal changes, multi-organ failure, bleeding disorders, brain swelling and other complications. CM is responsible for ~20% of adult and ~15% child mortalities from *P. falciparum* parasite infection [29]. More than 25% of CM survivors usually develop life-long neurological sequelae, including sensory and cognitive impairment, leading to a reduced quality of life [42, 43]. During CM, the blood brain barrier is disrupted, giving rise to neurological complications (including intracerebral haemorrhage, seizures and increased intracranial pressure due to oedema) that ultimately leads to central nervous system dysfunction and death [44]. The development of CM is complex and multiple events are associated with the pathology including microvascular obstruction of infected erythrocytes, extreme pro-inflammatory cytokine production, microvascular thrombosis, loss of endothelial barrier function and endothelial dysregulation [45]. However, it remains unclear how all these factors are linked to the development of CM and studies of CM in humans have mostly been limited to clinical observations and post-mortem evaluations.

AKI develops in ~40% of malaria patients [37]. High parasite biomass causes stress to the kidneys in multiple ways. Parasite-related lactic acidosis leads to the clinical manifestations of metabolic acidosis [46]. The sequestration of infected erythrocytes and rosetting of erythrocytes in the blood vessels of the kidney, cause hypoxia. Sequestration furthermore leads to the build-up of parasite-related toxic products in the endothelial lining of the kidney which follows with endothelial damage and immune reactions. All these factors eventually lead to kidney failure.

Respiratory distress is frequently found in patients with *P. falciparum* SM. Two causes for this clinical syndrome include ARDS and pulmonary oedema. ARDS is characterised by severe hypoxia that leads to vascular permeability which causes pleural effusion, lung enlargement and reduces aerated lung tissue [47]. ARDS can develop late in the disease, even after anti-malarial treatment. The cause of ARDS is still poorly understood but involves accumulation of monocytes and macrophages in the lung alveoli that eventually leads to lung inflammation with alveolar damage [48]. Treatment of a patient with AKI involves fluid administration, however, this excessive intravenous fluid is linked to the development of pulmonary oedema [37].

During pregnancy, the concentration of parasite-infected erythrocytes in the placenta severely affects the mother and infant leading to PAM. The mother develops anaemia which can lead to maternal death. This sequestration interferes with nutrient and oxygen transportation through the placenta to the foetus, resulting in retarded foetal growth and the potential for premature delivery, low birth weight or foetal loss [49].

Cardiac effects associated with *P. falciparum* infections include myocarditis, pericarditis, ischemic disease, pericardial effusion and heart failure [50]. Although the mechanisms underlying cardiovascular (CV) complications are complex and incompletely understood, multiple factors can be involved such as mechanical mechanisms involving microvasculature obstruction, pro-inflammatory cytokine response, endothelial dysfunction, metabolic effects like systematic acidosis or tissue hypoxemia, and/or humoral mechanisms.

Survivors of SM often suffer from neurologic and cognitive impairment [51]. Factors leading to SM are complex and multifactorial owing to characteristics of both the parasite and the human host and therefore, the malaria parasite and/or host-mediated interactions, along with underlying mechanisms involved in pathophysiology of SM, remain poorly understood [21, 42]. However, it has been proven that the parasite has a unique ability to remodel the host erythrocyte in a way that promotes erythrocyte adherence to the endothelial lining of tissues and organs (sequestration), and it is this characteristic that is predominantly associated with SM.

1.3 Remodelling of the host erythrocytes

1.3.1 Remodelling for survival within the host erythrocyte

As soon as the merozoite has invaded the erythrocyte, the parasite starts remodelling the erythrocyte host as part of both a survival strategy and to provide an environment that would enable parasite functionality and multiplication (Figure 1.3) [52, 53]. Firstly, during the invasion step, the parasitophorous vacuole (PV) is formed as a compartment in which the parasite resides. The parasitophorous vacuole membrane (PVM), the barrier between the erythrocyte cytosol and parasite, surrounds the PV and fulfils key functions for parasite survival [54-56].

During the asexual IDC, the parasite is dependant of the host's supply of nutrients to support growth and division. The host erythrocyte only contains haemoglobin, a limited source of some amino acids, and therefore cannot alone meet the parasite's high nutritional demand [57]. During the IDC, the parasite takes up large quantities of the host erythrocyte's cytosol through invagination of the PVM and the parasite plasma membrane (PPM). The contents of these double-membrane structures, known as cytosomes and phagotrophs, are transported to the parasite's digestive vacuole (DV) [57]. In the DV, a large amount of haemoglobin is metabolised to supply the parasite with amino acids, maintain osmotic homeostasis and to increase the intracellular space for parasite growth [58-61]. During haemoglobin digestion, large quantities of free ferric haem are released, which are toxic to the parasite due to its membrane-disruptive and lytic effects. The parasite detoxifies the free haem by crystallizing it into β-hematin that is non-toxic to the parasite [62]. The parasite consequently reconstructs the host cell to permit the acquisition of necessary extracellular nutrients and disposal of metabolic waste across several membranes. The erythrocyte does not have any intracellular organelles, no protein synthesis capability and lacks protein trafficking machinery. The parasite therefore establishes a system that allows the correct transport of effector parasite-specific proteins to the erythrocyte compartment essential for parasite viability and virulence [63]. There have been numerous studies that identified and characterized some of these parasite-specific proteins and their functions vary but include nutrient exchange and evading the host's immune system [64]. The creation of new permeability pathways (NPP) facilitates the transport of most low molecular solutes from the blood plasma into the erythrocyte and disposal of toxic

metabolites to the extracellular space [65]. Following entrance into the erythrocyte cytosol, the nutrients must still cross the PVM and the parasite plasma membrane (PPM). Nutrient permeable channels, such as export protein 2 (EXP2), allow the nutrients to cross the PVM into the parasite vacuole. In turn, PPM transporters allow the final crossing of nutrients into the parasite cytosol [66].

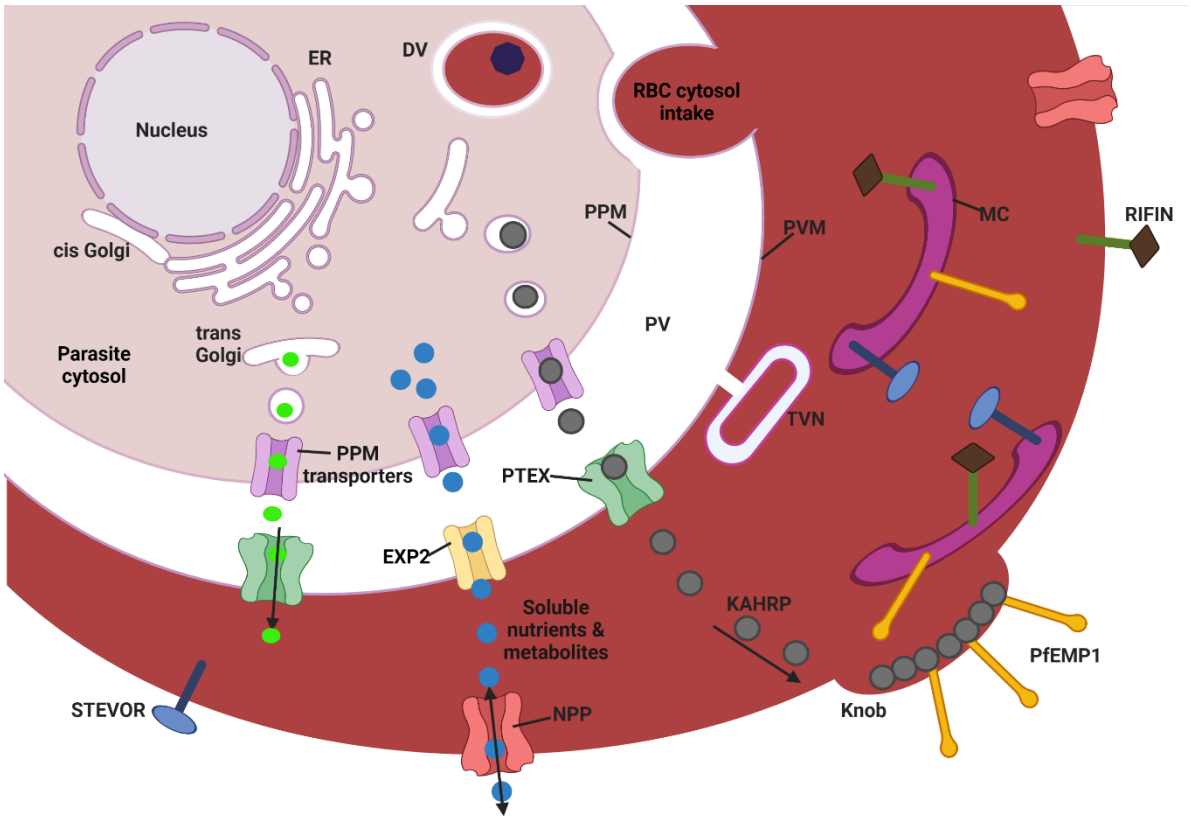

Figure 1.3. Remodelling of the erythrocyte by *P. falciparum* parasites. Endoplasmic reticulum (ER); digestive vacuole (DV); parasitophorous vacuole (PV); parasitophorous vacuolar membrane (PVM); parasite plasma membrane (PPM); Maurer's cleft (MC); tubular vesicular network (TVN); *Plasmodium falciparum* erythrocyte protein 1 (PfEMP1); subteleomeric variant open reading frame (STEVOR); *Plasmodium falciparum*-encoded repetitive interspersed families of polypeptides (RIFINs); knob associated histidine rich protein (KAHRP); new permeability pathways (NPP); *Plasmodium* export element (PEXEL); *Plasmodium* translocon of exported proteins (PTEX); red blood cell (RBC), exported protein 2 (EXP2). Created with BioRender.com

Proteins destined to be exported into the host cell undergo vesicle-mediated transport by firstly becoming inserted in the parasite endoplasmic reticulum (ER), which then transfers them to the Golgi apparatus where the trans-Golgi later transfers these proteins into the PVM [67]. These proteins contain a *Plasmodium* export element (PEXEL), a pentameric motif that acts as a targeting signal peptide for ER entry. The PVM contains a protein complex, the *Plasmodium* translocon of exported proteins (PTEX), that governs the transport of parasite-specific proteins across the PVM [68].

Because the erythrocyte does not contain secretory pathways, the parasite develops an exomembrane system to regulate protein transport in the cytoplasm of the erythrocyte [69]. This includes membrane cisternae, known as Maurer's cleft (MC), and a tubulovesicular network. The MC serves as an intermediate destination of proteins where proteins are sorted and then routed to the erythrocyte plasma membrane [63].

Parasite-derived proteins that interact and associate with the cytoskeleton of the host cell are mainly involved in cytoadherence, promoting erythrocyte rigidity and increasing the permeability of the erythrocyte's membrane. Proteins that allow adherence of the infected erythrocyte to the microvasculature of certain tissue enable the parasite to evade the host immune system and avoid splenic filtration. Knob associated histidine rich protein (KAHRP), present on the cytoplasmic side of the erythrocyte plasma membrane, induces raised points on the erythrocyte membrane known as knobs [70]. These knobs serve as platforms in which parasite-specific proteins are displayed on the surface of erythrocytes [70, 71].

1.3.2 Remodelling for evasion of the host immune system

Sequestration and cytoadherence

Most erythrocyte modifications occur in the trophozoite and the schizont stages. These infected erythrocytes show decreased membrane deformability as well as becoming spherical and less flexible. The spleen is able to sense these defective erythrocytes and would consequently eliminate them via the macrophage phagocytic system as they cannot pass through the inter-endothelial slits of the sinuses of this organ [25, 72]. However, the parasite has developed a spleen evading mechanism. Some parasite-specific proteins, exported and expressed on the erythrocyte cytoskeleton, allow the late-stage asexual parasites (trophozoite and schizont stages) to adhere to the microvasculature of organs and tissues (sequestration), as well as to uninfected erythrocytes (rosetting), platelets (agglutination) and other infected erythrocytes (clumping) (Figure 1.4), and thereby evade filtering by the spleen.

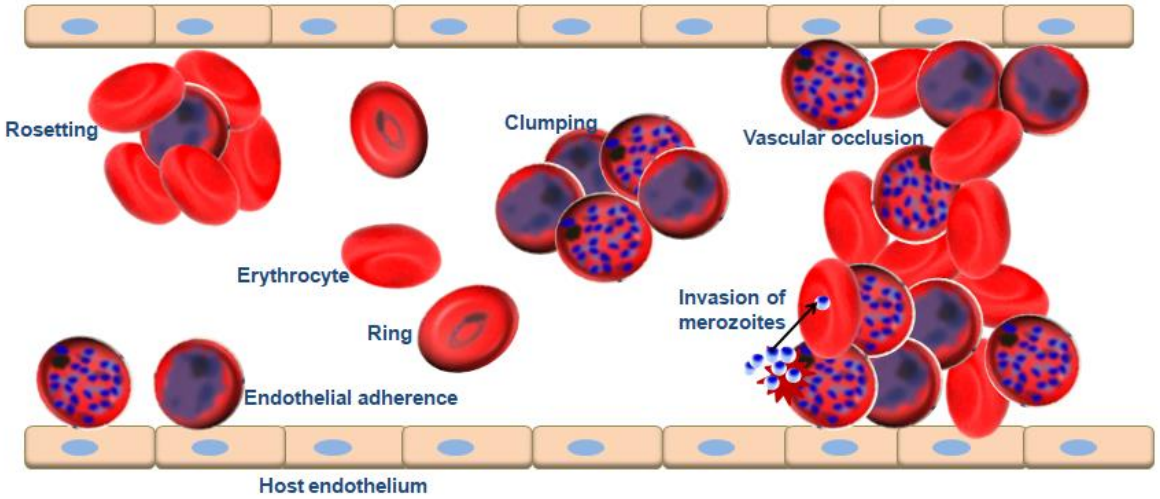

Figure 1.4. Schematic representation of possible outcomes of erythrocyte remodelling by *P. falciparum*. The parasite expresses proteins on the infected erythrocyte membrane that allow the parasite to survive in the host. This antigen expression can result in mature *P. falciparum*-infected erythrocytes undergoing: 1) adherence to uninfected erythrocytes by rosetting; 2) adherence to infected erythrocytes through clumping; 3) cytoadherence to tissue endothelial lining and eventually 4) vascular occlusion that obstructs blood flow. Rosetting also provides a favorable environment for newly released merozoites to invade uninfected erythrocytes. However, ring-infected erythrocytes remain unbound circulation. Input for this figure was obtained from previous publications [73-75].

Three major families of proteins known as variant surface antigens (VSA), contribute to adherence of infected erythrocytes and hence host immune system evasion. They include *P. falciparum* erythrocyte protein 1 (PfEMP1), subtelomeric variable open reading frame (STEVOR) and *P. falciparum*-encoded repetitive interspersed families of polypeptides (RIFINs) (Figure 1.3) [75]. The PfEMP1 family members are the largest contributor to sequestration of asexual blood stage parasites [76]. This protein is expressed on the surface erythrocytes infected by the late-stage parasites. PfEMP1 has been found to bind to more than 12 host receptors including intercellular adhesion molecule 1 (ICAM-1), complement receptor 1 (CR1), chrondroitin sulfate A (CSA), cluster of differentiation 36 (CD36) and endothelial protein C receptor (EPCR) [1, 75, 77]. RIFINs, expressed on the surface of infected erythrocytes, bind to other erythrocytes to mediate microvascular binding of the infected erythrocytes [78]. STEVORs also promote rosetting, independent from PfEMP1, through binding to glycophorin C on the surface of erythrocytes. In this way, STEVORs also protect released merozoites from immune detection [79]. Infected erythrocyte deformability due to STEVORs is believed to contribute to the adherence of immature gametocytes in bone marrow, protecting them from the immune system until they are mature [80, 81].

Antigenic variation

Although these adhesion proteins prevent parasite elimination by the spleen, they are displayed on the surface of the infected erythrocyte and can therefore be recognised by the host's adaptive immune system and potentially be targeted by specific antibodies. The challenge for the host immune system, however, is that these proteins are encoded by multigene families that ensure antigenic variation through every life cycle, thus providing the parasite with another protective mechanism by which to evade host immunity.

PfEMP1 is the most well-characterized surface proteins that distinguishes *P. falciparum* from the other malaria-casing parasite species [63]. It is encoded by *var* genes, of which the *P. falciparum* genome contains ~60 *var* genes [82]. Each individual parasite expresses a single *var* gene at a time while the other *var* genes are transcriptionally silenced [83]. This antigenic switching between *var* gene expression facilitates evasion of the host's immune system and therefore also allows the sexual stages to develop [84, 85]. The RIFIN proteins are the largest family of VSAs in *P. falciparum* and are encoded by the *rif* gene family consisting of ~150 members [86]. RIFINs are expressed in the intraerythrocytic asexual and gametocyte stages of the life cycle [86, 87]. Some RIFINs assist in the parasite's immune evasion mechanisms by inhibiting the activation of B cells and natural killer cells through interactions with leukocyte-associated immunoglobulin-like receptor (LAIR)-B1 [88]. STEVOR proteins form the third largest multigene family of VSAs, encoded by ~40 *stevor* genes. STEVORs are expressed in numerous stages including merozoites, sporozoite and gametocytes [79, 89].

1.4 Approaches to study and diagnose SM

Delayed treatment of uncomplicated malaria often leads to the death as a result of the development of SM. However, studies have shown that mortality decreases significantly with improving diagnosis and treatment coverage [90]. Although current rapid diagnostic tests are unable to diagnose SM, there are several tools have been developed for researchers and clinicians to diagnose and better understand the single syndromes associated with SM [91-93]. In the case of CM, retinal changes have proven to be an observable marker to distinguish disease severity [94, 95]. There are multiple medical imaging approaches to study malaria retinopathy (e.g., fundoscopy,

optical coherence tomography, teleophthalmology and fluorescein angiogram framework) and these methods are available for clinicians in endemic areas [45]. Electroencephalography (EEG) and micro-EEG are used to detect delayed sequelae of CM including neurological disabilities and subclinical seizures [45]. The involvement of CV symptoms in SM can be assessed through electrocardiogram (ECG), X-rays, echocardiography and the presence of cardiac enzymes. However, it has been reported that in some cases CV complications are unrecognised or under-reported due to the overlap with other fatal complications [50]. There are several routine laboratory markers for single syndromes, however, these do not always predict the severity of the disease as SM includes multi-factorial processes that can be present simultaneously [96]. It is therefore imperative to develop a technique that would permit the simultaneous investigation of the multiple syndromes and complications associated with SM *in situ*. This could allow improved early detection of cases that are likely to develop into SM, which would ensure immediate treatment and decrease the probability of death or the development of long-term sequelae in SM survivors [97]. Additionally, this would also expand our knowledge on the molecular basis of malaria pathogenesis which will, in turn, contribute to improved current therapies and development of new drugs that can reduce the life-threatening complications of SM.

One possible approach that could assist with better understanding of SM entails non-invasive imaging techniques to visualise malaria infections *in vivo* and to observe the intricate host-parasite mechanisms that govern malaria pathogenicity *in situ*. In the clinical setting, *in vivo* imaging allows to repeatedly capture the disease in real time and has helped to obtain unique insights into numerous disorders and pathologies [98]. It is therefore plausible to suggest real-time *in vivo* imaging for the study of malaria, to reveal the mechanisms behind malaria pathophysiology and aid in early diagnosis of SM.

1.5 *In vivo* imaging

In vivo imaging allows for non-invasive and quantitative evaluation of organs, tissues, or cells at a molecular level in real time, providing a major advantage over other imaging techniques (e.g., histology and microscopy). *In vivo* molecular imaging has been a particularly successful method for studying the progression of a disease as well as monitoring any response to therapeutic treatments. It is one of the desired,

very accurate applications in oncology and was recently also shown to have huge potential for studying infectious diseases [98].

While there are different modalities of *in vivo* imaging, each technique has its own advantages and limitations regarding image resolutions, sensitivity, tissue penetration depth, detection threshold of the probes and contrast quantification (Table 1) [99-101]. Additionally, each individual imaging modality has its own characteristics. The choice of imaging modality depends on the type of data sought in a study (i.e., functional processes, biochemical mechanisms or biological objects and tissues) and the resources available. Anatomy-based imaging techniques mainly provide structural details (i.e., soft tissue analysis and blood flow imaging foetal development etc.) while functional imaging (nuclear imaging) grants insight into biological behaviours.

Available diagnostic imaging techniques include X-ray, computed tomography (CT), magnetic resonance imaging (MRI), nuclear imaging (positron emission tomography (PET) and single-photon emission computerised tomography (SPECT)), optical imaging (bioluminescent (BLI) and fluorescent (FLI)) and ultrasound imaging [101, 102].

Structural or anatomical imaging (mainly achieved by MRI and CT) is a reliable technique that provides quality images of particularly soft and/or bony tissues. CT relies on the ability of certain tissue types to absorb X-rays when a low energy X-ray source is directed towards the region of interest, resulting in high anatomical resolution three-dimensional (3D) images of the subject. This modality is relatively cheap, provides rapid readout, and is easy to use, however, one major pitfall is the higher amount of radiation that the patient is exposed to for the duration of the image acquisition [103]. MRI allows visualization of anatomy and physiological processes in the body without radiation exposure. Even though MRI is the best imaging technique for soft tissue imaging, it has its own disadvantages such as rather long scanning times required, a loud noise and small space inside the MRI scanner that may become problematic for some individuals (e.g., people suffering from claustrophobia), and also the incapability to use it on patients with metal implants [104].

Table 1. Most common *in vivo* imaging techniques

Imaging technique	Imaging modality	Sensitivity (mol/L)	Depth	3D Image
Anatomical imaging	MRI	10^{-3} - 10^{-5}	unlimitted	+
	CT	10^{-2} - 10^{-3}	unlimited	+
Optical imaging	FLI	10^{-9} - 10^{-12}	1-10 cm	-
	BLI	10^{-15} - 10^{-17}	1-10 cm	-
Nuclear imaging	PET	10^{-11} - 10^{-12}	unlimited	+
	SPECT	10^{-10} - 10^{-11}	unlimited	+

Footnotes: Three-dimensional (3D); X-radiation (X-ray); computed tomography (CT); magnetic resonance imaging (MRI); positron emission tomography (PET); single-photon emission computerised tomography (SPECT); bioluminescent imaging (BLI); fluorescent imaging (FLI); capable (+); incapable (-).

Optical imaging relies on the detection of light or photons emitted from cells or tissues (either directly through bioluminescence or indirectly through a fluorescent compound) to produce an image. This imaging modality is easy to use, versatile, accurate, sensitive, and cost effective when compared to other imaging techniques. The two main types of optical imaging are FLI and BLI. BLI involves the use of luciferase-expressing cell lines that catalyse the oxidation of a luminogenic substrate (such as D-luciferin), yielding photons of light from within the body that can be detected in real time [105, 106]. The applications of BLI include studying diseases and their potential treatments, and monitoring tumour growth in xenograft models and transgenic animals models [107, 108]. The application of BLI is limited to non-human study subjects, as it requires the injection of genetically modified parasites and exposure of these parasites to luciferin to produce the light-emission for image preparation. Fluorophores for FLI can be either free (unconjugated), conjugates of fluorescent dyes (e.g., green fluorescent protein, GFP) to targeting molecules or fluorescently expressed in

infectious cells (e.g., near-infrared parasite strains), allowing imaging of cancers and infectious diseases [109-111]. Additionally, FLI has been used in multiple surgery applications (fluorescence-guided surgery) including sentinel lymph node mapping, solid tumour identification, lymphography, angiography, anatomical imaging, blood flow imaging, tissue perfusion, plastic surgery, and reconstructive surgery [112]. The main challenge of real-time optical imaging includes limitations in penetration depth and autofluorescence, however, tissues can still be analysed *ex vivo* when dissected *post-mortem* [102, 103, 113].

On the other hand, nuclear imaging uses small amounts of radioactive molecules attached to a compound that targets a specific body part/cell of interest, thereby allowing the study of the functions of the target site [114]. These techniques are employed clinically in the field of nuclear medicine to evaluate organ and tissue functionality and allows early detection/diagnosis of a disease. The most sensitive and specific nuclear imaging techniques include PET and SPECT, both providing functional imaging data that often complement the data produced by MRI and CT [114-116].

PET is the arguably the most advanced nuclear imaging modality with outstanding sensitivity and unlimited penetration depth. Certain radioisotopes emit positrons by the nucleus after which the positrons pair with electrons and the pair annihilates and converts all the mass energy into two photons [117]. The PET imaging acquisition is based on detection of the annihilation photons (511 keV) from the radionuclides (attached to the vector) that accumulates in a tissue or cell of interest [115]. Radionuclides are unstable isotopes of a particular element that undergo radioactive decay by emitting α or β particles, γ rays and Auger electrons, some of which can be utilized in medicine when they form part of a tracer (e.g., radionuclides bound to a biological molecule to enable uptake by the physiological process of interest).

Historically, PET was only used to perform cardiac studies and to detect brain disorders but with the increasing development of new tracers, nuclear imaging now forms an integral part of oncology and also, more recently, in infectious disease studies. PET has particularly been used to better understanding of tuberculosis (TB) infections as well as during the clinical evaluation of human immunodeficiency virus/acquired immunodeficiency syndrome (HIV/AIDS) [118, 119]. PET is capable of

detecting minimal concentrations of a tracer molecule inside the body (Table 1). This technique is therefore more sensitive compared to CT or MRI scans and allows for the visualisation of specific infected areas. Additionally, advantages of this method include the ability to evaluate the whole body of the patient for the extent and progression of the disease, allow the early detection of disease reoccurrence, the evaluation of treatment efficiency to assist in drug development, and the selection of regions for biopsy to enable pre-surgical planning.

SPECT imaging relies on radioisotopes that emits a single photon (a single gamma ray) as a result of radioactive decay [120]. SPECT imaging is more readily available than PET imaging mostly because SPECT imaging is a cheaper modality. However, SPECT does have a lower resolution due to artifacts and attenuation, requires longer scanning times and is less sensitive compared to PET [121].

1.5.1 *In vivo* imaging modalities in malaria

Intravital microscopy (IVM) has been used to image the entrance of sporozoites of the murine malaria parasite *Plasmodium berghei* into the skin and lymph nodes, the development of the parasite in the skin, traversal of the liver parenchyma by these sporozoites and hepatocyte-derived merosome formation that ensures migration and release of the merozoites into the blood stream [122-124]. IVM of murine microcirculation were able to indicate points of blood flow obstruction due to the adhesion of *P. berghei*-infected erythrocytes and leukocytes to capillaries [125]. IVM of transgenic *Plasmodium yoelii* (another murine parasite causing self-limiting parasitaemias) expressing GFP, has been useful in imaging the passage of these parasites through the spleen of murine models [126]. Through *in vivo* imaging, the authors were able to report remodelling of the spleen and adherence of infected erythrocytes in the red pulp during infection.

Optical imaging featuring transgenic BLI and FLI, has been utilized to study and to better understand cellular processes related to malaria infections [127, 128]. These genetically engineered parasite lines have allowed scientists to understand some biological aspects of the parasite that were previously unknown and have played an essential role in the development of drugs. *P. falciparum* and *P. berghei* parasites have been engineered to express bioluminescent reporters in most developmental stages of the parasite's life cycle [129]. *P. berghei* luciferase-expressing sporozoites have

been used to obtain real-time images of the administration and development and testing of drugs that target the liver stages [127, 130, 131]. Additionally, luciferase-expressing *P. berghei* parasites have permitted sensitive *in vivo* screening of drugs against asexual parasites [132]. Furthermore, luciferase-expressing *P. berghei* have allowed real-time BLI of the sequestration patterns in mouse models [133]. Transgenic parasites have also been used in vaccine development to examine efficacy and immune responses *in vivo* [134]. Although rodent malaria has provided vital information about malaria infection, there remains key differences between rodent and human malaria. This has inspired the development of transgenic rodent malaria parasites that expresses human malaria proteins. These parasite lines have been used to assess candidate vaccines and anti-malaria drugs [135]. Luciferase-expressing *P. falciparum* parasites in liver- and blood-humanised mice have allowed study of the biology of the *P. falciparum* liver stages, the transition to blood stages and the development of asexual parasites [136]. This model has the potential for use in the development of treatments for pre-erythrocytic and erythrocytic stages as it allows the intravital imaging of these two stages independently.

CT and MRI have been considered for use in clinical settings to study CM-related changes in brain tissue. Although CT scans have shown that some CM patients show brain swelling, this imaging modality lacks the ability to distinguish vasogenic oedema from cytotoxic oedema, for example [137-139]. MRI techniques have allowed for the diagnosis of CM, the visualisation of vascular damage arising from inflammatory processes, analysis of neuron axon injury, endothelial dysfunction, viewing of areas of blood brain barrier dysfunction, blood flow obstruction and swelling of the brain stem [37, 91, 140]. CT scans have been able to identify splenomegaly (an abnormal enlargement of the spleen) and splenic infarction induced by malaria [141-144]. Karakas *et al*. (2005) were able to show the abnormal enhancement of malarial splenic parenchyma and markable differences in blood flow between the white and red pulp in malaria infections [145].

X-ray, CT, ultrasonography and PET imaging are standard imaging techniques used for the identification of ARDS [47]. SPECT/CT have also been used to study malaria-ARDS, highlighting the ability for SPECT/CT imaging to allow early diagnosis in malaria-associated ARDS in *P. berghei*-infected mice [47]. However, pulmonary

complications arising from malaria can be misdiagnosed as another respiratory disease [146].

In nuclear medicine, 2-deoxy-2-[^{18}F]fluoro-D-glucose-PET ([^{18}F]FDG-PET) has been used to study malaria in non-human primates (NHP) infected with *P. coatneyi* [147, 148]. The one study utilized [^{18}F]FDG-PET scans of infected Japanese macaques to show an evident splenic tracer uptake due to the enhanced glucose metabolism present in this organ as a result of infection (Figure 1.5). Along with autopsy and histopathologic findings, the authors suggested that this vast increase in glucose metabolism in the spleen could result from the activation of the splenic clearance system towards infected erythrocytes [147]. Another study that focused on CM indicated a reduction in glucose metabolism in the cerebral cortex with the basal ganglia almost unchanged in the case of acute infection (Figure 1.5). Along with neuropathologic examination, the authors suggested that this decrease in glucose metabolism occurred before parenchymal brain changes appeared and was possibly due to a reduction in energy metabolism in an effort to reduce brain damage [148].

Recently, a human exploratory study was performed using [^{18}F]FDG-PET/MRI to study the differences between *P. vivax* and *P. falciparum* in experimentally induced infection [149]. In this study, marked differences were found between *P. vivax* and *P. falciparum* infections with glucose metabolism most pronounced in *P. vivax* infection. This study demonstrated that PET/MRI offers the possibility to define organ-specific physiological changes. A limitation of using [^{18}F]FDG to study malaria infections, is that it is not specific for malaria and other infections or diseases (e.g., tumours or inflammatory and infectious tissues) will also accumulate [^{18}F]FDG. Hence, this unspecific [^{18}F]FDG uptake may cause false-positive or false-negative diagnosis when used for malaria infection studies and thus, improvements are needed to increase the specificity of the technology to distinguish and study only sequestered malaria parasites. Direct radiolabelling of *P. falciparum*-infected erythrocytes with technetium-99m has been done to study sequestration of parasite-infected erythrocytes in rats [150]. The main finding of the study, revealed through *in vivo* imaging and *in vitro* binding studies, indicated sequestration of infected erythrocytes in the lungs of the rats. However, labelling the infected erythrocyte itself limited the study to only allow investigation of sequestration of the initial injected erythrocytes since any infected erythrocytes after asexual replication would not be labelled. Immuno-PET can overcome the limitations

of both the direct labelling of the parasite and [^{18}F]FDG PET, through the use of monoclonal antibodies (mAbs) that are specific to malaria parasite proteins and/or antigens to provide an image that is specific to the malaria parasite only.

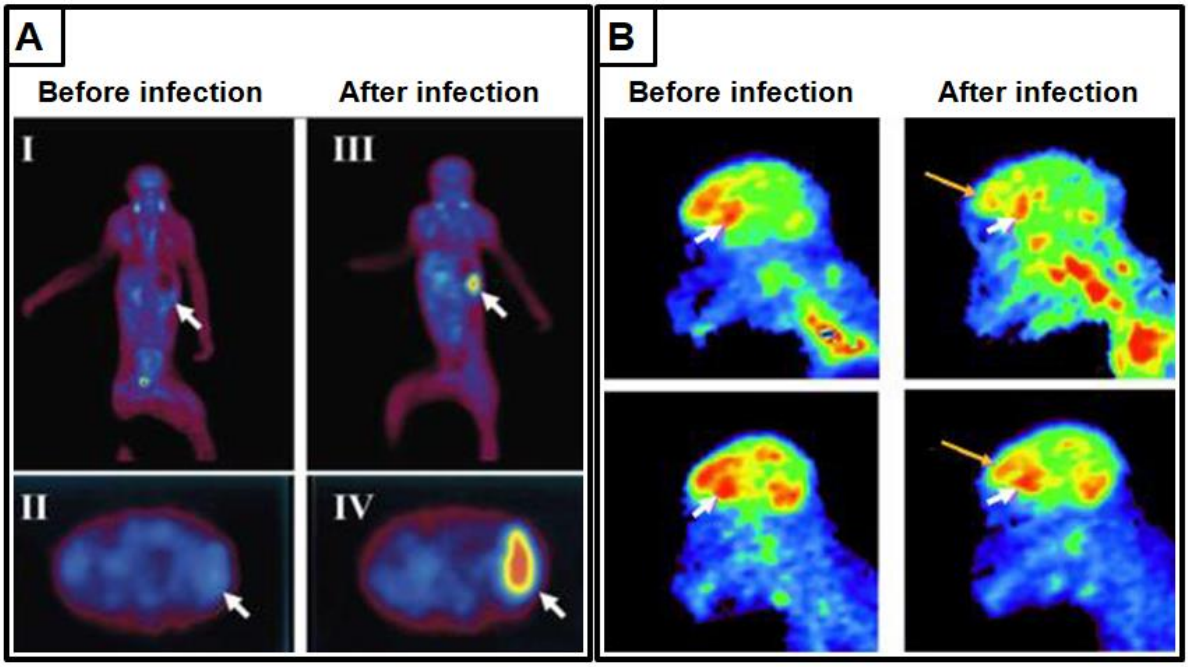

Figure 1.5. [^{18}F]FDG-PET scans of monkeys to study *P. coatneyi* infection *in vivo*. A) Sagittal and transverse [^{18}F]FDG-PET images in a monkey at the level of the spleen before and after *P. coatneyi* infection [147]. I) Sagittal image of monkey before infection. II) Transverse image of monkey before infection. III) Sagittal image of infected monkey with high parasitaemia. IV) Transverse image of infected monkey with high parasitaemia. Arrow indicates position of the spleen. B) Sagittal images of the cerebral metabolic rate of glucose before and after malarial infection in two Japanese macaques [148]. Cross sections of basal ganglia. Yellow arrows indicate frontal lobes. White arrows indicate basal ganglia. Copyright permission granted from American Society of Tropical Medicine and Hygiene [147, 148]

1.5.2 Immuno-PET

Immuno-PET has become a prevalent method for *in vivo* imaging. It combines the high sensitivity and resolution of PET with the superb targeting specificity and affinity of the mAbs to yield functional interpretation of the desired target through non-invasive imaging [151-154]. Immuno-PET can be used in diagnostics and therapeutics – tracers (also known as probes, radiotracers or radiopharmaceuticals) thereby consists of the signalling agent (e.g., radionuclide) coupled to the targeting vector (antibody) (Figure 1.6) [155]. Quite often, a bifunctional chelator serves as a chemical moiety to couple the radionuclide to the targeting vector [156]. Additionally, the bifunctional chelator bears a functional group that permits its attachment to the vector. Although there are various chelators available, the choice for a specific study is usually limited and

dependant on the radionuclide used [157]. It is necessary that the chelator properly complexes and stabilises the radionuclide to prevent dissociation of the radionuclide *in vivo.*

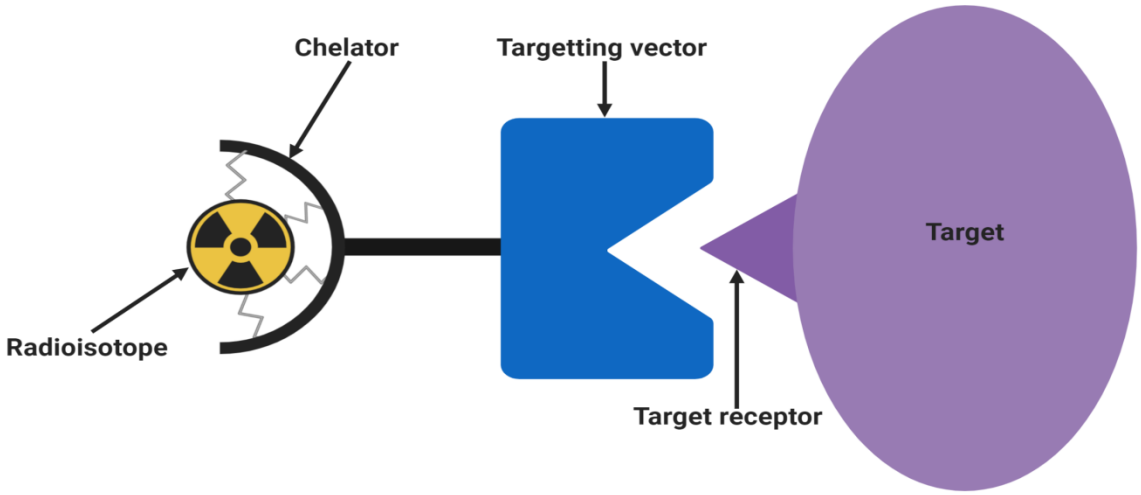

Figure 1.6. Schematic representation of a radiopharmaceutical specific to a target receptor. The radionuclide is linked to the targeting vector via a bifunctional chelator. The vector is responsible for the selective interaction with the target, allowing the radionuclide to concentrate at that site. Input for this figure was obtained from previous publications [158]. Created with BioRender.com.

A number of mAbs have successfully been used for therapeutic applications in cancer and non-cancerous diseases [154]. The mechanisms by which mAbs assist in therapeutics include antibody-dependent cell-mediated cytotoxicity, antibody-dependent cellular phagocytosis, complement dependent cytotoxicity, interruption of a signaling pathway, and inhibition of enzymatic activity of an immune checkpoint [154]. Immuno-PET (i.e., antibody-based PET) tracers have shown to provide good image quality, spatial resolution and quantification. Immunoglobulin type G (IgG) is the most used antibody in therapeutic and imaging modalities. However, the use of mAbs does have several disadvantages. Firstly, their large size that results in slow clearance via the liver limits antibodies to be used for imaging liver diseases. The slow blood clearance often results in poorer image quality due to an elevated background signal [152, 159]. Secondly, mAbs contain a fragment crystallisable (Fc) region that binds to Fc receptors to activate the complement system [160]. The Fc domain also interacts with the neonatal Fc receptor which protects the mAb from degradation and thereby extends the serum half-life of the mAb [161]. Although this extension in half-life of mAbs are preferred for certain therapies, in a number of imaging applications, these Fc-mediated outcomes and long biological half-lives are undesirable [154, 162]. The

persistent mAbs blood pool circulation can also cause unwanted radiation exposure and adsorption to healthy organs. Lastly, production of antibodies in large amounts is expensive and needs to be justified for clinical application.

Removing the Fc region from full size IgG antibodies enzymatically yields antigen-binding fragments (Fab, Fab', and F(ab')$_2$) with lower molecular weights. Antibody engineering also allowed rapid and easy development of other small molecules. This technology affected immuno-PET imaging by evolving from using full sized mAbs as tracers to using recombinant antibody fragments (Fab, single-chain variable fragment (scFv)) and their variants (dia-, tria- and tetrabodies, minibodies and single-domain antibodies) (Figure 1.7)

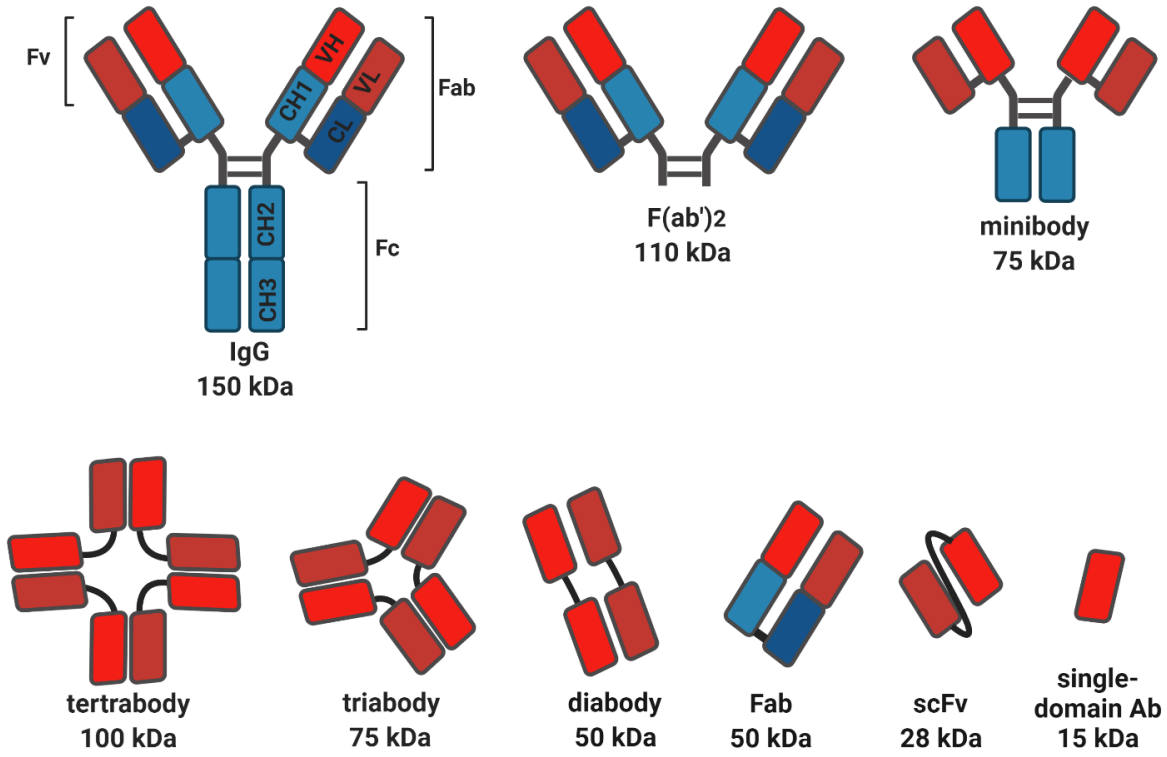

Figure 1.7. Schematic representation of different antibody formats. The classic immunoglobulin type G (IgG) molecule represents a whole antibody with two distinct functional units: fragment antigen binding domains (Fab) and the fragment crystallisable region (Fc). Fc binds to Fc receptors and is responsible to activate the complement system. The Fab consists of a variable fragment (Fv) and a pair of constant domain of heavy chain (CH) and constant domain of light chain (CL) domains. The Fv consists of the variable domain of the light chain (VL) and the variable domain of the heavy chain (VH). Single-chain variable fragment (scFv) consists of a VH and VL domain linked by a peptide linker. A single domain antibody (Ab) consists of only the antigen binding domain of the heavy chain. Created with BioRender.com.

As these smaller fragments are suggested to be rapidly cleared by the renal system, using them as tracer for PET imaging may provide better image quality and delineation of, for instance, tumour from background signal or from unspecific organ-related tissue [163]. Noteworthy, during the development phase, modified radiolabelled antibody fragments may be tested ensuring that their basic targeting and binding properties are maintained [152]. Furthermore, these fragments cannot be biochemically prepared from all subclasses of antibodies, and the production could be tedious and require large quantities of starting materials. Despite these disadvantages, several antibody fragments (mostly Fabs and scFvs) have already entered clinical trial investigations [164].

Immuno-PET radionuclides

There are a wide range of radionuclides available to label antibodies or antibody fragments. The type of radionuclide chosen depends on matching its physical properties (radiological dose, exposure, tissue uptake, half-life, decay characteristics and labelling chemistry) with the targeting ligand and biological process under study [152, 165]. The most commonly used radionuclides in PET imaging include zirconium-89 (^{89}Zr), copper-64 (^{64}Cu), iodine-124 (^{124}I), carbon-11 (^{11}C), oxygen-15 (^{15}O), nitrogen-13 (^{13}N), fluorine-18 (^{18}F), and gallium-68 (^{68}Ga) [152]. Certain short-lived radionuclides (e.g., ^{11}C, ^{15}O, ^{13}N, ^{18}F) were used for diagnostic purposes to determine the location, biochemical and physiological processes of a disease via PET such as Alzheimer's disease, cerebral vascular disease, ARDS, asthma etc [166-170]. PET radiometals with longer half-lives (e.g., ^{64}Cu = 12.7 h; ^{89}Zr = 78.4 h) are mostly used for imaging of prolonged biological processes. For example, ^{89}Zr-labelled tracers have permitted cell trafficking studies, cell signalling measurement, PET/CT-guided biopsies, and prolonged imaging of tumours that exhibit delayed tracer uptake, without the need to reinject the radiotracer [171-174]. These radiometals have mostly been used for labelling intact antibodies and larger antibody fragments such as diabodies, minibodies, Fab and Fab'$_2$ [152].

1.6 Problem statement

Although mAbs have been the most used probe in the past, in the theranostics (combination of therapy and diagnosis), a standard "one-size-fits-all" tracer cannot be applied. Especially in diseases where different stages occur. The choice, design and

development of an appropriate tracer is the key to success of any type of *in vivo* imaging study [156, 175]. The availability of *P. falciparum*-specific tracers for PET-imaging is a big challenge due to the complexity of the disease. This thesis focuses on the discovery and development of probes for future PET imaging of malaria infections.

1.7 Hypothesis

Malaria-specific radiopharmaceutical probes can be developed to display favourable pharmacokinetic and biodistribution properties *in vivo*.

1.8 Aim

This study aimed to develop malaria-specific radiopharmaceuticals for stable and specific detection of malaria parasites with *in vivo* non-invasive PET imaging.

1.9 Objectives

1. Identify the potential of a radiolabelled *Plasmodium*-specific antibody and antibody fragment as tracers for future *in vivo* imaging of malaria (Chapter 2)
2. Discover and develop new single-chain variable fragments specific towards *P. falciparum*-infected erythrocytes (Chapter 3)
3. Investigate and characterise a radiolabelled *P. falciparum*-specific peptide to evaluate its potential for future *in vivo* imaging or antimalarial drug development (Chapter 4)

1.10 Research outputs

During the PhD some research findings were already published or presented as following:

Peer-reviewed publications

Duvenhage J, Ebenhan T, Garny S, González IG, Montaña RL, Price R, Birkholtz LM, Zeevaart JR. Molecular imaging of a zirconium-89 labelled antibody targeting *Plasmodium falciparum*–infected human erythrocytes*. Molecular Imaging and Biology* 22:115-123 (2020); doi.org/10.1007/s11307-019-01360-3

Conference proceedings

Duvenhage J, Garney S, Ebenhan T, Bester C, Bunting H, Van Wyk D, Sathekge M, Birkholtz LM, Zeevaart JR. Zirconium-89 radiolabelling and pre-clinical imaging of *Plasmodium*-specific antibody bioconjugate aimed at the clinical tracking of malaria infections. All Africa Congress on Pharmacology and Pharmacy. Oral presentation. Gauteng, South Africa, 2016

Duvenhage J, Garney S, Ebenhan T, Bester C, Bunting H, Van Wyk D, Sathekge M, Birkholtz LM, Zeevaart JR. Zirconium-89 radiolabelling and preclinical imaging of *Plasmodium*-specific antibody bioconjugate aimed at the clinical tracking of malaria infections. Poster presentation. World Molecular Imaging Congress, New York, United States of America, 2016 [176]

Duvenhage J, Zeevaart JR, Ebenhan T, Birkholtz LM. Zirconium-89 radiolabelling and pre-clinical imaging of *Plasmodium*-specific antibody bioconjugate aimed at the clinical tracking of malaria infections. Malaria Research Conference. Oral presentation. Gauteng, South Africa, 2017

Duvenhage J, Ebenhan T, Birkholtz LM, Garney S, Zeevaart JR. Developing a radiolabelled tracer to image *Plasmodium falciparum* infections *in vivo.* Oral presentation. European Molecular Imaging Meeting. https://eventclass.org/contxt_emim2020/online-program, 2020

Chapter 2

Characterisation and immuno-PET/CT imaging of zirconium-89 labelled antibody IIIB6 and fragment specific to *Plasmodium falciparum*-infected erythrocytes

This chapter has been published in part as follows:

Duvenhage J, Ebenhan T, Garny S, González IG, Montaña RL, Price R, Birkholtz LM, Zeevaart JR. Molecular imaging of a zirconium-89 labelled antibody targeting *Plasmodium falciparum*–infected human erythrocytes*. Molecular Imaging and Biology* 22:115-123 (2020); doi.org/10.1007/s11307-019-01360-3

Previous studies conducted in 2015 provided [^{89}Zr]Zr-IIIB6 microPET/CT images acquired and reconstructed from healthy BALB/c mice. During this PhD those images provided the basis for a qualitative and quantitative data analysis as an integral part of the above publication.

2.1 Introduction

Nuclear *in vivo* imaging has been used to successfully study and gain a better understanding a number of infectious diseases [177]. As mentioned previously, the current *in vivo* imaging techniques used for malaria are either not specific enough ([^{18}F]FDG-PET), lack sensitivity (MRI and CT) or are challenged by translatability to human malaria (e.g., using bioluminescent- and fluorescent imaging to study malaria in mice). Immuno-PET uses antibody-based tracers which combines the high specificity of the antibody-tracer with the sensitivity of the PET imaging modality [178]. IgG monoclonal antibodies (mAbs) are the most common vectors used for nuclear imaging (PET and SPECT) and therapeutic applications [166]. For instance, in the treatment of cancer, immuno-PET and SPECT imaging have been used to guide therapy selection, estimate radiation dosimetry, and track the patient's response to treatment. Furthermore, this non-invasive imaging modality has been used in the study of viral, fungal, and bacterial infectious diseases [179-181].

Evidently, the success of an *in vivo* imaging strategy lies in the appropriate choice, design and development of a tracer [156]. The use of a suitable radioisotope-antibody combination can be of exceptional value for studying the onset and progression of the disease and may allow for monitoring the effects of drug treatment. However, the availability of malaria-specific tracers for PET-imaging is limited due to the complexity of the disease. Full-length mAbs and Fabs have previously been reported to be a suitable vector for radiolabelling and nuclear imaging of various diseases. A commercially available *Plasmodium*-specific full-length IgM antibody (IIIB6) has been characterised *in vitro* to bind to late-asexual *P. falciparum*-infected erythrocyte stages that are associated with sequestration and pathogenesis of malaria [182]. Through a previous study this mAb was successfully radiolabelled with ^{89}Zr which permitted safe administration of the tracer in healthy mice and allowed for non-invasive PET/CT image acquisition.

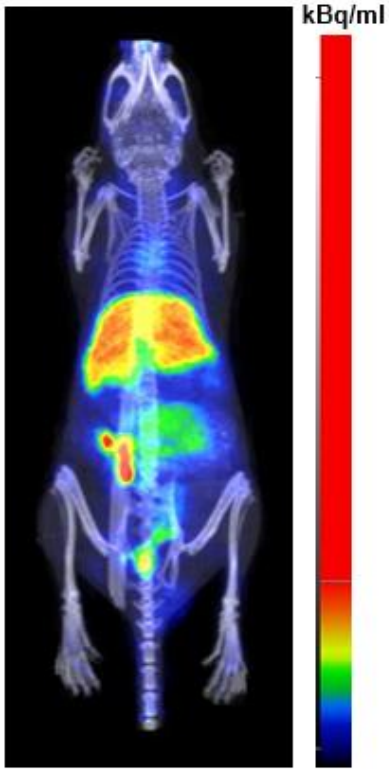

Figure 2.1. A representative microPET/CT imaging of [^{89}Zr]Zr-IIIB6. Maximum intensity projections (MIP) of a representative healthy BALB/c mouse injected with 10.1 MBq. MicroPET/CT image was acquired 2 h post-injection. Color scale: kBq/mL (blue = minimum, red = maximum).

The potential of the ^{89}Zr-labelled IIIB6 ([^{89}Zr]Zr-IIIB6) to be used in future as a malaria imaging agent was also evaluated by comparing its *post-mortem* biodistribution to that of nimotuzumab (h-R3), a mAb approved for human use in cancer therapy and tumour imaging. Although [^{89}Zr]Zr-IIIB6 biodistribution shows comparable results to that of [^{89}Zr]Zr-h-R3, this result pertaining to a *P. falciparum*-specific antibody in the context of malaria has set a novel benchmark.

Herein, we used the microPET/CT images acquired in real-time as a basis for quantitatively determine the tracer's biodistribution and organ activity residence over time. We also assess whether a mAb splice component, i.e., an antibody fragment (Fab), can be radiolabelled and serve as a suitable radiotracer for malaria imaging based on the knowledge that the smaller antibody fragments generally have more favourable pharmacokinetics. The human anti-*P. falciparum* recombinant antibody (clone MGC34) Fab fragment (further denoted as Pf-Fab) used in this study was derived from a human mAb previously isolated from the plasma of *P. falciparum*-infected individuals [183]. This Pf-Fab still recognises erythrocytes infected by various different *P. falciparum* isolates through binding to RIFIN proteins. Pf-Fab is explored in this study to evaluate its potential as an immuno-PET tracer to visualise sequestration of *P. falciparum* parasites in real time.

2.2 Methods

2.2.1 ^{89}Zr-radiolabelling of Pf-Fab

Radiolabelling of the Pf-Fab (clone MGC34) (Creative Biolabs, New York, United States of America) was achieved by firstly conjugating *p*-isothiocyanatobenzyl-desferrioxamine (DFO-Bz-NCS) (CheMatech, Dijon, France) to the side-chains' amino groups of lysine on MGC34 followed by complexation with ^{89}Zr (Figure 2.1) [184].

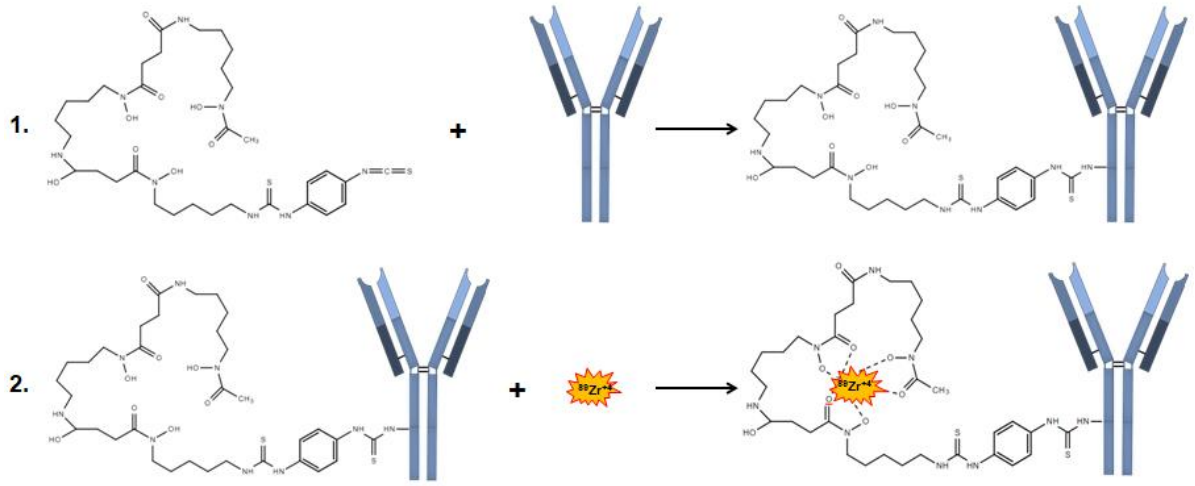

Figure 2.2. Schematic representation of labelling a monoclonal antibody with ^{89}Zr. 1) Firstly, the antibody is conjugated to DFO-Bz-NCS through a thiourea bond between the amino group of the lysine residues of the antibody with the NCS ester functionality of the chelator. 2) Subsequent addition of ^{89}Zr and facile complexation to DFO-mAb.

Concentrating Pf-Fab

The preferred concentration of mAb to perform conjugation is between 2 and 10 mg/ml [185]. Hence, the obtained Pf-Fab (MW ~50 kDa, 1mg/mL in phosphate buffered saline (PBS)) (Creative Biolabs, New York, United States of America) was concentrated using an Amicon Ultra-0.5 Centrifugal Filter Unit (Merck Millipore, Sandton, South Africa) as previously described [182]. In short, the ultrafiltration tube was prepared by rinsing it with 0.5 mL PBS (0.1 M, pH 8.9) by centrifugation (Serie Digicen 21 R, Orto Alresa, Madrid, Spain) for 15 min at 4100 x*g*. Of the Pf-Fab, 500 µL (0.5 mg) was transferred into the ultrafiltration tubes and centrifuged at 4100 x*g*, at 4°C for 20 min. The concentrated Pf-Fab remaining on the column was diluted to 500 µL with PBS (0.1 M, pH 8.9) in the same column and was centrifuged repeatedly at 4100 x*g* and 4°C until the volume of the solution was reduced by more than a fifth (the end volume ~85 µL). The concentrated Pf-Fab was collected by reverse centrifugation at 1000 x*g*

at 4°C for 3 min. This step was followed by adding 50 µL PBS (0.1 M) to the column and reverse centrifugation as above resulting in an end concentration of 3.7 mg/ml Pf-Fab.

Conjugation and purification of the Pf-Fab-chelate

Conjugation was carried out as described previously with some minor alterations [182]. DFO-Bz-NCS (3.38 mg) (CheMatech, Dijon, France) was dissolved in 200 µL 100% DMSO at a concentration of 16.85 mg/mL (pH adjusted to 8.9 with 2 M NaOH and/or 1 M HCl). The amount of DFO-Bz-NCS required to provide a molar excess of 10 to Pf-Fab (Pf-Fab:NCS-Bz-DFO molar ratio of 1:10) was used. The ratio decision was based on literature and specific findings in the laboratory [185]. A volume of 4.5 µL DFO-Bz-NCS was added to the concentrated 135 µL Pf-Fab and incubated at 37°C for 30 min with gentle shaking. The Pf-Fab-chelate (from now on referred to as Pf-Fab-DFO) was purified and concentrated to 3.7 mg/mL (end volume of 109 µl) as described above while changing the buffer from 0.1 M PBS to 0.1 M ammonium acetate (pH adjusted to 7 with 2 M NaOH).

^{89}Zr-radiolabelling of Pf-Fab-DFO

^{89}Zr-radiolabelling was achieved by adopting a previously published method [184]. Briefly, 260 µl ammonium acetate (0.1 M) was added to 145 µl ^{89}Zr-solution (166 MBq in 1 M oxalic acid) (PerkinElmer, Waltham, Massachusetts, USA) and the pH was adjusted to 7.0 (with NaOH and/or HCl). The Pf-Fab-DFO (109 µl) was added to the ^{89}Zr-solution and incubated for 1 h at 25°C while shaking gently (pH maintained at 7). Radioactive instant thin-layer chromatography (radio-iTLC) on silica-gel-plated (SG-iTLC) strips was performed to determine the labelling efficiency (%LE) of ^{89}Zr-DFO-Bz-NCS-Pf-Fab (referred to as [^{89}Zr]Zr-Pf-Fab) and to monitor the stability of the radiolabelled product as radiochemical purity (%RCP) over time. Before performing radio-iTLC, to scavenge any free radiometal, the sample was supplemented with EDTA (0.01 M, pH 6.0) corresponding to a tenth of the sample volume. Radio-iTLC was then carried out by using 10% (w/v) ammonium acetate:methanol (1:1) as the mobile phase; measurement was either carried out by one of the following methods: a) cutting the strips into segments and measuring each segment's activity, or b) scanning the entire paper on a MiniGITA TLC scanning device (Elysia-raytest, Straubenhardt, Germany). When radio-iTLC analysis was carried out by a) cutting the strips into segments, the activity of each segment was measured, and the sum of these

counts was used to determine the %RCP or %LE as a fraction of the total radioactivity (%RCP or %LE = counts per second (CPS) in specific segment/total CPS of all the segments) x 100)). If radio-iTLC was carried out by b) using the TLC scanning, analyses were done with Gina X Analysis software (Raytest GmbH, Straubenhardt, Germany) to determine the %RCP = counts (product radio-peak)/total counts (all detectable radio-peaks)) x 100.

After radiolabelling, the [^{89}Zr]Zr-Pf-Fab was purified from remaining free ^{89}Zr using the ultrafiltration tubes (same method as described in previous section) and the %RCP was assessed by radioactive high performance liquid chromatography (radio-HPLC) using a Varian Prostar 325 UV-Vis apparatus (Varian Inc., Walnut Creek, CA, USA) aligned with a GABI Star gamma detector (Raytest GmbH, Straubenhardt, Germany). Following sample injection, size exclusion chromatography (SEC) (BioSep™ 5 µm SEC-s2000, 300 × 7.8 mm, Phenomenex, Aschaffenburg, Germany) was performed using an isocratic flow (1 mL/min) of 0.1 M phosphate buffer (pH 8.5) for 25-35 min.

2.2.2 Animal studies

Animal preparation

Ethical clearance for the study was obtained through the North-West University's Animal Research Ethics Committee (AnimCare REC: NWU-00175-18-S5) to comply with the South African National Health Act 61 (2003), the South African National Standards (SANS) document 10386:2008 and the Ethics in Health Research: Principles, Structures and Processes. Healthy BALB/c mice (7 weeks old, 20-26 g, female) were used for the *in vivo* characterization of [^{89}Zr]Zr-Pf-Fab. The animals (n=5) were housed in a high barrier specific pathogen-free (SPF) facility (North-West University (NWU) vivarium, Potchefstroom, South Africa) and fed standard rodent maintenance chow (Nutroscience, Malmesbury, South Africa). Animals were transferred to the Interim Preclinical Imaging Facility (IPCIF) located at the South African Nuclear Energy Corporation (Necsa) and were acclimatised to the new environment for 6 days with daily monitoring by a qualified veterinary animal technician. Mice were housed with 12 h/12 h day/night cycle, at 22°C with a 55% relative humidity in enriched individual ventilated cages (IVC GM500, Tecniplast, Buguggiate, Italy) on chipped corn-cob bedding; water was available *ad libitum.*

MicroPET/CT imaging

Prior to tracer administration, animals were anaesthetised using 2-3% Isoflurane (Isofor(r) Sanofi-Aventis, Midrand, South Africa) in oxygen. The formulation (volume of 150 µL) consisted of saline containing [^{89}Zr]Zr-Pf-Fab (3-5 MBq) which was injected intravenously via the tail vein. Nuclear imaging was performed utilizing a dedicated microPET/CT camera (Mediso Medical Systems, Debrecen, Hungary). MicroPET/CT was performed at 1 h, 3 h, 6 h, and 24 h after tracer injection (30 min image acquisition). Image-guided biodistribution of [^{89}Zr]Zr-Pf-Fab was determined at each time point.

PET image reconstruction was performed from list-mode: reconstruction algorithm: 3DOSEM (6 iterations; Terra-Toma 3D), energy window 400-600 keV, coincidence mode 1:5, corrections for random events, detector normalization, decay, dead time and voxel size: 0.65 mm^3. Inter View Fusion software version 2.02.055.2010 (Mediso Medical Systems, Debrecen, Hungary) was used for image visualization, yielding co-registered PET/CT images in axial, coronal, and sagittal orientation. Analysis of the MicroPET/CT images included the drawing of three-dimensional volumes of interest (VOI) to determine the standard uptake values (SUV) of [^{89}Zr]Zr-Pf-Fab in selected organs. Semiquantitative analysis was used to determine a normalised SUV, defined as the regional tissue radioactivity concentration normalised to account for injected dose and body weight of the animal, thus the SUV values (tissue/organ tracer concentrations (g/mL)) were further used to generate time-activity curves.

***Ex vivo* tracer biodistribution of [^{89}Zr]Zr-Pf-Fab**

To further validate the *in vivo* distribution of [^{89}Zr]Zr-Pf-Fab, systematic endpoint biodistribution studies were performed. Following the final PET image acquisition (i.e., 24 h post injection of [^{89}Zr]Zr-Pf-Fab), animals were euthanized while still under anaesthesia, organs were dissected, weighed and the activity in organ- or tissue-related activity was determined using an automated gamma counter (Hidex AMG, Turku, Finland). Following activity corrections for background and radioactive decay, the results were expressed in relation to the injected dose (ID) and adjusted for organ weight (%ID/g). Control animals received a formulation of saline containing either [^{89}Zr]Zr-IIIB6 (7.5-15.1 MBq) or [^{89}Zr]Zr-oxalate (8.3-11.7 MBq). These animals were euthanised 24 h post injection and their biodistribution determined as described for [^{89}Zr]Zr-Pf-Fab.

2.3 Results

2.3.1 MicroPET/CT analysis and organ activity residence of [^{89}Zr]Zr-IIIB6

MicroPET/CT imaging acquired previously provided qualitative [^{89}Zr]Zr-IIIB6 distribution data which indicated predominant tracer residing in the liver and the spleen (a representative image diplayed Figure 2.2). PET/CT image-guided analysis allowed for quantification of [^{89}Zr]Zr-IIIB6 concentrations presented in organs/tissues by means of VOI-based SUV calculation and subsequent displayed as time-activity curves (Figure 2.3).

The microPET/CT image-guided quantification allowed the calculation of the *in vivo* tracer concentrations (n=3) in relevant organs/tissues (Figure 2.3). The time-activity curve (TAC) analysis of the blood pool (heart) demonstrated an exponential decrease ($y = 18.22e^{-0.116x}$, $R^2 = 0.978$) expected for intraveinous tracer administration (Figure 2.3).

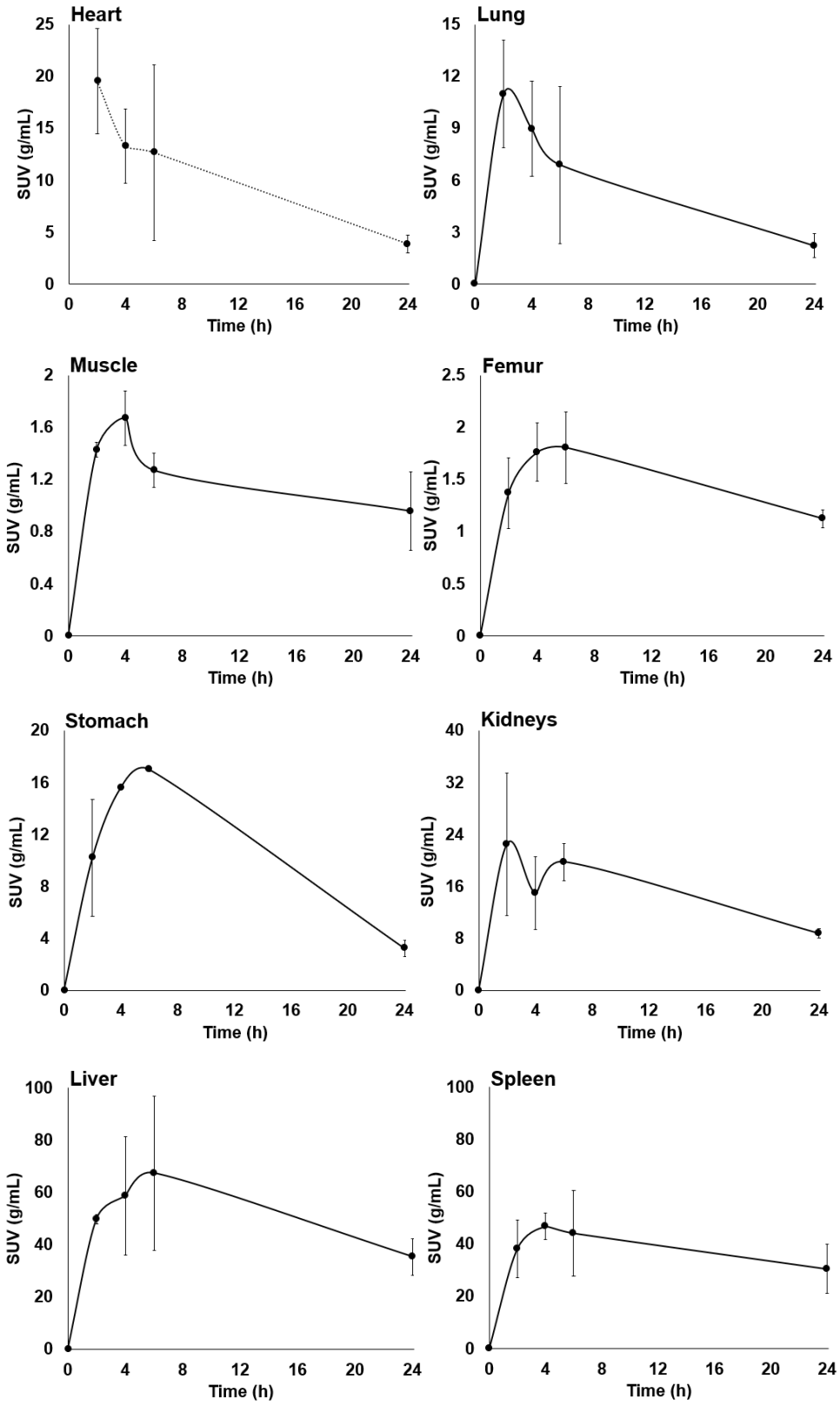

Figure 2.3. Time-activity curves representing the concentration of [^{89}Zr]Zr-IIIB6 in various organs. Healthy BALB/c mice were injected with [^{89}Zr]Zr-IIIB6 and microPET/CT was performed at different time points. The reconstructed images were subjected to VOI analyses delineating heart, lung, muscle tissue, bone (femur), stomach, kidneys, liver, and spleen VOI which provided SUV values (g/mL). Results are displayed as mean ± SEM (n=3).

The liver had the highest tracer concentration with a maximun calculated [^{89}Zr]Zr-IIIB6 concentration of 67 ± 30 g/mL 6 h post-injection (Figure 2.3). There was no significant hepatic wash out over 24 h. The TAC analysis also demonstrated high tracer concentration in the spleen where the maximun [^{89}Zr]Zr-IIIB6 concentration of 46 ± 5 g/mL was observed 4 h post-injection. Favourable low activities were observed in the muscle and the bone (SUV<2.5 g/mL) indicating that it would not pose any unwanted background signal that would influence the image quality. Rapid tracer clearance was observed in the lungs and kidneys where maximum tracer concentration was observed only 2 h post-injection, followed by a significant wash out and minimum concentration at 24 h (*P*<0.05).

2.3.2 ^{89}Zr-radiolabelling of Pf-Fab

To determine the specific retention times of pure Pf-Fab (in 0.1 M PBS), DFO-Bz-NCS (in DMSO) and [^{89}Zr]Zr-oxalate, SEC-HPLC was performed (Figure 2.4).

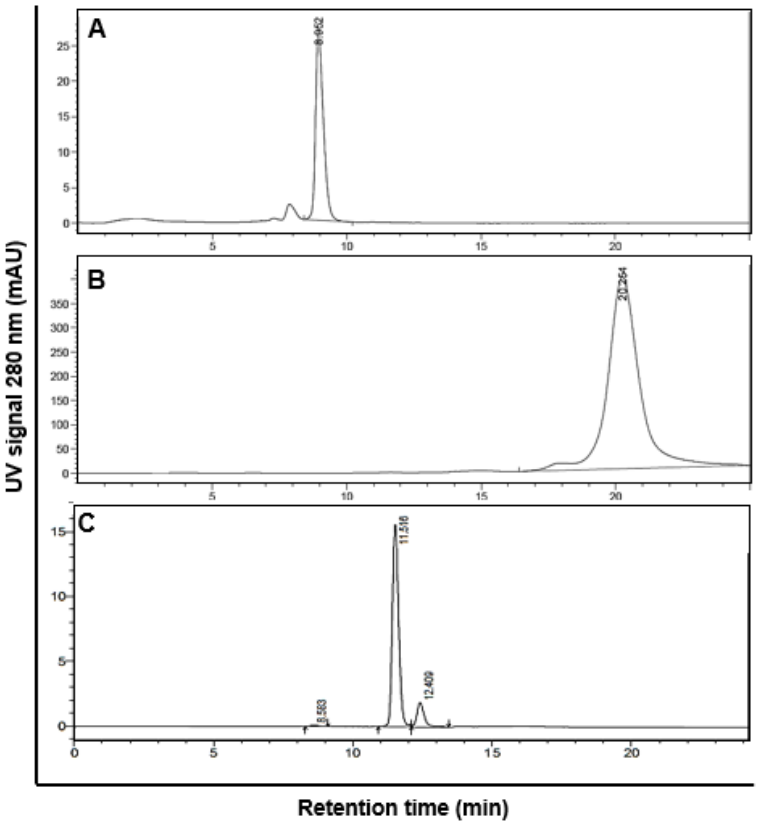

Figure 2.4. Representative HPLC-UV analysis (signal intensity at 280 nm wavelength). The UV signal was detected for retention times of A) Pf-Fab, B) DFO-Bz-NCS and C) [^{89}Zr]Zr-oxalate**.** Isocratic HPLC elution was performed in 0.1 M phosphate buffer (pH 8.5) using BioSep™ 5 µm SEC-s2000, 300 × 7.8 mm (Phenomenex, Aschaffenburg, Germany) column (1.0 mL/min). A volume of 10 µL was injected.

The retention times of the Pf-Fab were 8.9 min with an additional small peak present at 7.9 min (Figure 2.4) while the chelator had a retention time of 20.26 min with a small peak at around 17.85 min. HPLC-UV revealed the retention time for [^{89}Zr]Zr-oxalate at 11.5 min with a small peak at 12.4 min (Figure 2.4). These retention times were subsequently used to monitor and analyse the radiolabelling process.

Prior to ^{89}Zr-radiolabelling of the Pf-Fab, a prerequisite step involving DFO-Bz-NCS conjugation to Pf-Fab is mandatory. Literature reports and previous laboratory experiments using the IIIB6 and hR3 steered the decision for a Pf-Fab:NCS-Bz-DFO molar ratio of 1:10 [185]. Due to the low Pf-Fab volume and concentration used during conjugation, monitoring of the conjugation reaction using SEC-HPLC was not feasible, however, radio-iTLC was capable of monitoring the conjugation (only after the step of ^{89}Zr-labelling of Pf-Fab; i.e., successful radiolabelling equals successful conjugation) and the %LE (Figure 2.5). Using a polar mobile phase such as 10% (w/v) ammonium acetate:methanol (1:1), free [^{89}Zr]Zr-oxalate is known to migrate with the solvent (segment 5, R*f* = 0.8-1.0) front while [^{89}Zr]Zr-Pf-Fab remain close to the origin (segment 1, R*f* = 0.0-0.2).

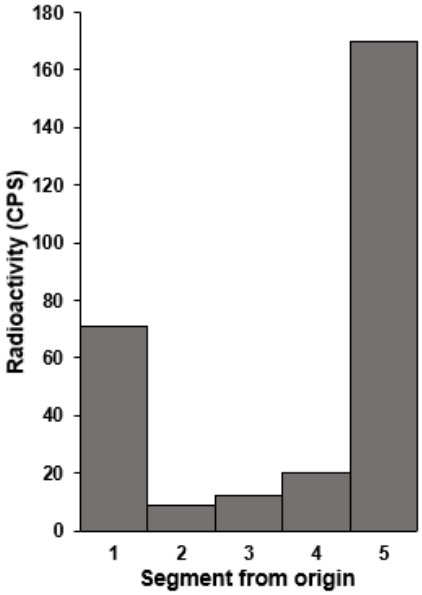

Figure 2.5. Radio-iTLC analysis of crude [^{89}Zr]Zr-Pf-Fab. Directly after ^{89}Zr-labelling of Pf-Fab and before purification of the product ([^{89}Zr]Zr-Pf-Fab), 1 µL sample was spotted on the bottom of the SG-iTLC strip (origin) and allowed to run in a mobile phase (10% (w/v) ammonium acetate:methanol (1:1)) until reaching the last part of the strip (solvent front). The plate was cut in 5 equal-sized segments (each segment = 2 cm) and the radioactivity of each segment was measured.

When comparing the radioactivity measured in segment 5 relative to all segments about 60% [^{89}Z]Zr-oxalate was not bound to the Pf-Fab (Figure 2.5). In contrast, the radioactivity associated with the radiolabelled Pf-Fab (segment 1) was about 25%. Three consecutive ultrafiltration (purification) steps were required to significantly minimize free [^{89}Zr]Zr-oxalate (P<0.001). The RCP was determined using radio-iTLC (Figure 2.6.A) and radio-HPLC (Figure 2.6.B) (as described above) and both methods indicated that a desirable 99% RCP was achieved.

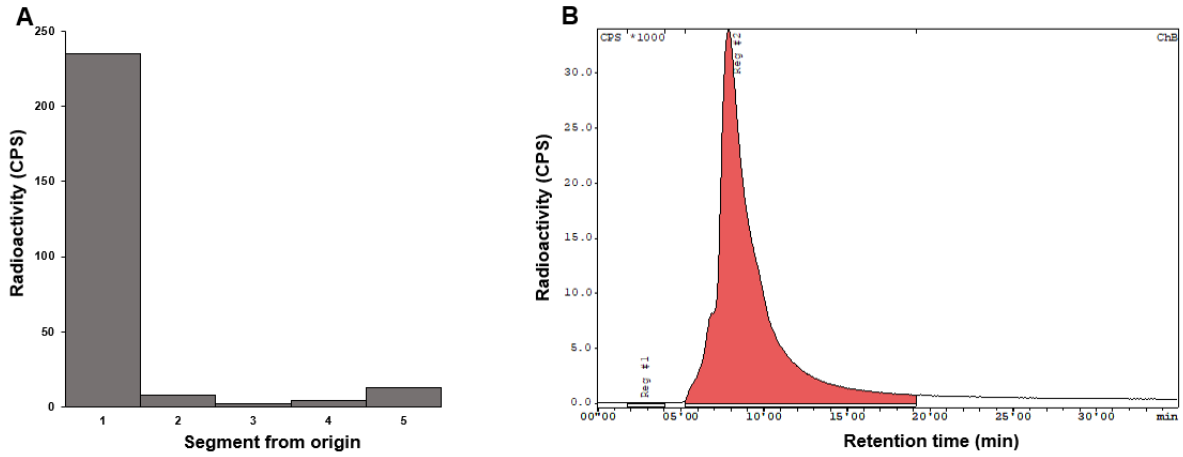

Figure 2.6. A) Radio-iTLC analysis and B) radio-HPLC of [^{89}Zr]Zr-Pf-Fab. [^{89}Zr]Zr-Pf-Fab was purified and analysed by radio-iTLC and radio-HPLC. A) The SG-iTLC strip was spotted with 1 µL sample (origin) and allowed to run in a mobile phase (10% (w/v) ammonium acetate:methanol (1:1)) until reaching the top end of the strip (solvent front). The plate was cut in five equal-sized segments and the radioactivity (CPS) of each segment counted. B) Radio-HPLC was carried out using a Varian Prostar 325 UV-Vis apparatus (Varian Inc., Walnut Creek, California, USA) aligned with a gamma detector (GABI Star, Raytest GmbH, Straubenhardt, Germany). Following sample injection (20 µL) SEC (BioSep™ 5 µm SEC-s2000, 300 × 7.8 mm, Phenomenex, Aschaffenburg, Germany) was performed using an isocratic flow (1 mL/min) of 0.1 M phosphate buffer (pH 8.5) for 35 min.

The radio-HPLC showed that 99% of the activity resided in a single radioactive peak that was congruent with the retention time of Pf-Fab (8.9 min) (Figure 2.6.B). There was no recognizable radioactivity peak present at 20 min that would have been indicative of the presence of ^{89}Zr-DFO-Bz-NCS. The purification yielded [^{89}Zr]Zr-oxalate-free solution of [^{89}Zr]Zr-Pf-Fab with a radiochemical yield (RCY) of 47 MBq (28%) and activity concentration of 100 MBq/mL.

To determine the complexation integrity of ^{89}Zr in relation to the [^{89}Zr]Zr-Pf-Fab product over time (bench-top incubation), a sensitive radio-iTLC scanner was utilised as described above. By direct gamma detection on the TLC bed, the SG-iTLC strip could be scanned multiple times over several minutes to detect any reoccuring ^{89}Zr-activity

that lost its integrity with the product (Figure 2.7). The integrity of [^{89}Zr]Zr-Pf-Fab remained stable over time (95% of the total counts resided in the radio-peak associated with [^{89}Zr]Zr-Pf-Fab).

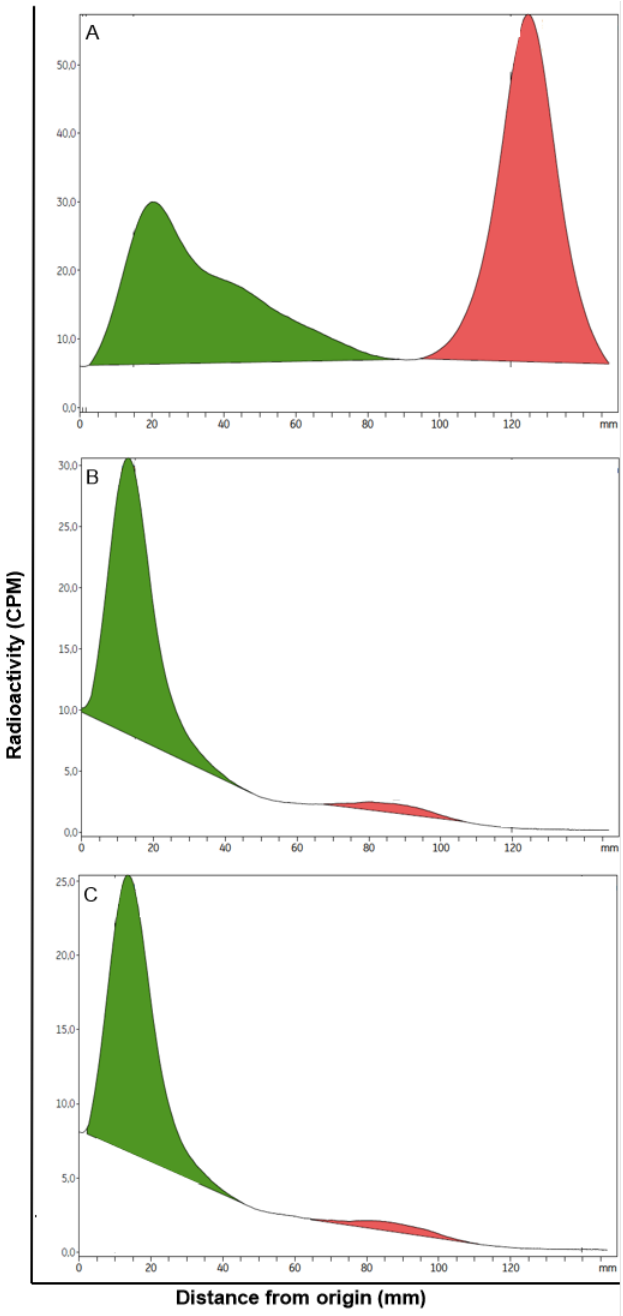

Figure 2.7. Radio-iTLC analysis and complexation integrity in relation to the [^{89}Zr]Zr-Pf-Fab product with prolonging bench-top incubation. Each SG-ITLC strip was spotted with 1 µl product sample (origin) and allowed to run in a mobile phase (10% (w/v) ammonium acetate:methanol (1:1)) until reaching the last part of the strip (solvent front). Radio-TLC analysis was performed using a dedicated TLC scanner connected to a gamma counting probe (Elysia MiniGITA, Raytest, Straubenhardt, Germany). A) peak identification was performed using dedicated analysis software (Gina X, Raytest, Straubenhardt, Germany) according to the retention of both [^{89}Zr]Zr-oxalate (peak at the solvent front indicated in pink) and [^{89}Zr]Zr-Pf-Fab (peak at the origin indicated in green). Similar to A) the radioactivity distribution in the purified [^{89}Zr]Zr-Pf-Fab solution was studied following a B) 24 h and C) 48 h bench-top incubation.

2.3.3 Animal studies

Preclinical microPET/CT analysis and *ex vivo* biodistribution studies were performed for [^{89}Zr]Zr-IIIB6 [182]. The *ex vivo* data of [^{89}Zr]Zr-IIIB6 were used to compare to those of [^{89}Zr]Zr-Pf-Fab.

Preclinical microPET/CT studies of [^{89}Zr]Zr-Pf-Fab

After successful radiolabelling, [^{89}Zr]Zr-Pf-Fab was evaluated for its *in vivo* stability and biodistribution. Upon intravenous tail injection of 4.5 ± 0.5 MBq, the mice did not exhibit any adverse events or abnormal behaviour. MicroPET/CT scans 1 h, 3 h, 6 h, and 24 h post-injection (Figure 2.8) resulted in images of excellent quality, even with mice injected with activity as little as 3.23 MBq.

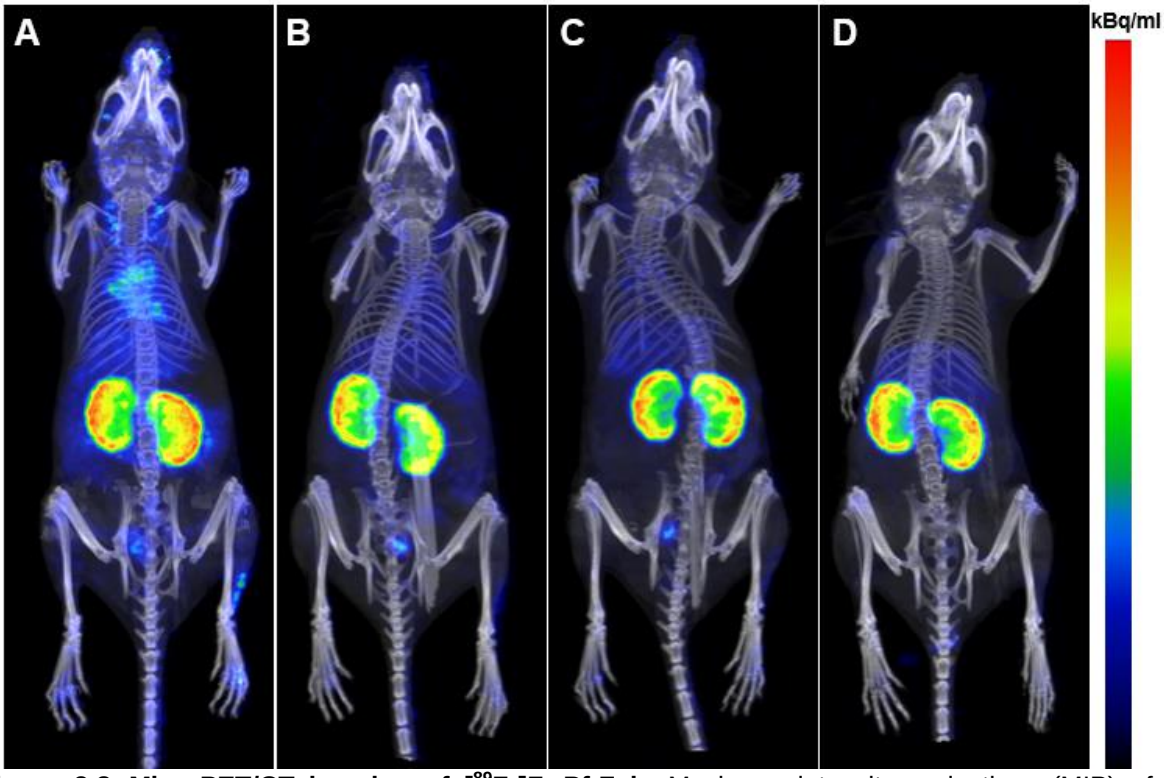

Figure 2.8. MicroPET/CT imaging of [^{89}Zr]Zr-Pf-Fab. Maximum intensity projections (MIP) of a representative healthy BALB/c mouse injected with 4.9 MBq. MicroPET/CT images were acquired for 30 min at A) 1 h, B) 3 h, C) 6 h and D) 24 h post-injection. Color scale: kBq/mL (blue = minimum, red = maximum).

Qualitative microPET/CT analysis using real-time maximum intensity projection (MIP) images of each 20 min image acquisition indicated visible activity in the kidneys was visible as early as 1 h post-injection (Figure 2.8). The activity in this organ appeared to remain constant over 24 h. The activity appeared to be mostly concentrated in the

renal cortex, however, this can only be concluded with *post-mortem* studies by way of microtomic organ slicing and autoradiographic organ analysis. Moderate liver uptake was seen from 3 h post-injection. At 1 h the presence of the tracer in the cardiovascular system could be identified which then gradually decreased over time until no notable activity was observed at 24 h. Some inconsistent bladder activity was seen (in some of the mice).

Quantification of the *in vivo* biodistribution was performed on the microPET/CT images by way of image guided calculation of the tracer concentrations in organs/tissues by means of standard SUVs and VOI-based time-activity curves (Figure 2.9 and Figure 2.10).

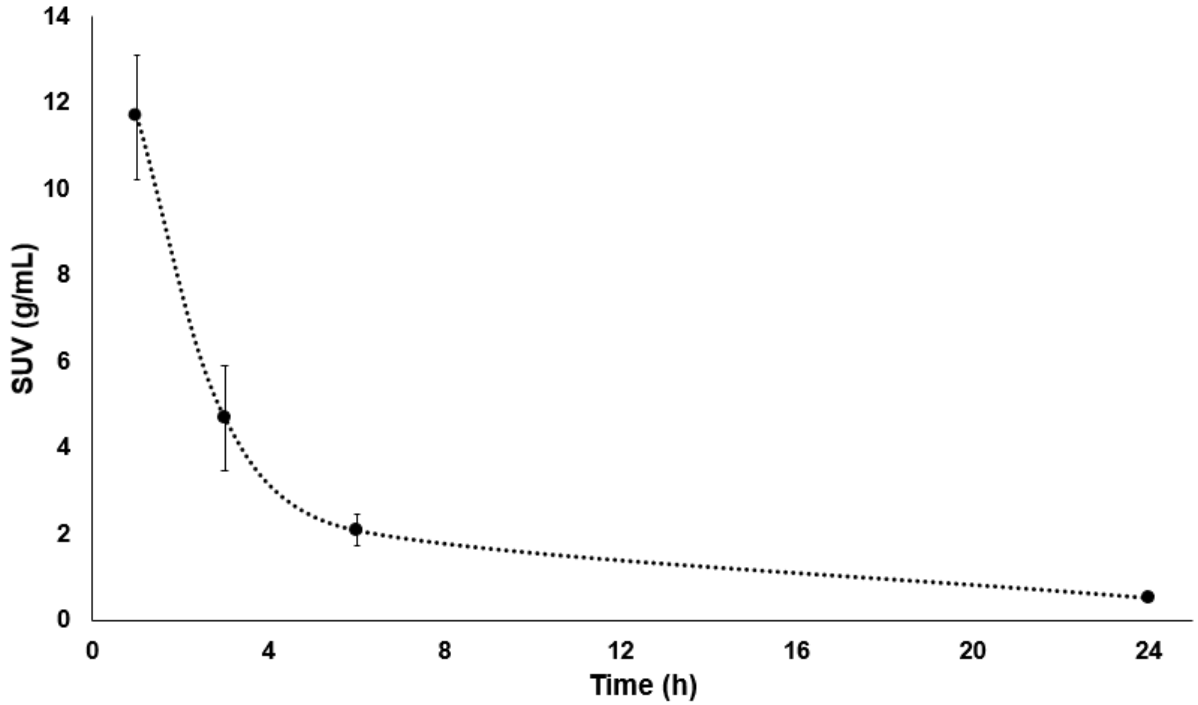

Figure 2.9. Time-activity curve representing the blood pool concentration of [^{89}Zr]Zr-Pf-Fab. Healthy BALB/c mice were injected with [^{89}Zr]Zr-Pf-Fab and microPET/CT was performed at different time points. The reconstructed images were subjected to VOI analyses of the myocardium which provided SUV values (g/mL). Results are displayed as mean ± SEM (n=3).

Based on the TAC (Figure 2.9), the tracer concentration present in the myocardium may decrease exponentially ($y = 7.4827e^{-0.116x}$, $R^2 = 0.7477$) after intravenous injection. The pharmacological half-life was 3.5-6.0 h with an excretion rate of about 0.116 g/h.

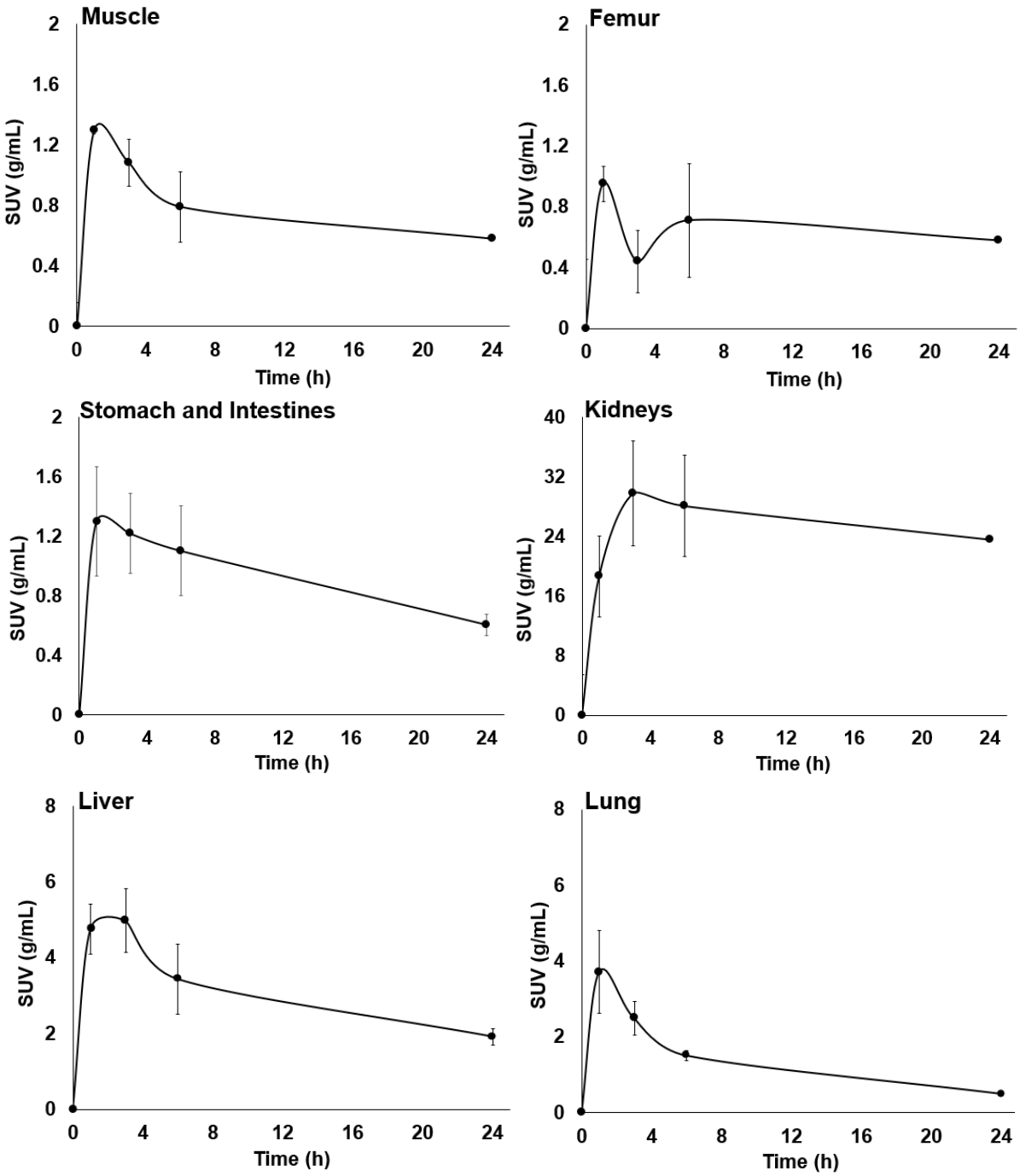

Figure 2.10. Time-activity curves representing the concentration of [^{89}Zr]Zr-Pf-Fab in various organs. Healthy BALB/c mice were injected with [^{89}Zr]Zr-Pf-Fab and microPET/CT was performed at different time points. The reconstructed images were subjected to VOI analyses delineating muscle tissue, bone (femur), liver, lung, kidneys and an abdominal VOI (including stomach and intestines) which provided SUV values (g/mL). Results are displayed as mean ± SEM (n=3). Time activity curves are scaled according to the following: low level uptake: SUV<2; moderate level uptake: SUV<8, high level uptake: SUV<40.

The microPET/CT image-derived quantification allowed the calculation of the *in vivo* tracer concentrations (n=3) in relevant organs or tissues (Figure 2.10). Both the liver and kidneys showed a delayed peak concentration (compared to the rest of the organs

or tissues) where the highest SUV was observed only at 3 h. There was a significant decrease in radioactivity in the liver from 3 h to 24 h (P<0.05). The kidneys had the highest tracer concentration with a calculated [^{89}Zr]Zr-Pf-Fab concentration of 18.6 ± 5.4 g/mL at 1 h and a maximum of 29.7 ± 5.4 g/mL reached at 3 h post-injection. There was no significant wash out of the tracer in the kidneys over 24 h. The low activity in the muscle and bone (SUV<1.3 g/mL) was similar to the background signal. The TAC of the femur, intestines and lung showed similar [^{89}Zr]Zr-Pf-Fab behaviour with the maximum tracer concentration present at 1 h post-injection and this concentration decreased over time. In the lung, the maximum concentration of 3.7 ± 4.4 g/mL was observed at 1 h followed by a significant decrease at 24 h to a minimum SUV of 0.5 ± 0.4 g/mL (P=0.055). The concentration in the femur decreased over time with a significant wash out from 1 h to 24 h (P<0.05) and a residual tracer concentration at 24 h of 0.58 ± 0.23 g/mL. The stomach and intestines did not show any significant decrease in activity even after 24 h (P=0.11), although very low SUV of 1.0 was determined by VOI analysis. The spleen was undetectable with the CT and the splenic uptake of [^{89}Zr]Zr-Fab was not sufficient to delineate the organ to calculate the SUVs. The splenic uptake could therefore only be evaluated *ex vivo*.

Ex vivo biodistribution of [^{89}Zr]Zr-Pf-Fab

In addition, to validate the results from [^{89}Zr]Zr-Pf-Fab-microPET/CT image analysis, endpoint biodistribution studies were performed *ex vivo* by way of dissecting various tissues/organs of the previously injected healthy BALB/c mice. Tracer biodistribution in various organs is displayed for [^{89}Zr]Zr-Pf-Fab (Figure 2.11) considering dissection at 24 h post-injection. The organ uptake (%ID/g) for [^{89}Zr]Zr-Pf-Fab is displayed in comparison to biodistribution studies in mice injected with [^{89}Zr]Zr-IIIB6 and [^{89}Zr]Zr-oxalate [182] (please see Appendix Table A.2 for biodistribution data and P-values).

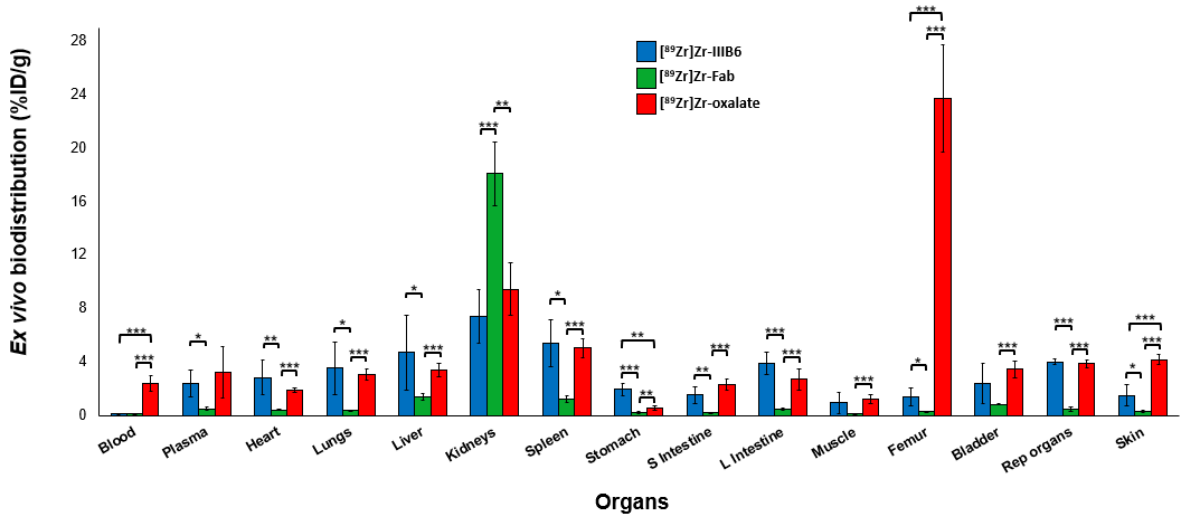

Figure 2.11. *Ex vivo* biodistribution of ^{89}Zr-labelled compounds. Healthy BALB/c mice were administered intravenously with either [^{89}Zr]Zr-IIIB6 (n=5), [^{89}Zr]Zr-Pf-Fab (n=5) or [^{89}Zr]Zr-oxalate (n=4) and dissection and gamma counting of organs/tissues were performed 24 h post-injection. Results are expressed as the mean as a percentage of injected dose per gram of each organ/tissue (%ID/g) ± SD. Student's *t*-test was performed to determine the statistical significance of the tracer concentration between the three compounds (*P<0.05; **P<0.01; ***P<0.001).

A rather straight forward *ex vivo* biodistribution of a novel ^{89}Zr-labelled compound can be compared to that of [^{89}Zr]Zr-oxalate to determine its potential as an imaging agent. Meeting the expectation, [^{89}Zr]Zr-oxalate, acting similar to the uncomplexed ^{89}Zr-metal, predominantly targets the bone tissue wherein [^{89}Zr]Zr-oxalate (23.8 %ID/g) was 79-fold higher compared to the bone uptake calculated from mice injected only with [^{89}Zr]Zr-Pf-Fab (0.3 %ID/g; P<0.001) (Figure 2.11) [186]. Hence, low bone uptake indicated the *in vivo* stability of the [^{89}Zr]Zr-Pf-Fab complex, i.e., ^{89}Zr-ions did not seem to dissociate from the Pf-Fab-DFO conjugate.

The potential of [^{89}Zr]Zr-Pf-Fab uptake was also compared with the uptake of [^{89}Zr]Zr-IIIB6, the only malaria-specific antibody that has been evaluated [182]. There were no significant differences between [^{89}Zr]Zr-Pf-Fab and [^{89}Zr]Zr-IIIB6 uptake found in the bladder, muscle and blood pool of the mice. Most of the other analysed organs and tissues had a significantly higher uptake of [^{89}Zr]Zr-IIIB6 over [^{89}Zr]Zr-Pf-Fab. Significantly more [^{89}Zr]Zr-IIIB6 (2.42 %ID/g) resided in the plasma than [^{89}Zr]Zr-Pf-Fab (0.5 %ID/g; P=0.012) indicating that [^{89}Zr]Zr-Pf-Fab has much faster clearance rate over 24 h. The radioactivity of [^{89}Zr]Zr-Pf-Fab (1.2 %ID/g) in the spleen was 4.5-fold less than that of [^{89}Zr]Zr-IIIB6 (5.4 %ID/g; P=0.012) and about 4.0-fold less than [^{89}Zr]Zr-oxalate (5.0 %ID/g; P<0.001). Hepatic radioactivity determined for [^{89}Zr]Zr-Pf-

Fab (1.2 %ID/g) was at least 3.0-fold lower than that of [^{89}Zr]Zr-IIIB6 (5.4 %ID/g; *P*=0.013). The kidneys exhibited a significantly higher uptake of [^{89}Zr]Zr-Pf-Fab (18.13 %ID/g) compared to [^{89}Zr]Zr-IIIB6 (7.40 %ID/g; *P*=0.0001). [^{89}Zr]Zr-Pf-Fab presented high kidney and relatively low liver uptake, when compared to [^{89}Zr]Zr-IIIB6 which might indicate a shift of excretion processes between the two compounds (predominant renal excretion of [^{89}Zr]Zr-Pf-Fab and hepatobiliar excretion for [^{89}Zr]Zr-IIIB6).

2.4 Discussion

The key difficulty in malaria research that limits our knowledge of the infection is the inability to visualise and to observe the intricate host-parasite mechanisms that govern malaria pathogenicity *in situ.* Previously used *in vivo* imaging techniques such as MRI, CT or bioluminescence lack the selectivity, specificity, and sensitivity required to study processes of malaria infection in real time. Nuclear imaging techniques such as PET and SPECT have been used successfully to study infectious diseases *in vivo* and have been introduced as important pre-clinical research tools to evaluate organ and tissue functionality, metabolism and pathologies related to diseases. Our group has successfully accomplished the first proof-of-concept radiolabelling of IIIB6 for *in vitro* and *in vivo* molecular imaging [182]. The microPET/CT image-derived quantification of the [^{89}Zr]Zr-IIIB6 distribution revealed that the tracer concentration in the liver and spleen remained high even after 24 h post-injection. The biodistribution [^{89}Zr]Zr-IIIB6 in mice confirmed this non-specific uptake and persistent radioactivity levels in these organs that are usually involved in malaria pathology. As the drawbacks of using mAb as imaging tracers are mostly associated with their size, we explored a different tracer, [^{89}Zr]Zr-Pf-Fab in this study, towards more favourable PET imaging quality and biodistribution. However, IIIB6 could still be used for other optical imaging (BLI or FLI) approaches such as live cell fluorescence microscopy and flow cytometry.

P. falciparum express various antigens on the surface of infected erythrocytes (iRBCs) that may differ with each of its life cycles. Some of these antigens are responsible for the severity of the disease, especially those that are involved in sequestration and cytoadherence of iRBC to host organs and tissues. Tan *et al*. (2016) has successfully isolated human mAbs that recognise erythrocytes infected with various *P. falciparum* isolates via binding to RIFIN peptides [183]. This broad reactivity was obtained by an insertion of a large DNA fragment between the V and DJ that was responsible for the binding to RIFIN family. It encodes the entire collagen-binding domain of the LAIR-1, an Ig superfamily inhibitory receptor encoded on chromosome 19. The antibodies were produced by a single expanded B cell clone that carries a distinct mutation in the LAIR-1 domain that eliminates collagen binding while increasing binding to iRBCs. Subsequently, a fragment antibody of one of these mAbs, clone MGC34 that maintains sufficient ability to bind to isolates of various strains of *P. falciparum*, has been generated by Tan *et al.* (2016) [183]. In this study the MGC34 Fab was characterised

and developed to serve as a prospective immuno-PET tracer. [^{89}Zr]Zr-Pf-Fab can, in future studies, be examined for its potential to visualise the sequestration of late-stage trophozoite- and schizont-infected *P. falciparum* parasites in real time.

There are multiple radionuclides, all with different characteristics, that have been successful applied using immuno-PET imaging, however, the choice of the radionuclide should depend on the aim of the study. In particular, ^{89}Zr has ideal physical characteristics and properties that increased its popularity for immuno-PET imaging applications (e.g., high resolution that allows for facile quantitative imaging, a long half-life of 78.4 h, and decays via positron emission (23%) and electron capture (77%) to ^{89}Y [186, 187]). In addition, excellent spatial resolution is achieved by the sufficiently low positron energy (395.5 keV) of ^{89}Zr [188]. In particular, the long half-life is ideal for slow accumulation of biologically active molecules, allowing imaging of the targeted biological process after prolonged time or for longitudinal imaging protocols over days following a single dose administration [165]. To date, full size mAbs as well as antibody fragments and engineered fragments have been successfully radiolabelled with ^{89}Zr-ions and have shown favourable biodistribution patterns in numerous clinical settings [189-191]. Although the half-life of ^{89}Zr can match the circulation time of IgGs, the disadvantage lies in the fact that the patient will univocally receive a higher radiation dose. Despite this, immuno-PET is now considered a great diagnostic technique and as long as the radiolabelled complex clears from healthy tissues, the additional dose is considered acceptable [186].

There are numerous reported chelator molecules capable of conjugating ^{89}Zr with mAbs or mAb-derived fragments. By far, the most commonly used chelator is DFO and its derivatives due to the high complexation yields, mild labelling conditions and reasonable stability [152, 154]. DFO can be coupled to bioactive mAbs by click chemistry, thiol conjugation or acid-amide and thiourea formation [192]. The direct conjugation of functionalised DFO to the ε-amino group of lysine on the antibody remains the most valued approach of conjugation. In this study a straightforward approach to conjugate the Pf-Fab to DFO, using *p*-isothiocyanatobenzyl-derivative of DFO (DFO-Bz-NCS), was performed. Although the conjugation process could not be monitored with HPLC (due to the low volume of Pf-Fab available), radio-HPLC of the purified [^{89}Zr]Zr-Pf-Fab confirmed that adequate DFO-Bz-NCS was bound to the Pf-Fab to ensure efficient labelling. The subsequently performed radiosynthesis did

indeed yield a product that met the requirements for pre-clinical application and allowed safe intravenous [^{89}Zr]Zr-Pf-Fab administration into the healthy mice. The high-quality 3D images obtained from the [^{89}Zr]Zr-Pf-Fab-microPET/CT allowed the characterization of the [^{89}Zr]Zr-Pf-Fab's *in vivo* pharmacokinetic behaviour and warranted non-invasive and unprecedented quantification of [^{89}Zr]Zr-Pf-Fab organ uptake and excretion in real time.

Nuclear imaging revealed a considerable amount of [^{89}Zr]Zr-Pf-Fab present in the kidneys as early as 1 h post injection. The TAC further confirmed that this activity increased up to 3 h and did not wash out significantly over time. Favourably-low [^{89}Zr]Zr-Pf-Fab activity could be observed in the liver; contrasting to what was seen for mAbs; images of [^{89}Zr]Zr-IIIB6 revealed high hepatic and splenic accumulation and negligible activity in the kidneys. This correlates with previous findings that macromolecules below the renal threshold (~60 kDa) are excreted by the kidneys while bigger fragments, being resistant to glomerular filtration, remain in the system and are therefore excreted through the hepatobiliary route [164, 193]. However, in the case of [^{89}Zr]Zr-Pf-Fab, the SUV-based TAC showed no significant elimination over 24 h of the tracer in the kidneys. Undesirably high levels of radioactivity residing in the kidney when using lower molecular weight antibody fragments (Fab, scFv, diabody and nanobody) labelled with radiometals has also been previously reported [194]. This high level of radioactivity in the kidneys is usually caused by radio-metabolites produced by lysosomal proteolysis of the parent low molecular weight Fabs and peptides following glomerular filtration and reabsorption in the proximal tubular renal cells [195]. After proteolysis, transporter proteins transport some amino acids across the lysosomal membrane. In the case where radiometals are used to label polypeptides through bifunctional chelators, these can be degraded by lysosomes, yielding metal-chelate-amino acids of which some will not be recognised by transmembrane transporters and will therefore accumulate within the lysosomes [196]. However, additional experiments are required to conclude that this was indeed the pathway responsible for the accumulation of [^{89}Zr]Zr-Pf-Fab-related radioactivity in the kidney. These experiments could include collecting urine samples from the injected animals to test for any radiolabelled by-products that have been excreted. The radioactive distribution within the kidney itself may also be further studied *post-mortem* by way of microtomic organ slicing and autoradiographic organ analysis. There are

various strategies that have proven successful to lower the renal retention including pre- or co-administration of compounds to prevent reuptake by proximal tubule cells, alteration of physiochemical properties of the radionuclide or tracers and the addition of brush border enzyme-cleavable linkers between the radionuclide and targeting agent [197-199].

Another factor that could have contributed to this persistent radioactivity in the kidney, was the method used for the Fab conjugation. Although the direct conjugation of DFO-Bz-NCS to side ε-amino group of lysine on the Fab remains a simple and easy approach, it lacks the capability for site-specific conjugation. The inability to control the location and number of conjugates per antibody can lead to numerous regioisomers and/or heterogenous immunoconjugates which might differ in pharmacokinetic behaviour. It has been shown that different conjugation strategies do influence the elimination and/or accumulation of the radiotracers in the kidneys [200]. Improving the conjugation process, however, could be expensive, time consuming and still cumbersome. Because kidneys are overly sensitive to radiation, they are often the dose limiting organs when it comes to smaller antibody fragments and peptides. Therefore, when developing new antibody fragment-based radiopharmaceuticals, focussing on off-target pharmacology and radiation dosimetry could be considered worthwhile.

Ex vivo biodistribution of tracers is an important tool to quantitatively validate the results of microPET/CT image-guided analyses and calculations. It can also aid in detecting any unforeseen organ toxicity related to the injected dose of the compound. The [^{89}Zr]Zr-Pf-Fab was herein evaluated by comparing its post-mortem biodistribution to that of [^{89}Zr]Zr-IIIB6, which is the only malaria-specific antibody that has previously been evaluated. [^{89}Zr]Zr-IIIB6 was assessed by comparing its *post-mortem* biodistribution to that of the well-studied and clinically-approved tumour agent, nimotuzumab (h-R3) [182]. [^{89}Zr]Zr-IIIB6 showed a similar biodistribution to [^{89}Zr]Zr-h-R3 in context of their *in vivo* stability, lack of organ toxicity and lack of a ‘‘target organ’’ in healthy mice. However, the criteria for evaluating a potential imaging agent in healthy animals, includes low uptake in the healthy tissue in the area where the eventual target needs to be detected (i.e., low non-target uptake). Therefore, the high uptake in liver and spleen (high non-target uptake) limits the potential of [^{89}Zr]Zr-IIIB6 as a malaria imaging tracer due to the expected high parasite load in these organs in

the case of malaria-infected animals. It was therefore deemed sufficient to use [^{89}Zr]Zr-IIIB6 as a control model to evaluate whether [^{89}Zr]Zr-Pf-Fab has better properties as an *in vivo* tracer than [^{89}Zr]Zr-IIIB6 (i.e., low or impersistent radioactivity at the sites where malaria parasite sequestration is desired).

Both [^{89}Zr]Zr-IIIB6 and [^{89}Zr]Zr-Pf-Fab had significantly lower uptake in the femur than that of [^{89}Zr]Zr-oxalate. Free ^{89}Zr is known to behave like a bone seeker meaning it will become embedded into the bone if released from an antibody-chelate complex [186, 192]. Clinically this accumulation can act as a dose-limiting characteristic of ^{89}Zr-PET, in general. [^{89}Zr]Zr-oxalate, which acts similarly to free ^{89}Zr when it comes to having a high affinity for the bone, is therefore used as a reference to evaluate the *in vivo* stability of a [^{89}Zr]Zr-Fab and [^{89}Zr]Zr-IIIB6 conjugate. This finding indicates that both the antibody complexes were stable *in vivo*.

There was a discernible lower uptake of [^{89}Zr]Zr-Pf-Fab in the lung to that of [^{89}Zr]Zr-IIIB6 and [^{89}Zr]Zr-oxalate. This opens the possibility to use [^{89}Zr]Zr-Pf-Fab as a potential tracer that can specifically be used for non-invasive visualisation of pulmonary sequestration of *P. falciparum*-iRBCs in real time. This confirmed the image-derived VOI results where significant decrease in concentration of [^{89}Zr]Zr-Pf-Fab was observed at 6 h post-injection.

A MGC34-derived [^{89}Zr]Zr-Pf-Fab is presented to have superior potential over [^{89}Zr]Zr-IIIB6 as a prospective *in vivo* imaging agent for the study of malaria-related processes in real time. Thus, future studies are warranted to explore the differences in biodistribution occuring in mice with *P. falciparum* infection using non-invasive [^{89}Zr]Zr-Pf-Fab-PET/CT imaging.

Chapter 3

Identifying scFvs specific to whole *P. falciparum*-infected erythrocytes through phage display technology

3.1 Introduction

Although IgG mAb tracers have been an effective tool in the field of therapeutics, diagnostics and targeted drug delivery systems in various diseases, the use of mAb tracers have several drawbacks. Monoclonal, target-specific antibodies are generally developed through hybridoma technology or by antibody engineering [201]. Regardless of all the progress made with hybridoma technology, the process remains complex, tedious, and unpredictable. MAbs also have several limitations in *in vivo* applications mainly due to their high molecular weight and need for radioisotopes with longer half-lives to reach optimal target-to-background ratio [155]. Genetically engineered antibody technology has allowed the easy, less expensive and stable production of recombinant antibody fragments that are smaller than conventional mAbs whilst retaining the regions responsible for antigen recognition and binding e.g., Fab, scFv, diabodies, minibodies, tetrabodies and single-domain antibodies [202, 203]. These smaller antibody fragments, in particularly scFvs, have become popular in *in vivo* analysis mainly due to their favourable pharmacokinetic properties including improved tissue penetration and blood clearance and reduced immunogenicity [162, 163, 203]. ScFvs, with a size of ~25 kDa, consists of variable regions of the VH and VL chains connected with a short polypeptide linker [202]. These small recombinant antibody fragments have shown to have better pharmacokinetic properties than full-length antibodies in *in vivo* nuclear imaging [162]. The scFv's improved deep tissue penetration and fast blood clearance without compromising the binding affinity minimizes exposure to healthy tissues and the accumulation of radiotracers in organs allowing the generation of high-resolution images [162, 204, 205].

3.1.1 Phage display technology

Various expression systems have allowed the successful production of scFvs [202]. Phage display, a recombinant antibody technology based on the ability to express and

display antibody fragments on the surface of phages, has become a popular *in vitro* display system to study protein functions and biological processes of infectious diseases [206, 207]. This high-throughput technology allows screening large numbers of phages, expressing thousands of different antibodies, that interact with a target molecule without any prior knowledge about structure or sequence of its epitope [208]. Phages can display small peptides (peptide display) from 6 amino acids up to larger proteins (i.e., antibody display) of ~100 kDa [209-211]. Before one can use phage display technology, a library consisting of a collection of different targeting vectors/ligands must first be designed and constructed. Once a successful library is made and amplified it serves as an unlimited source from which to select specific peptides/antibodies [212]. Most existing recombinant libraries are based on human immunoglobulin genes, however, phage displayed antibody fragments can be generated from a number of animal species [213-216]. Bacteriophages which infect *Escherichia coli* such as Ff filamentous phage, T7 and Lambda are used. In this study, the M13 filamentous bacteriophage (M13) phagemid vector (pHEN1) was used where the antibody fragment is displayed on the phage surface as a coat protein 3 (pIII) fusion protein (Figure 3.1) [202]. These antibodies have the potential to be used in immunodiagnostics, proteomics, and therapies.

During the phage display screening/panning process, the definite aim pertains to the identification of those phages from a pool of diverse phages that bind with high affinity to the target antigen of interest. The process usually consists of multiple rounds of binding of phages to target antigen, washing to remove unbound phages followed by elution and recovery of the bound phages. After each round, these eluted phages are amplified by infection into *E. coli* before they are subjected to the next selection round. In the end, soluble antibody fragments are produced and then the binding to the antigen of interest is characterized [202].

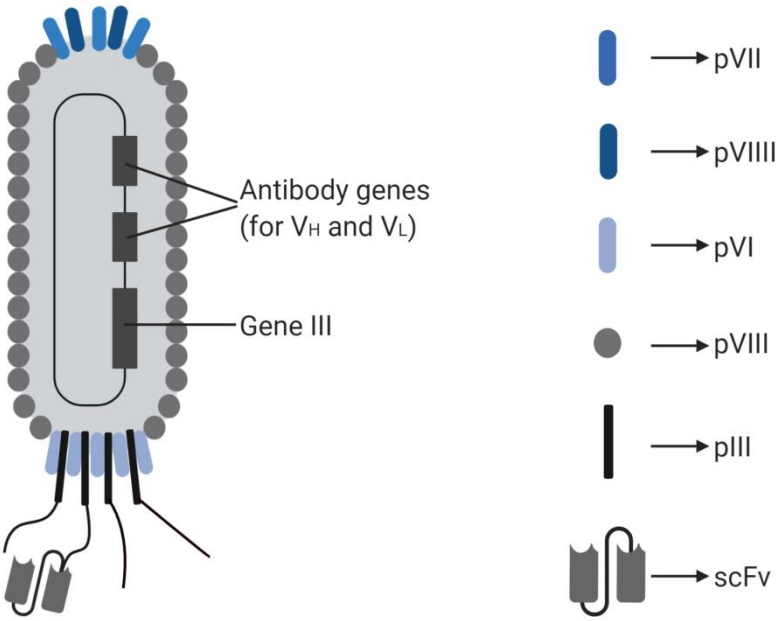

Figure 3.1. Structure of filamentous phages displaying scFv fragments on its surface. The genome contains 9 genes that encode 11 proteins. There are 5 of these proteins that are coat proteins with gene 3 protein (pIII), gene 6 protein (pVI), gene 7 protein (pVII) and gene 9 protein (pVIIII) as minor coat proteins while gene 8 protein (pVIII) is a major coat protein. Single-chain variable fragment (scFv) is fused to the gene 3 protein (pIII). Created with BioRender.com.

Phage display technology has emerged as a tool to support research of malaria mostly focussing on biopanning against selective malaria expressed proteins including erythrocyte binding ligand-1 (EBL-1), duffy binding protein (DBP), ring-infected erythrocyte surface antigen (RESA), merozoite surface protein (MSP), and apical membrane antigen-1 (AMA1) [217-220]. By utilizing only a specific protein as the target for panning, the use of the antibody as an imaging agent to study multiple life cycles of the disease, is limited. Previous studies using peptide display on whole iRBCs have yielded *P. falciparum* peptides that bind specifically to the whole cell [221]. In this study we set out to screen a scFv phage library for antibodies that bind to whole iRBCs. As the parasite expresses variable proteins in each life cycle, the goal is to find scFvs binding to a conserved surface protein of late-stage trophozoite and schizont-infected erythrocytes (T-iRBC). The *Nkuku*® - and *Inshi*® libraries, derived from chicken and ostrich variable heavy and light chains, respectively, have successfully produced recombinant antibodies for application in various diseases including foot-and-mouth disease, bluetongue disease, and bovine TB [222-224]. Here, the M13 phage display system used was the *Nkuku*® library from Van Wyngaardt *et al*. (2004) and *Inshi*® library (unpublished) that was screened for scFvs specific T-iRBCs [213].

These scFvs express a c-myc tag that allows detecting the antibody fragments via an anti-c-myc antibody (clone 9E10).

3.2 Materials and Methods

3.2.1 *In vitro* cultivation of asexual *P. falciparum* parasites

Ethical approval for *in vitro* cultivation of *P. falciparum* parasites was granted by the University of Pretoria Research and Ethics Committee, Health Science Faculty (No: 120821-077). Drug sensitive *P. falciparum* 3D7 (BEI resources/MR4) parasite cultures were maintained with moderate shaking (~60 rpm) at 37°C in human erythrocytes (blood type A^+ or O^+) at a haematocrit of 5%, in complete culture medium [RPMI 1640 medium (Sigma-Aldrich, Johannesburg, South Africa) supplemented with 25 mM 4-(2-hydroxymethyl)-1-piperazineethanesulfonate (HEPES) (Sigma-Aldrich, Johannesburg, South Africa), 2% (w/v) D-glucose (Sigma-Aldrich, Johannesburg, South Africa), 200 µM hypoxanthine (Sigma-Aldrich, Johannesburg, South Africa), 24 µg/mL gentamycin (Fresenius-Kabi, Bad Homberg, Germany), 0.2% (w/v) sodium bicarbonate (Sigma-Aldrich, Johannesburg, South Africa) and 0.5% (w/v) AlbuMAX II (Invitrogen, Thermo Fisher Scientific, Waltham, Massachusetts, USA)] and gassed with 5% O_2, 5% CO_2, and 90% N_2 (Afrox, Johannesburg, South Africa) [225]. For optimum growth, the media was replaced daily with fresh, pre-warmed medium and parasitaemia monitored under a light microscope on Giemsa-stained thin blood smears, maintained at 3-5%. Synchronous asexual parasites were obtained with 5% (w/v) D-sorbitol (Sigma-Aldrich, Johannesburg, South Africa) synchronisation of ring-stage parasites for two consecutive life cycles [226]. A mixture of late-stage trophozoites and schizont-infected erythrocytes (T-iRBCs) were enriched from uninfected erythrocytes (RBCs) to >90% parasitaemia using magnetic separation [227, 228]. The *P. falciparum* cultures were loaded onto CS columns (Miltenyi Biotec, California, United States of America) mounted on the VarioMACS (Miltenyi Biotec GmbH, Bergisch Gladbach, Germany) separator. Uninfected RBCs were washed away 3x using culture medium (37°C). The CS column was removed from the magnetic field and the T-iRBCs eluted. Enrichment was monitored via a haemocytometer.

3.2.2 Biopanning phage display libraries on T-iRBCs

Previous established libraries (*Nkuku*® and *Inshi*®) were utilized with minor adjustments to pan a phage display collection of immunoglobulins to whole T-iRBCs according to a combination of previously described methods (Figure 3.2) [221, 229].

Details of the library construction have been described previously [213]. To eliminate cross-reactivity of phages between the target T-iRBCs and non-target erythrocytes, the phage libraries were firstly pre-adsorbed with ring-infected and uninfected RBCs (Figure 3.2). Of a synchronous ring-infected culture (~2 x 10^8 cells consisting of a mixture of ring-infected and uninfected RBCs), the culture media was removed by centrifugation (3500 x*g*, 5 min) and the cells were resuspended in 3.5 mL phosphate-buffered saline (1x PBS, 137 mM NaCl, 2.7 mM KCl, 10 mM phosphate, pH 7.40) containing 4% (w/v) bovine serum albumin (BSA) in PBS and incubated with 3 mL phages (1 x 10^{12} transducing units (TU)) at 37°C for 30 min with gentle shaking at ~40 rpm on an orbital shaker. The cells containing bound phages were removed by centrifugation for 5 min at 3500 x*g* (SL 8R centrifuge, Thermo Fisher Scientific, Waltham, Massachusetts, USA) and the unbound phages were collected in the supernatant and used for the next round of pre-adsorption.

After the three rounds of pre-adsorption were completed, the unbound phages were panned to enriched T-iRBCs. Enriched T-iRBCs (>90% parasitaemia, >1 x 10^8 cells) were blocked with 2% (w/v) BSA in PBS for 1 h at 37°C with gentle shaking at ~40 rpm. The pre-adsorbed phages were incubated with the blocked T-iRBCs at 37°C for 30 min at ~40 rpm. The sample was centrifuged and washed 5 times with 10 mL 0.2% (w/v) BSA in PBS followed by 5 washing steps with 10 mL PBS. The washed cell/phage pellet was resuspended in 500 µL PBS and 50 µL Trypsin (1 mg/mL in PBS) to elute the bound phages. The sample was incubated at 37°C for 20 min followed by centrifugation at 13000 x*g* for 10 min (SL 8R centrifuge, Thermo Fisher Scientific, Waltham, Massachusetts, USA) to allow the phages to be accessible in the supernatant.

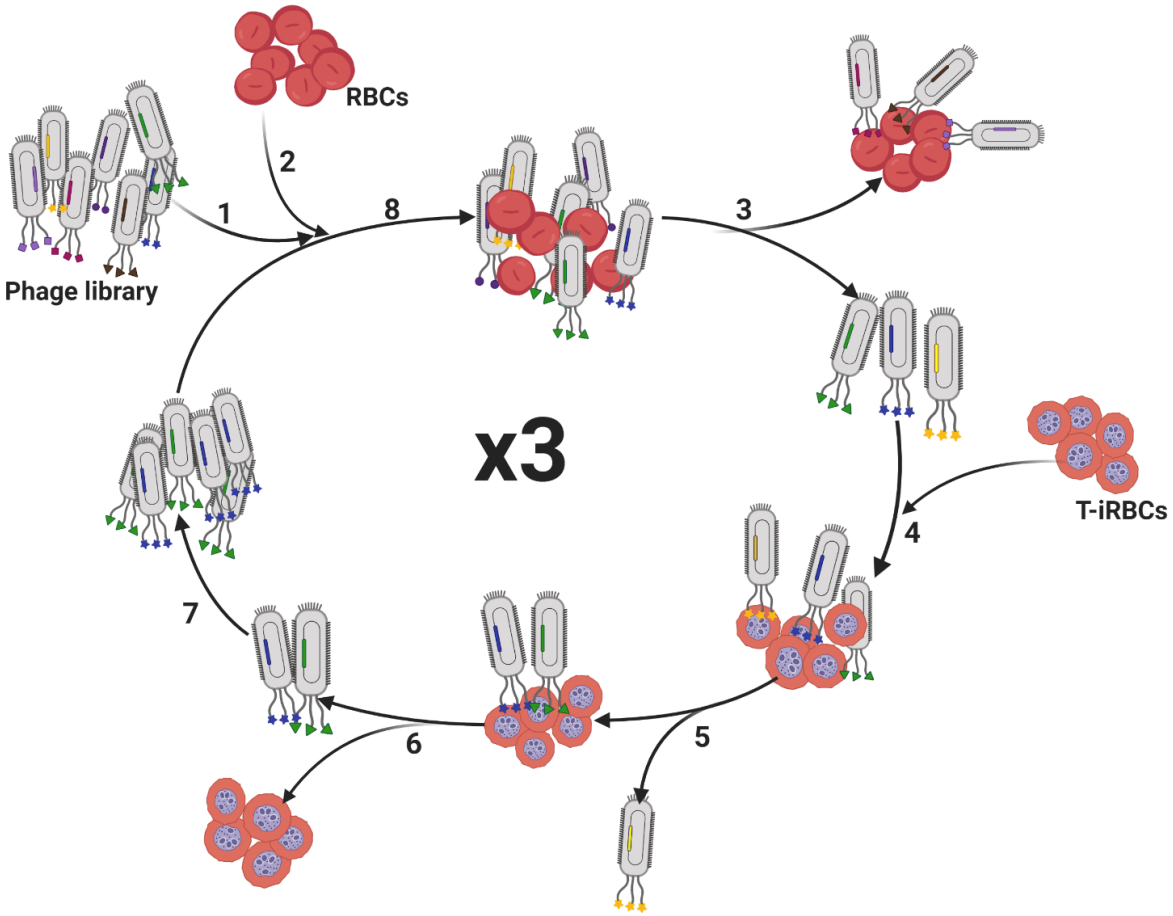

Figure 3.2. Panning phages specific to late-stage trophozoite- and schizont-infected erythrocytes. Phages from the *Nkuku*®- and *Inschi*® libraries (1) were pre-adsorbed to uninfected- and ring-infected erythrocytes (2). The phages that bound to the uninfected erythrocytes (RBCs) were removed (3). The unbound phages were panned with late-stage trophozoite- and schizont-infected erythrocytes (T-iRBCs) (4). The unbound phages were removed (5) which allowed separating the bound phages from the T-iRBCs (6). This pool of T-iRBC-specific phages were amplified (7) and pre-adsorbed again (8) with fresh erythrocytes (2). The panning was repeated three times. Created with BioRender.com.

To amplify the phages for the next round of panning, the eluted phages were re-infected into 5 mL of exponentially growing TG1 phage display electrocompetent *Escherichia coli* cells (OD_{600} of ~0.5, determined by GeneQuant (General Electric Healthcare, Chicago, Illinois, United States of America)). The volume was made up to 10 mL with 2x TY medium (1.6% (w/v) tryptone, 1.0% (w/v) yeast extract and 85 mM NaCl) supplemented with 100 µg/mL ampicillin (Sigma-Aldrich, Johannesburg, South Africa) and 2% (w/v) glucose and incubated stationary for 15 min at 37°C to allow the phages to infect the cells. The infected TG1 culture was plated on TYE (1.5% (w/v) agar, 1.0% (w/v) tryptone, 2.5% (w/v) yeast extract and 137 mM NaCl) plates containing 2% (w/v) glucose and 100 µg/mL ampicillin (TYE A/G plates) and incubated

overnight at 30°C. After the overnight incubation, a small volume of TY media was added to the plates and the colonies were carefully scaped off and 20 µL was used to inoculate in 50 mL fresh 2x TY medium (supplemented with 100 µg/mL ampicillin and 2% (w/v) glucose) and grown until an OD_{600} of ~0.5 was reached. The remainder of the scraped cells were stored in 15% (v/v) glycerol at -70°C. The phages (5 mL) were rescued by the addition of M13KO7 helper phages (ratio of helper phage:bacteria = 20:1), amplified overnight at 30°C whilst shaking at 240 rpm, and recovered from the supernatant via precipitation with 1/5 volume polyethylene glycol (PEG) 6000/ 2.5 M NaCl. The precipitated phages were then collected by centrifugation at 10000 x*g* for 15 min followed by resuspending the pellet in 1mL PBS and stored at -70°C in 15% (v/v) glycerol. The unbound phages were subjected to three rounds of biopanning (pre-adsorption to RBCs followed by panning to enriched T-iRBCs).

3.2.3 Polyclonal phage binding to T-iRBCs

After three rounds of bio-panning, the polyclonal phage populations of each round were tested for binding to T-iRBCs and evaluated whether enrichment for phages specific to T-iRBCs had taken place after each selection step. Enzyme-linked immunosorbent assay (ELISA) measurements were performed adopting methods previously described by van Wyngaardt *et al.* (2004); with the main difference that RBCs or T-iRBCs served as the antigens that were immobilised onto the immunoplates (Nunc Maxisorp, AEC-Amersham, Sandton, South Africa) [213]. To enable cell trapping, Maxisorp microtitre plates were coated for 1 h at 37°C with 50 µl/well of 10 µg/mL anti-red blood cell antibody (ab34858) (Abcam, Cambridge, UK) which has previously been purified by a Protein G HP SpinTrap (General Electric Healthcare, Johannesburg, South Africa). Non-specific binding sites of the antibody-coated wells were blocked with 2% (w/v) fat-free milk powder (2% MPBS) in PBS for 1 h at 37°C. Thereafter, T-iRBCs (or uninfected RBCs as control), suspended in 2% MPBS, were added to the antibody-coated wells and incubated for 1 h at 37°C. The excess cells were washed off gently three times with 2% MPBS. In each well, phages from each pool (~5 µL phages (~3 x 10^{13} phage particles/mL) in 45 µL 2% MPBS) were added and incubated for 1 h at 37°C. The unbound phages were removed by three gentle washes with 2% MPBS. To screen for the presence of phages, a 1/1000 dilution of 0.1 mg/mL B62-FE2-HRP (horse radish peroxidase (HRP)-conjugated murine monoclonal antibody against M13 filamentous phage coat protein VIII, Abcam,

Cambridge, UK) was added and incubated for 1 h at 37°C. The excess antibody was removed by three gentle washes in 2% MPBS as before. To spectrophotometrically determine the quantity of HRP, freshly prepared ortho-phenylenediamine (OPD) substrate (Sigma-Aldrich, Johannesburg, South Africa) (5 mg OPD tablet in 10 mL 0.1 M citrate buffer (pH 4.5) and 0.5 µL/mL of 30% H_2O_2) was added. After the colour development (± 30 min at room temperature), the reaction was stopped with 2 N H_2SO_4 and the absorbance values were subsequently determined at 492 nm.

3.2.4 Preparing single soluble scFv clones in masterplates

An adapted method of Fahr *et al*. (2020) was used to produce monoclonal scFvs in a microtiter platform [229]. To prepare masterplates containing single scFv clones, titrations of the TG1 bacteria from the third panning round were created and grown overnight at 30°C on TYE A/G plates. Individual colonies were picked and each suspended in a separate well of a 96-well plate containing 100 µL 2x TY medium (supplemented with 100 µg/mL amplicillin (Sigma-Aldrich, Johannesburg, South Africa), 2% (w/v) glucose and 10% (w/v) glycerol) and grown for 12 h at 30°C whilst shaking at 220 rpm. These plates (from now on denoted as masterplates) were stored at -70°C until further use. For induction of TG1 cells to produce soluble scFv, 5 µL from each well of the masterplates was resuspended in 150 µL 2x TY media supplemented with 100 µg/mL ampicillin, 1 mM isopropyl-thio-β-D-galactosidase (IPTG) and incubated for 12 h at 30°C whilst shaking at 220 rpm. To retrieve the secreted scFvs, the cells were pelleted at 600 x*g* (SL 8R centrifuge, Thermo Fisher Scientific, USA) and 25 µL of the supernatant was used to evaluate different strategies of screening monoclonal scFvs to bind to the surface of T-iRBCs.

3.2.5 Screening monoclonal scFvs to bind to the surface of T-iRBCs

3.2.5.1 Monoclonal scFv binding to surface of trapped T-iRBCs

Microtiter plate (MTP)-based ELISA has been the most widely used process for screening single soluble scFvs as it allows a straightforward approach to screen a large amount of scFv clones [230, 231]. ELISA plates were coated with RBCs or T-iRBCs as described in section 3.2.3. Single soluble scFvs (25 µL scFvs in 25 µL 4% MPBS) were added to the cells and incubated for 1 h at 37°C. To limit the loss of cells from the ELISA plates, all washing steps was performed by gently adding 2% MPBS using a pipette boy set on the slowest speed followed by gently inverting the ELISA

plates. The presence of scFv binders was detected with two different ELISA detection methods (Figure 3.3).

Detection of scFv using direct anti-c-myc antibody-HRP signalling (Figure 3.3.A). To screen for the presence of scFvs, a 1/1000 dilution (in 2% MPBS) of a 0.5 mg/mL HRP-conjugated anti-c-myc antibody (clone 9E10) (Roche Pharma, Basel, Switzerland) was added (50 µL) to each well followed by an incubation for 1 h at 37°C. The excess antibody was washed off carefully with 2% MPBS. OPD was added as substrate and wells were analysed as described in section 3.2.3.

Detection of scFv using sequential anti-c-myc antibody / goat anti-mouse H&L-antibody-AP (Figure 3.3.B). An anti-c-myc antibody (clone 9E10) was diluted 1/1000 (in 2% MPBS) from 1 mg/mL stock and 50 µL was added to each well and further incubated for 1 h at 37°C. The excess antibody was washed off gently with 2% MPBS. A 1/5000 dilution (in 2% MPBS) was made from the 1 mg/mL alkaline phosphatase (AP)-conjugated goat anti-mouse (IgG) H&L secondary antibody (ab97020) (Abcam, Cambridge, UK) and 50 µL was added to each well and further incubated for 1 h at 37°C. The excess antibody was washed off gently with 2% MPBS. Para-nitrophenylphosphate (pNPP) substrate was freshly prepared by dissolving a 5.0 mg pNPP tablet (Southern Biotech, Birmingham, Alabama, USA) in 5 mL substrate buffer (24.5 mg $MgCl_2.6H_2O$ and 48 mL diethanolamine in a final volume of 500 mL deionised H_2O, pH adjusted to 9.8 with 5 N HCl). Of the freshly prepared pNNP substrate, 50 µL was added to each well and after a colour forming process (± 30 min at room temperature) the reaction was stopped by adding 3 N NaOH and the absorbance measured at 405-410 nm.

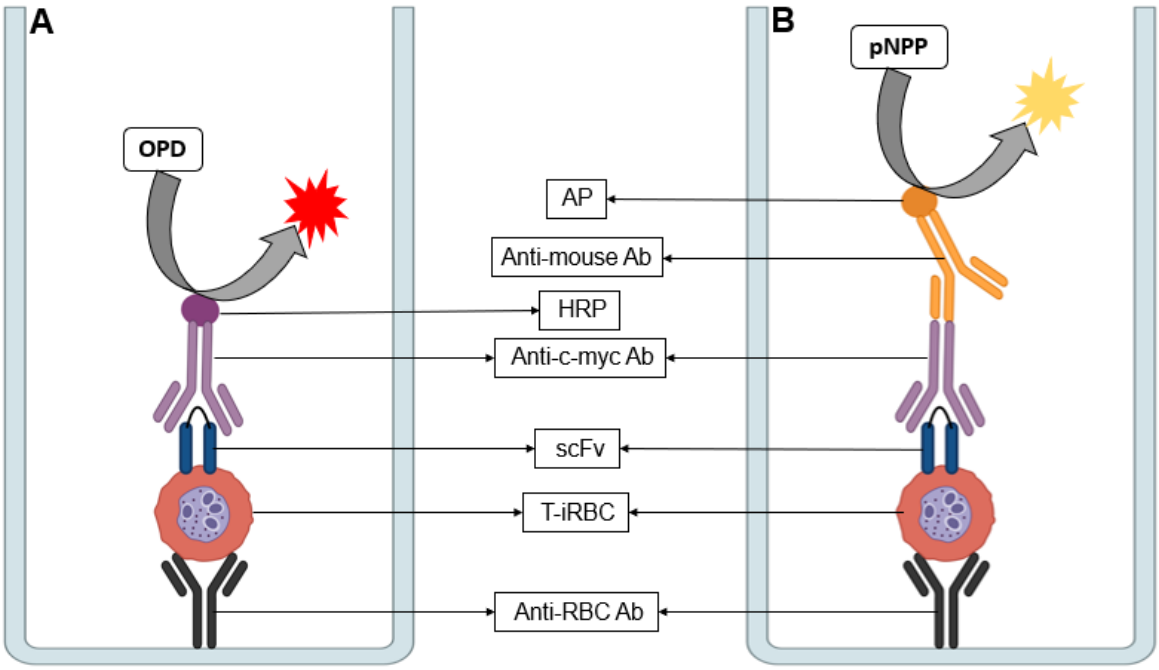

Figure 3.3. Monoclonal scFv trapping to surface-bound T-iRBCs and ELISA signaling strategies. Maxisorp immunoplates were coated with an anti-red blood cell antibody followed by trapping of T-iRBCs. Each single-clone derived scFv (one clone per well) was incubated with the cells and the unbound scFvs washed off gently. The presence of each scFv was detected by A) using direct anti-c-myc antibody-HRP signaling or B) using sequential anti-c-myc antibody and goat-anti-mouse (IgG) H&L secondary antibody-AP signaling. Rabbit polyclonal anti-red blood cell antibody (ab34858) (Anti-RBC Ab); late-stage trophozoite- and schizont-infected red blood cells (T-iRBC); single-chain variable fragment (scFv); horseradish peroxidase (HRP); alkaline phosphatase (AP); ortho-phenylenediamine (OPD); para-nitrophenylphosphate (pNPP); anti-c-myc antibody specific for c-myc epitope tag (9E10) (Anti-c-myc Ab); goat-anti-mouse (IgG) H&L secondary antibody (Anti-mouse Ab). Created with BioRender.com.

3.2.5.2 Monoclonal scFv binding to suspended T-iRBCs

The binding potential of single soluble scFvs was also assessed using T-iRBCs in suspension. Bigger volumes of scFvs were prepared by adopting methods previously described by Rakabe *et al*. (2011) [232]. Briefly, bacterial clones from the masterplates prepared section 3.2.4 (stored at -70°C) were grown in 10 mL 2x TY (supplemented with 100 µg/mL ampicillin and 2% glucose) overnight at 37°C with vigorous shaking at 220 rpm. The following day, the cultures were diluted 1/100 in 10 mL 2x TY (supplemented with 100 µg/mL ampicillin and 2% glucose) and grown at 37°C until an OD_{600} of ~0.9 was reached. The cells were collected by centrifugation at 4000 x*g* (SL 8R centrifuge, Fisher Scientific, Waltham, Massachusetts, USA) for 10 min and resuspended in 2 mL 2x TY supplemented with 100 µg/mL ampicillin and 1 mM IPTG. The cultures were incubated overnight at 30°C shaking at 220 rpm. The next day, the cultures were centrifuged at 4000 x*g* (SL 8R centrifuge, Fisher Scientific, Waltham,

Massachusetts, USA) for 15 min to enable retrieving scFvs in the supernatant. Of the soluble scFvs clones, 80 µL was added to 80 µL enriched T-iRBCs (>90% T-iRBCs in 4% MPBS) and incubated for 1 h at 37°C. The unbound scFvs were washed off by centrifugation at 3500 x*g* (MiniSpin plus, Eppendorf, Hamburg, Germany) for 5 min. To detect the presence of bound scFvs, anti-c-myc antibody / secondary goat anti-mouse IgG H&L-antibody-AP signalling (as described above in section 3.2.5.1) was used. The excess antibodies were washed off by centrifugation at 3500 x*g* (MiniSpin plus, Eppendorf, Hamburg, Germany) for 5 min. After the final wash, 80 µL of the chromogen pNPP was used to detect the presence of scFvs. The cells were removed by centrifugation and the supernatant was used to read the absorbance at 405-410 nm.

The same scFv clones were screened similar as above with an additional step where the clones were firstly pre-adsorbed to uninfected RBCs (11% haematocrit in 4% MPBS) for 30 min at 37°C, before screening them on dispensed T-iRBCs as before.

3.2.6 Confocal microscopy

Confocal microscopy imaging was carried out to ascertain binding of potentially positive single-clone soluble scFvs to T-iRBCs [14]. *P. falciparum* (strain 3D7) was cultivated as described in section 3.2.1. *P. falciparum* cultures (5% haematocrit, 5-7% parasitaemia) containing a majority of T-iRBCs, were harvested and washed three times with PBS and treated with a blocking buffer (1% (w/v) BSA in PBS) for 30 min at room temperature. After the blocking buffer was removed by centrifugation (SL 8R centrifuge, Thermo Fisher Scientific, Waltham, Massachusetts, USA) at 3500 x*g* for 2 min, 350 µL scFvs were added and incubated with the T-iRBCs for 1 h at 37°C. Unbound scFvs were removed by washing three times with PBS at 3500 x*g* for 2 min (MiniSpin plus, Eppendorf, Hamburg, Germany). The cells were resuspended in 1.5 mL PBS and loaded onto precoated poly-L-Lysine (0.1 mg/mL) (Sigma-Aldrich, Johannesburg, South Africa) coverslip in a 6-well tissue culture plate. To allow the parasites to adhere in a monolayer on the coverslips, the suspension was centrifuged (SL 8R centrifuge, Thermo Fisher Scientific, Waltham, Massachusetts, USA) at 300 x*g* for 3 min. The PBS was removed, and unattached cells were washed off carefully with PBS. The cultures were fixed for 30 min using PBS containing 4% (v/v) formaldehyde, 0.025% (v/v) glutaraldehyde. To enable the visualisation of scFvs, an anti-c-myc antibody (clone 9E10) was conjugated to fluorescein-5-isothiocyanate

(FITC) using the FluoroTag FITC conjugation kit (Sigma, Missouri, USA) according to the manufacturer's protocol. This FITC-conjugated antibody (1:14 dilution in PBS/ 0.1% Tween 20 (v/v)) was incubated overnight (4°C in darkness) with the respective samples. The slides were rinsed three times with PBS to remove any excess antibody. Parasite DNA was additionally stained with Hoechst 33342 (Invitrogen, Thermo Fisher Scientific, Johannesburg, South Africa) (1:100 dilution in PBS) at room temperature for 30 min in the dark. To remove excess Hoechst, the coverslips were washed and rinsed three times and prepared for microscopy by placing the cell-coated coverslip face down on a normal microscopy slide in fluoroshield (Sigma-Aldrich, Missouri, USA). The slides were evaluated with fluorescence confocal microscopy with a Confocal Laser Scanning Microscope 880 (Carl Zeiss GmbH, Oberköchen, Germany) using a Plan-Apochromat 100x/1.46 oil DIC M27 Elyra objective. The pinhole size was set to 1.1 AU. Images of 512 x 512 pixels were acquired using PMTs detectors. Hoechst was detected at 410-497 nm through the blue channel and FITC was detected at 493-634 nm through the green channel. Images were acquired with a Zeiss Axiocam 506 mono camera controlled with Zeiss ZEN 3.2 blue edition software (Carl Zeiss GmbH, Jena, Germany). ImageJ version 1.52v open-source software (National Institutes of Health, Bethesda, Massachusetts, USA) was used for further editing images (blue channel image displayed value = 0-129; green channel image displayed value = 0-225).

3.3. Results

3.3.1 Polyclonal phage binding to T-iRBCs

With biopanning, the phage displayed scFvs that are specific to the antigen (T-iRBCs in our case) are enriched through several rounds. This allows the addition of counter selection where scFvs binding to unwanted epitopes can firstly be removed. In this case, pre-adsorption was done with uninfected RBC and ring-infected RBCs. After three rounds of panning to evaluate whether enrichment of phages binding to T-iRBC have taken place, the polyclonal phage pools recovered after each round were screened for binding to T-iRBCs by polyclonal phage ELISA (Figure 3.4).

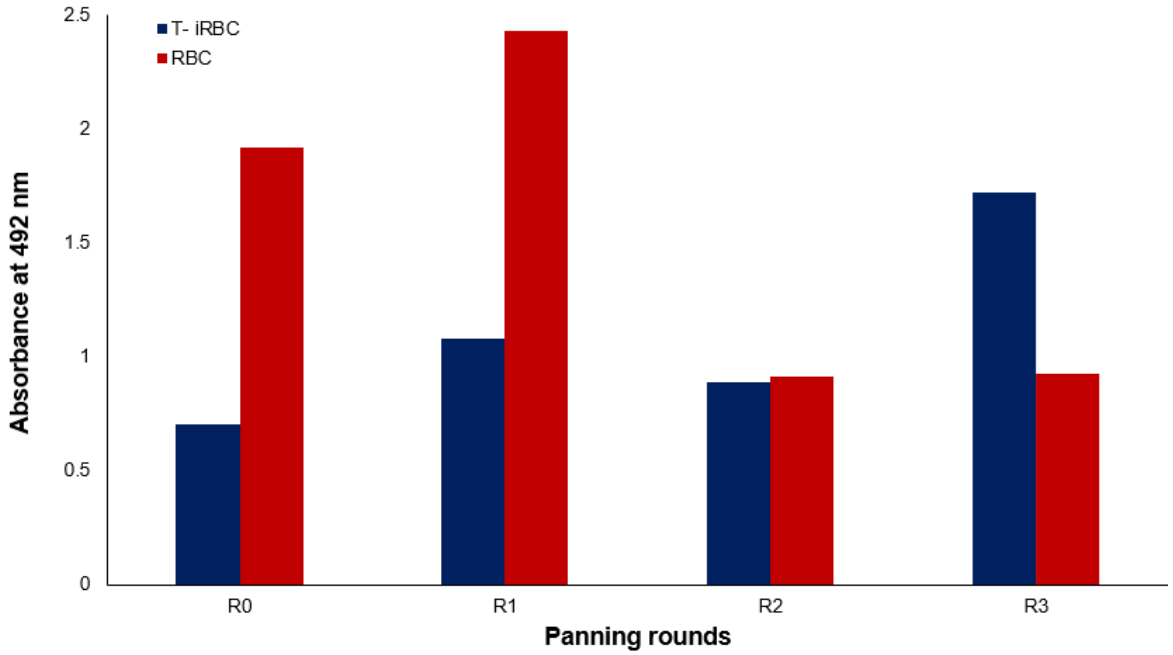

Figure 3.4. ELISA of polyclonal phage binding to T-iRBCs. After each round (R1-R3) of panning, the recovered polyclonal phage pools were screened for binding to RBCs and T-iRBCs. An HRP-conjugated anti-M13 antibody (B62-FE2-HRP) was used to detect the presence of phages. R0 represents the initial *Nkuku*® and *Inshi*® libraries prior to panning. Late-stage trophozoite- and schizont-infected red blood cells (T-iRBC); red blood cells (RBC).

The initial *Nkuku*® and *Inschi*® library and the pooled phages of round 1 showed a higher preference to RBC *vs.* T-iRBCs. By panning round 2, the phages bound similarly to the RBC (absorbance of 0.45) compared to T-iRBCs (absorbance of 1.1). After round 3, the phage pool preferentially bound to T-iRBC (absorbance of 1.73) *vs*. RBC (absorbance of 0.92) indicating that this phage pool was successfully enriched for phages that bind specifically to T-iRBCs.

3.3.2 Screening monoclonal scFvs to bind to the surface of T-iRBCs

Since enrichment of phages for binding to T-iRBC stages was observed after three rounds of phage panning, single clone scFvs were screened to T-iRBCs to identify individual clones that bind favourably to T-iRBCs. Screening for single soluble scFvs can be done with the same method as described above for panning. However, using cells in suspension would limit the ability to screen hundreds of different clones simultaneously. Magnetic-based, semi-automated screening has recently been discovered and allows high-throughput selection of antibodies by immobilizing cells to a microtiter plate however, this process has proven to be incredibly expensive [233]. Here, two different strategies (described in section 3.2.5.1 and section 3.2.5.2) were used in an attempt to identify scFvs specific to T-iRBCs.

3.3.2.1 Monoclonal scFv binding to surface of trapped T-iRBCs

MTP-based ELISA has been the most widely used approach for screening large amount of single soluble scFvs. The first strategy was therefore based on immobilisation of RBCs to microtiter plates. Approximately 90 scFv clones were screened using ELISA systems as described earlier in section 3.2.5.1. For the first monoclonal scFv ELISA, an HRP-conjugated anti-c-myc antibody was used for the detection of scFvs. Possible substrates for HRP includes 3,3',5,5'-tetramethylbenzidine (TMB) and OPD. Although TMB is about ten times more sensitive than OPD, excessive erythrocyte lysis was observed which negated the use of this detection system. Therefore, OPD was chosen as the substrate to detect the presence of scFvs [234]. To evaluate the potential of this detection system, the HRP-conjugated anti-c-myc antibody was incubated with immobilised T-iRBCs and uninfected RBCs (to represent the background signal) in the absence of scFvs (Figure 3.5).

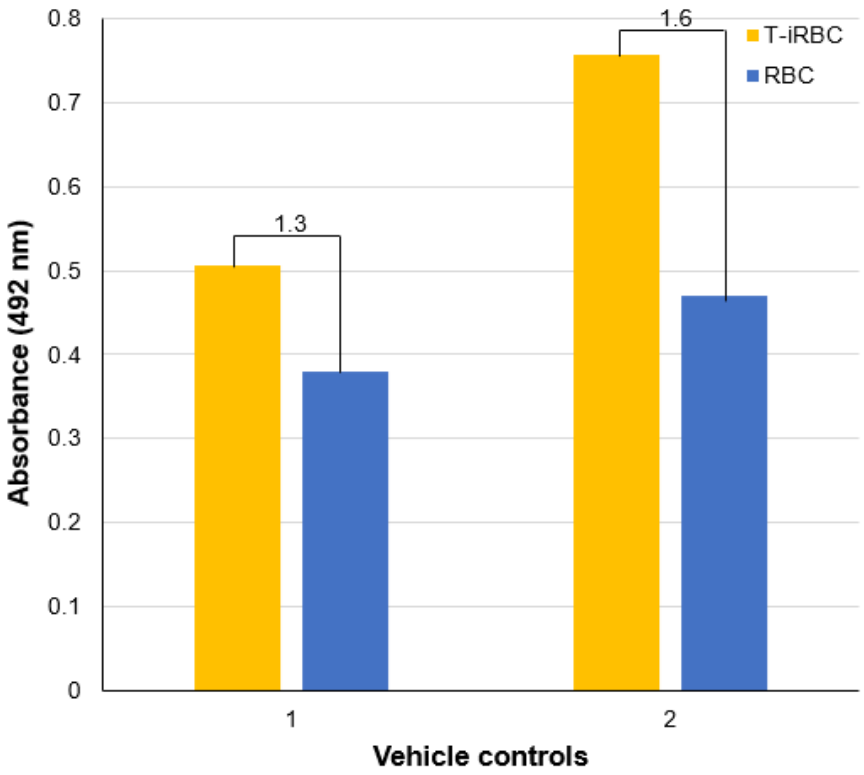

Figure 3.5. Evaluating monoclonal ELISA using direct anti-c-myc antibody-HRP signaling for screening of scFv clones. In the absence of scFvs**,** HRP-conjugated anti-c-myc antibody was incubated with uninfected red blood cells (RBCs) and late trophozoite- and schizont-stage infected red blood cells (T-iRBC), respectively. OPD was used as the substrate and the absorbance measured at 492 nm. The screening was performed in duplicate.

The signal of the controls *vs.* background ranged between 1.3 and 1.6, indicating a large contribution of background signal from the uninfected RBC population that is recognised by the HRP-conjugated anti-c-myc antibody (Figure 3.5). Moreover, the repeatability between assays was questionable since signal variation between 0.5 and 0.75 was observed for the two controls analysed.

The assay was therefore cautiously further evaluated by screening multiple single clone scFvs against T-iRBCs, whilst simultaneously screening the same scFvs against uninfected RBCs to correct for background interference (Figure 3.6).

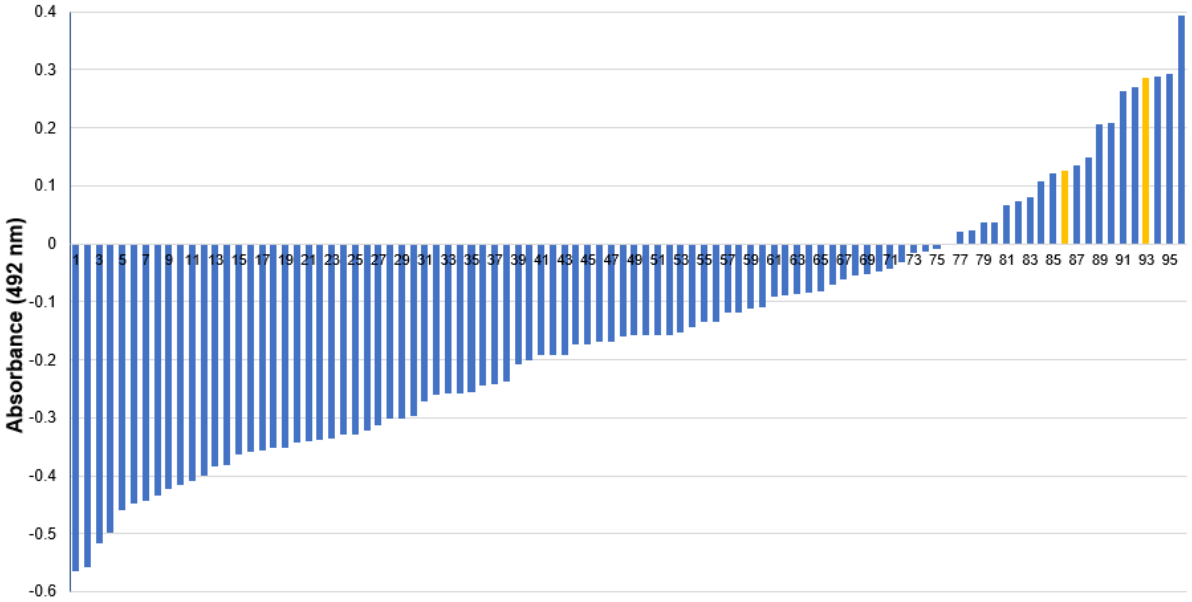

Figure 3.6. Screening of single scFv clones against *P. falciparum*-infected RBCs with monoclonal ELISA. Single clones (1-96) were screened with uninfected red blood cells (RBCs) (control) and late trophozoite- and schizont-stage infected red blood cells (T-iRBC), respectively. The control samples that contained no scFvs are represented by 86 and 93 (yellow bars). Bound HRP-anti-c-myc antibody-scFv complexes were detected by using OPD as the substrate and the absorbance measured at 492 nm. The results are expressed as the absorbance values of the control RBCs subtracted from those of the T-iRBCs.

The low signal to background ratio (RBCs to T-iRBCs) was observed throughout the screening of the scFv clones, resulting in only 20% of the clones screened presenting with an observable positive signal for binding to T-iRBC (Figure 3.6). Typically, positivity would only be assigned if the absorbance values of the target are at least 2-fold higher than that of the background [235]. Although clone 94 and 96 presented more than 6 absorbance units above their respective background, the absolute signal overall for all clones (absorbances of the RBCs subtracted from those of T-iRBCs) was less than 0.4, similar to the vehicle controls (Figure 3.6). Therefore, the results obtained for screening of the scFvs with OPD as detection system with the HRP-conjugated anti-c-myc antibody was deemed unsuitable due to its low sensitivity, specificity, and high background.

Subsequently, a different antibody conjugate for the monoclonal scFv ELISA was considered where an AP-conjugated goat anti-mouse (IgG) H&L secondary antibody (ab97020) was used as an alternative to detect the ant-c-myc antibody-scFv complexes (Figure 3.7). A commonly used chromogen for AP, pNPP, was used as detection system.

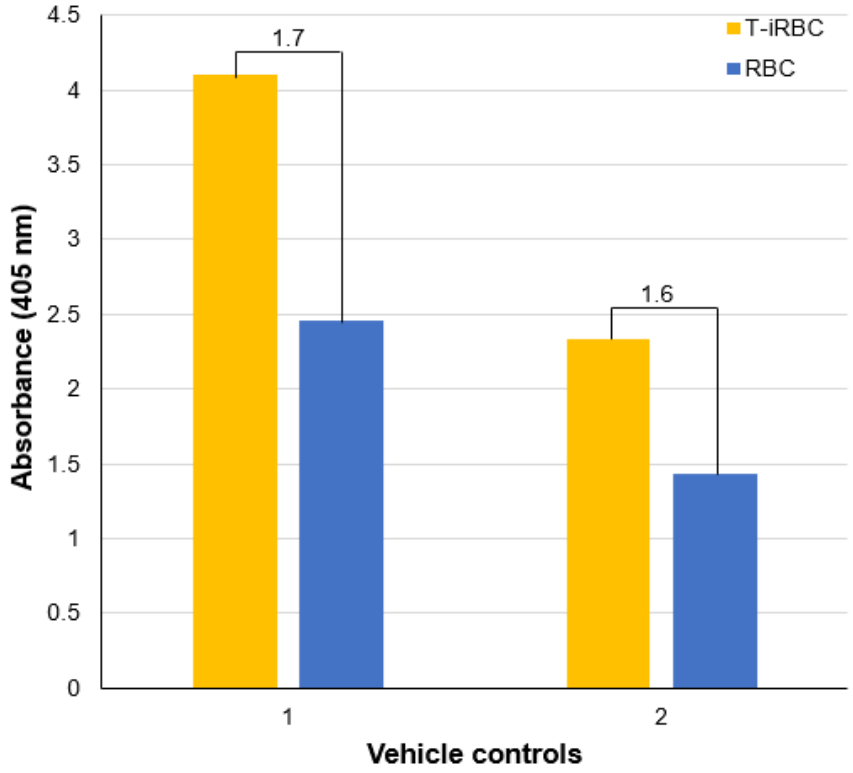

Figure 3.7. Evaluating monoclonal ELISA using sequential anti-c-myc antibody / goat anti-mouse H&L-antibody-AP signaling for screening of scFv clones. In the absence of scFvs**,** unconjugated anti-c-myc antibody was incubated with uninfected red blood cells (RBCs) and late trophozoite- and schizont-stage infected red blood cells (T-iRBC), respectively. An AP-conjugated goat anti-mouse (H&L) secondary antibody was then used to detect anti-c-myc antibody-scFv complexes. PNPP was used as the substrate and the absorbance measured at 405 nm. The screening was performed in duplicate

The ratio of control *vs.* background was around 1.7, indicating that still a large contribution of background signal came from the uninfected RBC population that is now recognised by the AP-conjugated goat anti-mouse (H&L) secondary antibody (Figure 3.7). However, the background levels were more uniformly present with little variation in the signal-to-background ratio (1.7 *vs*. 1.6 in repeats). Additionally, the absorbance values obtained for the controls were much higher than that of the previous monoclonal ELISA (represented in Figure 3.5), which might indicate that this assay has an improved readout. The assay was therefore used to screen multiple single clone scFvs against T-iRBCs whilst simultaneously screening the same scFvs against uninfected RBCs to allow correction for background interference (Figure 3.8).

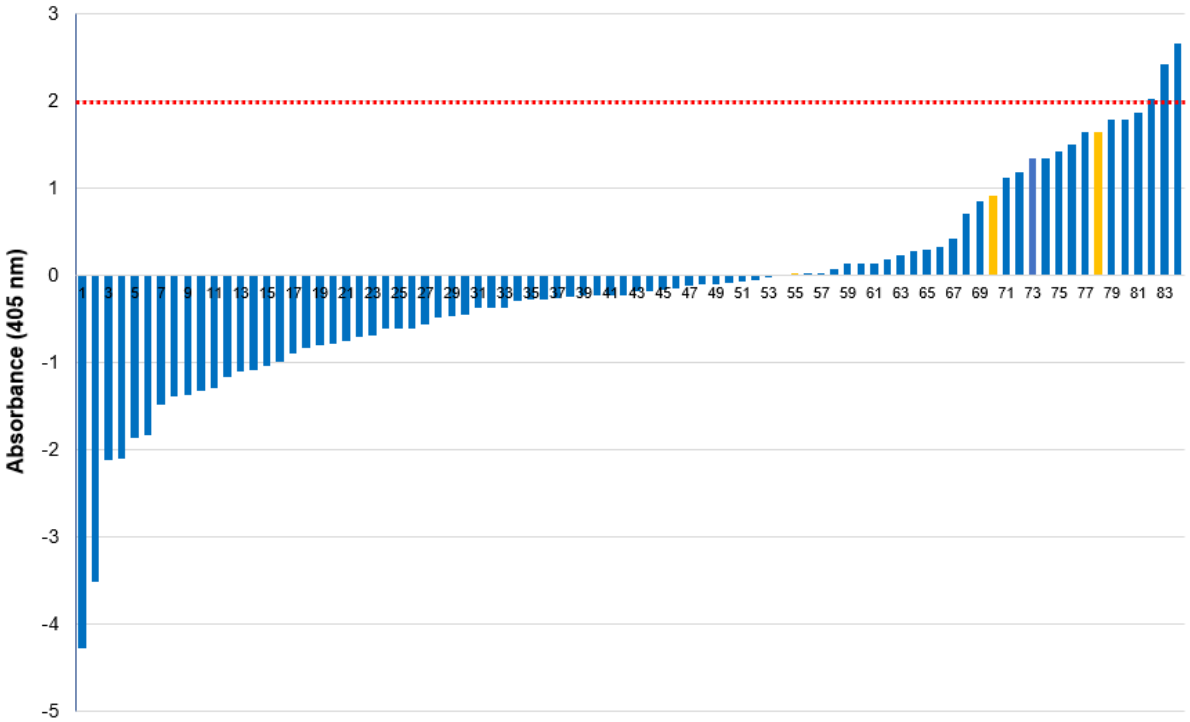

Figure 3.8. Screening of single scFv clones against *P. falciparum*-infected RBCs with monoclonal ELISA. Single clones (1-84) were screened with uninfected red blood cells (RBCs) (control) and late trophozoite- and schizont-stage infected red blood cells (T-iRBC), respectively. The control samples that contained no scFvs are represented by 70 and 78 (yellow bars). An AP-conjugated goat anti-mouse (H&L) secondary antibody was used to detect anti-c-myc antibody-scFv complexes. PNPP was used as the substrate and the absorbance measured at 405 nm. The results are expressed as the absorbance values of the control RBCs subtracted from those of the T-iRBCs.

Even though a low signal to background ratio (RBCs to T-iRBCs) were still observed throughout, this screening strategy resulted in ~36% of the clones screened exhibiting a positive signal for binding to T-iRBCs (Figure 3.8). Three of these clones (clone 81, clone 82 and clone 83) exhibited at least a 2-fold signal difference between T-iRBC and RBC, which could potentially indicate them as positive clones (Figure 3.8).

After carefully repeating the above-mentioned ELISA strategies to test the same scFv clones (i.e., repeating the assays by screening the same clones as above), persistent inconclusive findings were revealed that indicated the lack of repeatability and reproducibility of these assays. For instance, although initially the control plate (uninfected RBCs) contained the same number of cells as the plate with T-iRBCs and all the washing steps were carefully performed, it was evident that after each washing step cells were lost. This indicated that the cell immobilisation strategy was inadequate and/or the several washing steps were detrimental (especially on the T-iRBC plate). A colour difference between the plates coated with RBC (pinkish colour) and the plate

coated with T-iRBC (orange-brown colour) was prominent. The background absorbances of the uninfected RBCs remained present. The need for optimization of certain parameters (e.g., cell immobilization strategy, binding and washing conditions and detection mechanism) or a development of a different strategy was therefore required. Another custom way for screening on whole cells, is by performing the whole process on cells in suspension. This screening method was evaluated where the whole experiment was done in solution (as described in section 3.2.5.2).

3.3.2.2 Monoclonal scFv binding to dispensed T-iRBCs

To eliminate inefficient trapping of RBCs and to reduce cell loss during washing steps, a different strategy, where scFvs were screened to bind to suspended T-iRBCs (described in section 3.2.5.2), was evaluated to determine the monoclonal scFvs binding potential to T-iRBCs. To eliminate possible reagents that could cause a high background, the best suited chromogen was firstly determined. OPD and pNPP were added directly to RBCs and T-iRBCs (in the absence of HRP-anti-c-myc antibody and AP-conjugated goat anti-mouse (H&L) secondary antibody, respectively) to determine whether these substrates would cause any significant background (Figure 3.9).

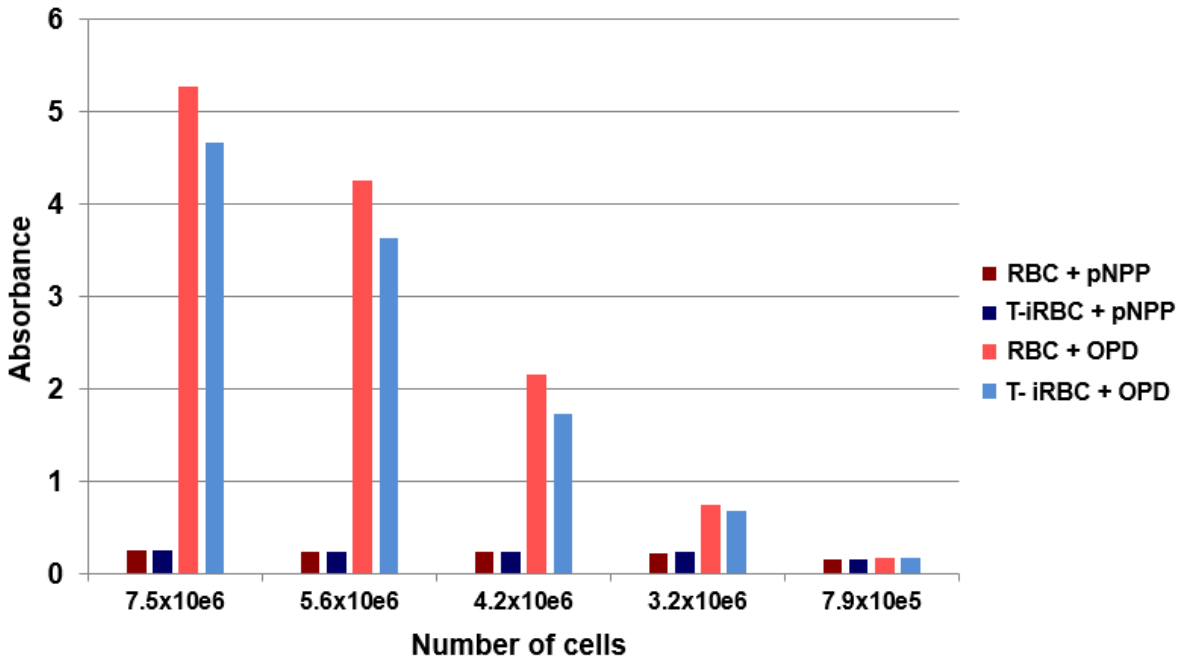

Figure 3.9. Testing the effect of different substrates (OPD or pNNP) to use in the presence of RBCs and T-iRBCs. The results are expressed as absorbance at 405 nm (for pNPP) and 492 nm (for OPD), respectively. The number of cells is shown on the x-axis. Red blood cell (RBC); late trophozoite and schizont-stage-infected red blood cells (T-iRBCs); para-nitrophenylphosphate (pNPP); o-phenylenediamine dihydrochloride (OPD).

PNPP was identified as the substrate with the least background as defined by A_{405} <0.3 for both RBCs and T-iRBCs (Figure 3.9). Even though a high number of cells (1-5 x 10^7) is usually preferred for screening antibodies on live cells, it could still influence the background signal in screening assays and therefore the effect of quantity of cells was evaluated. In the case where OPD (in the absence of HRP) was used as substrate, a high background signal was observed with an increase cell number (for both T-iRBCs and uninfected RBCs) (Figure 3.9). The number of cells had no effect on the background signal in the presence of pNPP (Figure 3.9), therefore pNPP was identified as the most promising substrate.

The potential of the assay where scFvs are screened on suspended T-iRBCs (described in section 3.2.5.2), was evaluated by screening seven single scFv clones using pNPP as chromogen to detect AP-conjugated goat anti-mouse (H&L) secondary antibody that bound to anti-c-myc antibody-scFv complexes (Figure 3.10).

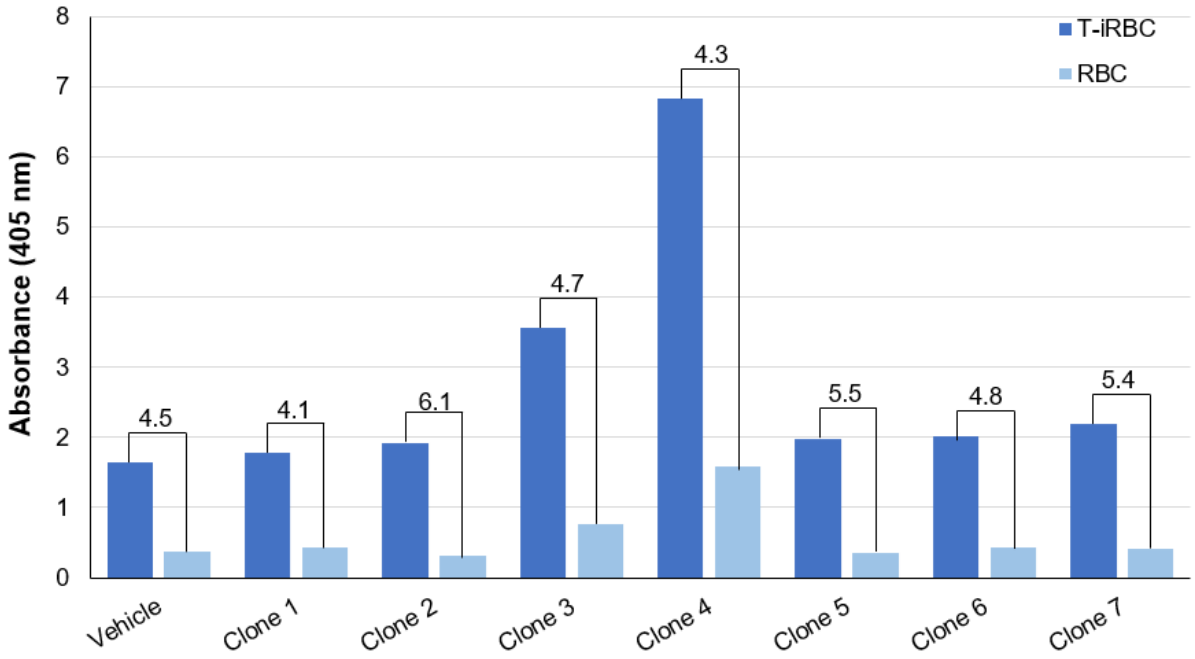

Figure 3.10. Screening of single clone scFvs against *P. falciparum*-iRBCs in suspension. Single clones (Clone 1-7) and a control sample (vehicle, containing no scFvs) were screened for binding to *P. falciparum*- late trophozoite and schizont-stage infected red blood cells (T-iRBCs) and uninfected red blood cells (RBC) (control for background interference), respectively. An AP-conjugated goat anti-mouse (H&L) secondary antibody (ab97020) was used to detect anti-c-myc antibody-scFv complexes. PNPP was used as the substrate and the absorbance measured at 405 nm. The results are expressed as the absorbance values of the RBCs and those of T-iRBCs, respectively.

The high signal-to-background ratio (RBCs to T-iRBCs) resulted all the clones presenting with a positive signal for binding to T-iRBC, especially clone 5 and clone 7 with an absorbance at least 5-fold signal difference between the T-iRBC and RBC (Figure 3.10). However, a similar positive signal was obtained for the vehicle sample (containing no scFvs).

Therefore, an additional step was introduced in the following screening where the same single clones were first pre-adsorbed to uninfected RBCs before testing their binding to T-iRBCs in solution (Figure 3.11).

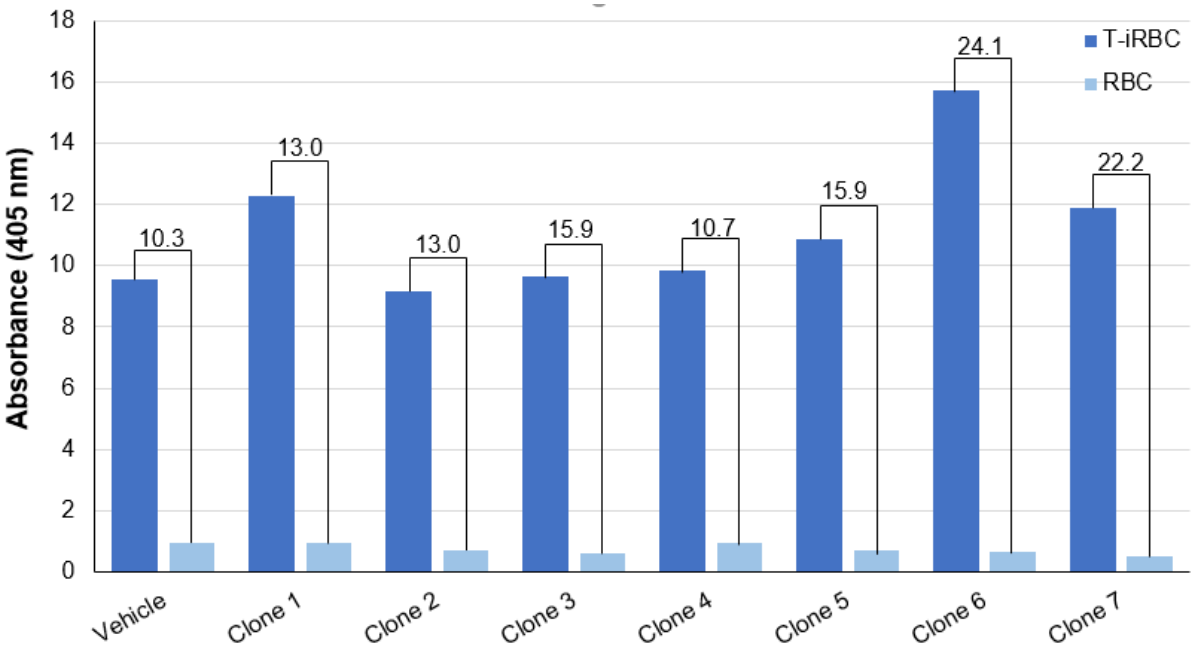

Figure 3.11. Screening of single clone scFvs against *P. falciparum*-iRBCs in suspension. Single clones (clone 1-7) and a control sample (vehicle, containing no scFvs) were firstly pre-adsorbed with uninfected red blood cells (RBC) before being screened for binding to *P. falciparum*- late trophozoite and schizont-stage-infected red blood cells (T-iRBCs) and RBCs (control for background interference), respectively. An AP-conjugated goat anti-mouse (H&L) secondary antibody (ab97020) was used to detect anti-c-myc antibody-scFv complexes. PNPP was used as the substrate and the absorbance measured at 405 nm. The results are expressed as the absorbance values of the control RBCs and those of T-iRBCs, respectively.

Pre-adsorption led to an extensive increase in signal of all the scFv clones (including the vehicle sample where scFvs were absent) (Figure 3.11). This could indicate that there was high background of reagents in the presence of T-iRBCs or one of the used antibodies (anti-c-myc antibody or the AP-conjugated goat anti-mouse (H&L) secondary antibody) bound non-specifically to T-iRBCs.

3.3.3 Confocal microscopy

To ascertain whether the positively identified scFvs clones (Figure 3.11) indeed recognised T-iRBCs *in vitro* or whether the anti-c-myc antibody bound non-specifically to T-iRBCs, confocal fluorescent microscopy was employed (Figure 3.12).

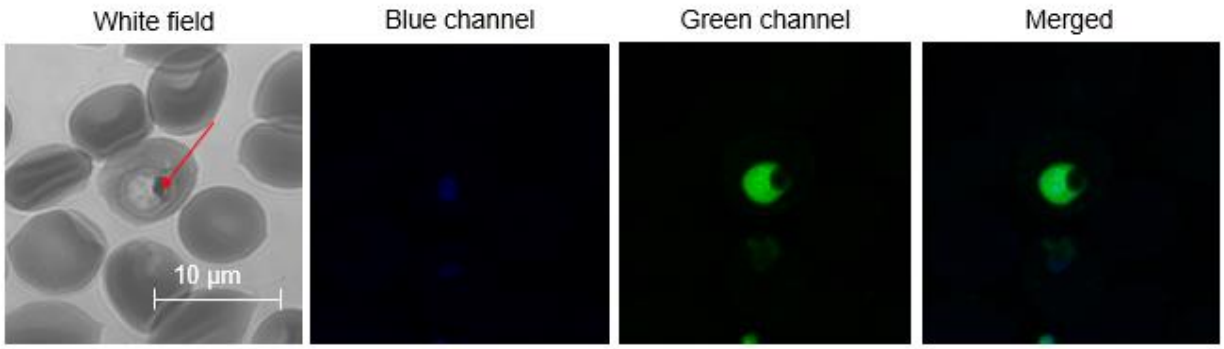

Figure 3.12. Evaluating if confocal microscopy could be used to identify single scFv clones that bind to T-iRBCs. Hoechst (seen through blue channel) was used to stain the parasite DNA. The FITC-conjugated anti-c-myc antibody (clone 9E10) (seen through green channel) bound to T-iRBCs in the absence of scFvs. The channels were merged to overlap and detect the two stains together. The white field was used to detect the haemozoin crystal (indicated by a red arrow) to distinguish T-iRBCs (containing a haemozoin crystal) from uninfected RBCs. Images were acquired with a Zeiss Axiocam 506 mono camera controlled with Zeiss ZEN 3.2 blue edition software (Carl Zeiss GmbH, Jena, Germany). ImageJ version 1.52v open-source software (National Institutes of Health, Bethesda, MA, USA) was used for further editing images (blue channel image displayed value = 0-129; green channel image displayed value = 0-225) and merging of channels.

T-iRBCs could be discriminated from uninfected RBCs by the presence of haemozoin crystals (as seen in the white field) and Hoechst nuclei stain (seen through the blue channel) corresponding to the T-iRBC. In trophozoites, haem detoxification occurs forming haemozoin crystals identifiable in the food vacuole [62]. When no scFvs were present, the FITC-conjugated anti-c-myc antibody (clone 9E10) bound to T-iRBCs (seen through green channel) but did not bind to uninfected RBCs (identified in white field as cells that lack a haemozoin crystal and confirmed through the blue channel that these cells did not contain parasite DNA) (Figure 3.12). This could serve as the explanation why all scFv clones tested positive for binding to T-iRBCs in the monoclonal scFv screening to T-iRBCs in suspension (Figure 3.10 and Figure 3.11). Consequently, confocal microscopy failed to evaluate whether any of the positively identified scFv clones actually did bind specifically to T-iRBCs.

3.4 Discussion

Single-chain variable fragments, compared to full size mAbs, have become powerful vectors in the clinical setting due to favourable pharmacokinetic properties and relative ease of production [162]. In this study, the *Nkuku*® - and *Inshi*® libraries were screened for scFvs specific to T-iRBCs through phage display technology. If scFvs can successfully be identified, these *P. falciparum*-specific scFvs could in turn then be assessed for the ability to use them as radiolabelled tracers to track malaria infections *in vivo* via PET imaging.

There are several different screening methods that have been developed over the years. The most commonly used method involves immobilising target antigens on a solid support such as magnetic beads, nitrocellulose column matrices or plastic surfaces and then incubating the scFvs with these antigens for affinity capture [236]. This method allows easy and fast wash steps to remove the unbound antibodies however, this conventional screening system could not be simply applied in our case where the whole live cell represents the target [237]. The parasite expresses complex antigens on the T-iRBC surface, with each life cycle presenting antigenic variation [83]. Selection of phage-displayed antibodies where the target is represented by the whole cell, is typically performed through biopanning in cell suspension or on a solid support where cells are either fixed or immobilised to a solid surface [238]. Even though whole cell biopanning has many difficulties, in this study, biopanning was performed either with T-iRBCs in suspension and/or T-iRBCs immobilised on a solid support.

MTP-based ELISAs was firstly evaluated for screening a large amount of single soluble scFvs on immobilised T-iRBC. In any biochemical screening process, there are certain parameters that can compromise an optimal selection output, e.g., the target cell and immobilisation strategy, the quality of the antibody library, the binding conditions, the washing conditions and/or the detection mechanism. Even though HRP is widely used in screening cell assays, in our case where HRP-conjugated anti-c-myc antibody was used to detect scFvs, the method proved to be insensitive [231, 235, 239, 240]. Additionally, during both these immobilised cell screening assays, cell loss was evident with every washing step (i.e., the immobilisation was inadequate). Therefore, screening was attempted on cells in suspension however, a high background of reagents in the presence of T-iRBCs was observed. We also saw

differences in background between substrates (pNPP *vs*. OPD) in the presence of RBCs. This points out the importance of testing different substrates before commencing to the screening processes in the presence of RBCs.

Confocal microscopy revealed a possible reason for the high PNPP signal observed in the presence of T-iRBCs in suspension (Figure 3.10 and Figure 3.11). The FITC-conjugated anti-c-myc antibody, used for detecting T-iRBC-scFv complexes, bound to T-iRBCs (in the absence of scFvs) while binding is absent on uninfected RBCs (Figure 3.12). This phenomenon could be due to the high permeability of T-iRBC which might allow the IgG antibody to enter the cell. It has been found that some macromolecules, including IgG, can be taken up by iRBCs [241].

This study proved that screening of scFvs on T-iRBC is complicated and the methods studied in this chapter were insufficient to identify scFvs binding to T-iRBCs. There are some other selection/screening techniques that have been explored using live target-expressing cells, such as fluorescence-activated cell sorting (FACS) and panning on adherent cell monolayers and magnetic based semi-automated screening [242]. Of these techniques, the recently discovered magnetic-based semi-automated screening allows high-throughput selection of antibodies by immobilizing cells to a microtiter plate however, this process has proven to be incredibly expensive [233, 243]. Additionally, one should always consider the fact that any extra steps that could cause extra stress on the parasite, would eventually lead to compromised/ dead cells that does not represent the true nature of T-iRBCs.

Phage display technology has provided imaging agents in pre-clinical settings, therefore, in the following chapter, a *P. falciparum*-specific peptide, which has been discovered by peptide phage display technology, was radiolabelled and evaluated for its potential to be used in future as an *in vivo* imaging agent.

Chapter 4

Radiolabelling and initial characterisation of the iRBC-reactive peptide P1 towards prospective preclinical nuclear imaging

The content of this chapter is invited for submission in Frontiers in Medicine: Research Topics - Functional Imaging of Inflammation and Infection.

4.1 Introduction

Currently, nuclear medicine protocols have implemented peptide-based radiopharmaceuticals for localisation and staging of different diseases [244]. The use of peptides as vectors in molecular imaging have become very attractive due to their favourable biodistribution *in vivo*. Their molecular weight of <5 kDa often realises superior target-to-non-target ratios due to fast clearance from blood and non-target tissues and high receptor affinity at the target. Additional advantages of peptides include their low antigenicity, rapid tissue penetration, low toxicity, toleration of harsher conditions for radiolabelling, and the structural capability to accept the conjugation with certain chelating agent without compromising the peptide's targeting properties [245-247].

Malaria-related drug discovery lead to the characterisation of multiple antimalarial peptides that exhibit a growth inhibitory effect on the parasite or cause haemolysis of iRBCs upon interaction [248-253]. Some of these peptides are suggested to target malaria-specific targets expressed only on iRBCs and could potentially be used for targeted molecular imaging or serve as a probe for selective delivery of drugs [254].

Eda *et al*. (2004) utilized extensive panning of a peptide phage display library (PDL) on T-iRBCs and positively identified 8 clones. They continued to characterise the most frequently obtained clone and revealed the synthetic 7-mer sequence LVDAAAL that binds selectively to the membrane of late asexual-iRBCs [221]. This peptide sequence was further cyclized by disulfide bonding by way of the supplemented cysteine residues at the flanking regions and expressed at the N-terminus of a coat protein of phage, called pIII. For further experimentation, this peptide was complemented with a

biotin moiety conjugated to the N-terminal of the peptide, which was named P1 (biotin-C*LVDAAALC*, cyclized at the asterisked cysteine residues). Although the sequence of P1 did not show homology to any proteins known to bind to the surface of iRBCs, it demonstrated binding to different *P. falciparum* strains, each with its own unique surface proteins (i.e., FCR-3 strain expresses knobs and has CD36-binding activity; the CS2 strain expresses knobs and bind preferentially to chondroitin sulphate; erythrocytes infected with D3 are knobless and bind to CD36). Therefore, the authors suggested that the target of P1 could be conserved in RBCs infected with different strains of *P. falciparum* [221].

P1 embodies structural and biological properties to allow its study in malaria pathology via optical and nuclear imaging. It therefore shows potential as a candidate for radiometal complexation to be used as a peptide-based pharmaceutical for nuclear-mediated imaging.

This chapter comprises of the evaluation of the antimalarial peptide P1. A modified P1 derivative (fluorescein isothiocyanate-Gly-conjugated P1 (FITC-P1)) was hereby used for confocal microscopy to justify its uncompromised targeting properties to T-iRBC. P1 was then further investigated towards its compatibility with ^{68}Ga-radiosynthesis using a 1,4,7,10-tetraazacyclododecane-1,4,7,10-tetraacetic acid (DOTA)-Gly-functionalized P1 (DOTA-P1) derivative. The resultant radiolabelled tracer ([^{68}Ga]Ga-DOTA-P1) was utilized to evaluate its stability in various chemical formulation and to study its behaviour in blood and serum. If required, the linear peptide FFSATLGNEE (C1), also suggested by Eda *et al*. (2004), was used as a control during the experiments (i.e., FITC-C1 or DOTA-C1). The outcome from these investigations will allow justification of future testing of P1 concerning its radiopharmaceutical or antimalarial drug development.

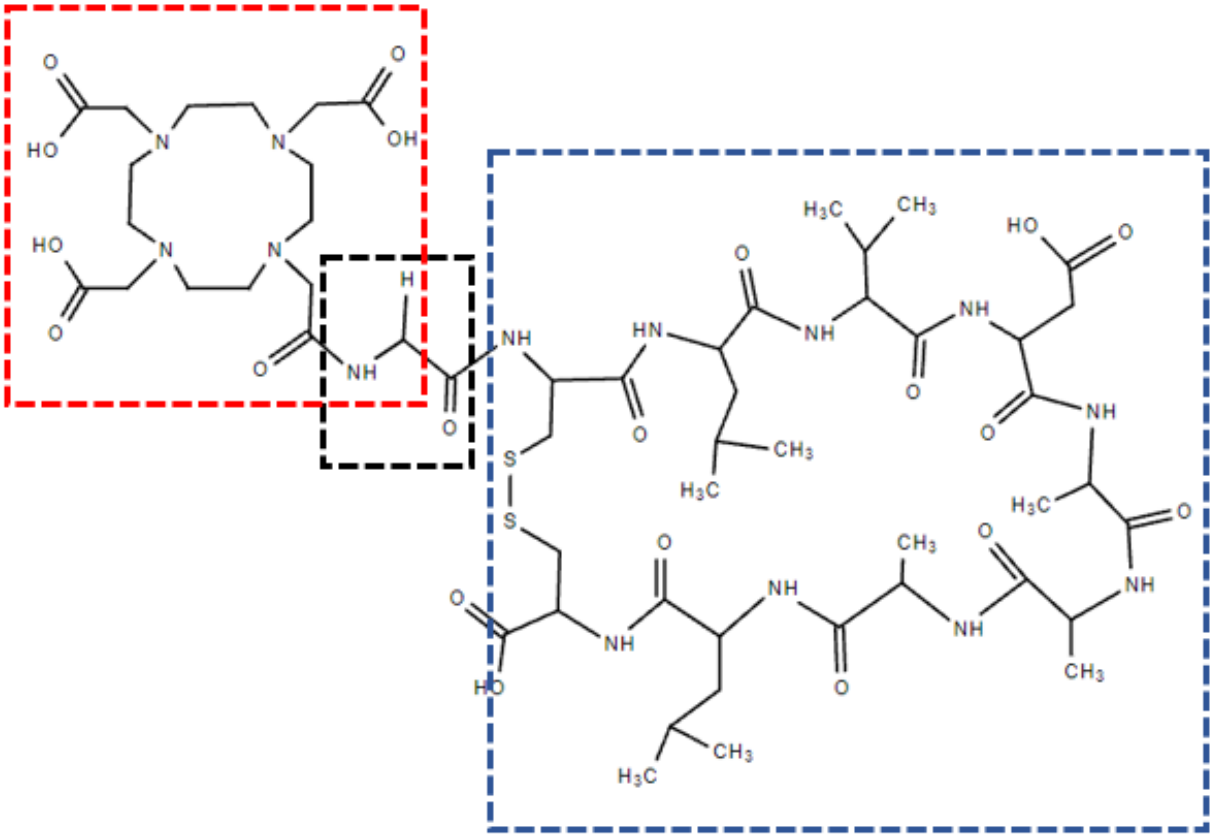

Figure 4.1. Chemical structure of DOTA-P1. The cyclic peptide P1 (NH2-CLVDAAALC-OH) (blue) is linked via glycine (black) with the bifunctional chelator molecule 1,4,7,10-tetraazacyclododecane-1,4,7,10-tetraacetic acid (DOTA) (red).

4.2 Methodology

P1 C*LVDAAALC*, cyclized at the asterisked cysteine residues

If required, the linear peptide FFSATLGNEE (C1) also suggested by Eda *et al*. (2004), was used as a control (i.e., FITC-C1 or DOTA-C1).

4.2.1 Confocal microscopy

Confocal microscopy was used to evaluate the binding of P1 (C*LVDAAALC*, cyclized at the asterisked cysteine residues) to *P. falciparum* T-iRBCs (FCR-3 strain) [182]. Either fluorescein isothiocyanate-Gly-conjugated-P1 (FITC-P1) or -C1 (both peptides supplied by GL Biochem, Shanghai, China) was dissolved in PBS to make a stock solution of 2.5 mg/mL. *P. falciparum* (strain FCR-3) was cultivated as described in section 3.2.1. *P. falciparum* cultures (5% haematocrit, 10-13% parasitaemia) containing a majority of T-iRBCs, were harvested and washed three times with PBS and treated with a blocking buffer (1% (w/v) BSA in PBS) for 30 min at room temperature. After the blocking buffer was removed by centrifugation (SL 8R centrifuge, Thermo Fisher Scientific, Waltham, Massachusetts, USA) at 3500 x*g* for 2 min, 500 µl of FITC-P1 or -C1 (1:100 dilution in PBS) was added to the pre-blocked T-iRBC culture and incubated for 1 h at 37°C whilst gentle shaking. Samples were washed three times with PBS to remove any unbound peptide. The cells were fixed on the coverslip as described in section 3.2.6. Parasite DNA was additionally stained with a 1:500 dilution of Hoechst 33342 (Invitrogen, Thermo Fisher Scientific, Johannesburg, South Africa) in PBS at room temperature for 30 min. The slides were subsequently evaluated with fluorescence confocal microscopy using a confocal laser scanning microscope 880 (Carl Zeiss GmbH) AG, Oberköchen, Germany) equipped with a Plan-Apochromat 100x/1.46 oil DIC M27 Elyra objective. The pinhole size was set to 1.68 AU. Images of 1040 x 1040 pixels were acquired using PMTs detectors. Hoechst signal was detected at 410-497 nm through the blue channel and FITC was detected 493-634 nm through the green channel. Images were acquired with a Zeiss Axiocam 506 mono camera controlled with Zeiss ZEN 3.2 blue edition software (Carl Zeiss GmbH, Jena, Germany). ImageJ version 1.52v open-source software (National Institutes of Health, Bethesda, MA, USA) was used for optimizing the image display (blue channel images displayed value = 20-126; green channel images displayed value = 6-120).

4.2.2 Radiolabelling

DOTA-P1 (GL Biochem, Shanghai, China) was dissolved in deionised water to a concentration of 1.25 mg/mL, aliquoted and stored at -80°C until further use. Inputs for the protocol for ^{68}Ga-labelling of DOTA-P1 have been adopted from a previously described procedure by Mokaleng *et al.* (2015) as well as Rossouw *et al*. (2012) [255, 256]. A SnO_2-based ^{68}Ge/^{68}Ga-generator (iThemba LABS, Somerset West, South Africa) was routinely eluted with 10 mL HCl (0.6 M). [^{68}Ga]$GaCl_3$ was yielded by eluate fractionation (Ebenhan *et al.* (2014)) and a 1 mL eluate fraction was directly buffered by 2.5 M sodium acetate to yield a desired labelling pH of 3.5-4.0 [257]. DOTA-P1 (30 µg) was added to 1 mL of the buffered ^{68}Ga-radioactivity and labelling was carried out at ~90°C for 10 min. The same procedure was followed for the radiolabelling of DOTA-C1 (30 µg). If required the radiolabelled peptide conjugates were purified by solid phase extraction using a SepPak C18 light cartridge (SPE-C18L, Waters Corporation, Milford, USA). The SPE-C18L matrix was equilibrated with 4 mL ethanol and 3 mL deionised water. The complete radiolabelling mixture was slowly loaded on the SPE-C18L followed by a rinsing step using 10 mL saline solution. To recover the product the SPE-C18L was treated with 1 mL ethanol/saline (1:1; v/v). The radiochemical yield (RCY (MBq)) and relative labelling efficiency (%LE) were calculated from the sum of the activities present in the reaction mixture, syringes, cartridge and purging liquids.

4.2.3 Instant thin-layer chromatography

The relative radiochemical purity (RCP (%)) was determined via gamma-ray detection using radio-iTLC. SG-iTLC paper strips (100 × 10 mm) were used as stationary phase. A small amount of radioactivity was drawn from the relevant samples (~2 µL) and spotted at the bottom (~10 mm up) of the strip. The SG-iTLC paper was placed in glass tubes pre-equilibrated with 1-2 mL of either mobile phase A) 0.1 M sodium citrate (pH 5.0) or B) 1 M ammonium acetate/methanol 1:1 (v/v) and exposed until the solvent front migrated close to the top of the strip (incubation time about 7-8 min). The strips were dried and subjected to gamma ray detection on a TLC scanner (MiniGITA-single, Elysia-Raytest GmbH, Straubenhardt, Germany) yielding chromatograms that were further analysed with Gina X Software (Elysia-Raytest GmbH, Straubenhardt, Germany) allowing to use of “area under the curve” calculation of the percentage of the peak. Retention factors (R*f*) were calculated as the decimal between the distances travelled (mm) by the solvent front and the component of interest.

4.2.4 ^{68}Ga-complexation constancy

To attest for accurate complexation of gallium-68 to the DOTA-P1 and DOTA-C1, radio-iTLC analysis (SG-iTLC / 0.1 M sodium citrate (pH 5.0)) was used. Radiolabelled product samples were exposed to challenging product conditions or formulations were analysed immediately as well as after a 30 min, 60 min or 120 min incubation period. The radio-iTLC chromatograms of each time point were analysed for reoccurring radioactivity that attributes to free ^{68}Ga-species close to the solvent front.

4.2.5 Blood cell binding and serum analysis

Prior to blood cell binding and serum analysis preparations of [^{68}Ga]Ga-DOTA-P1 included SPE-C18L purification, ethanol evaporation and pH adjustment with 0.1 M PBS (pH 7.4). Product RCP was ascertained using radio-iTLC analysis. The PCIF provided whole blood in heparin-coated vacutainers (Transpharm, Pretoria, South Africa). [^{68}Ga]Ga-DOTA-P1 (180 µL; ~1.2 µg; 1.5 - 1.8 MBq) was added to the 720 µL whole blood aliquots and incubated for 30 min and 60 min at room temperature. Each time 300 µL samples were withdrawn and transferred to BD vacutainer SST II advanced tubes (Transpharm, Pretoria, South Africa) to allow the serum to be separated from the blood cells by centrifugation (EBA20, Hettich Zentrifugen, Tuttlingen, Germany) at 4500 rpm for 5 min. An automated gamma radiation counter (Hidex Gamma Counter AMG, Turku, Finland) was used to determine the total radioactivity amount of [^{68}Ga]Ga-DOTA-P1 represented within the serum- and blood cell fraction. Samples were corrected for decay and weight differences between replicates per time point. The RBC bound fraction was calculated by obtaining the percentage of RBC radioactivity in the combined fractions.

Additionally, serum analysis was performed; [^{68}Ga]Ga-DOTA-P1 (200 µL; ~1.3 µg; 1.4 - 1.7 MBq) was incubated with 1000 µl serum at room temperature. Samples (100 µl) were drawn after 30 min and 60 min incubation and the proteins were precipitated with 500 µl ice-cold acetonitrile followed by centrifugation (EBA20, Hettich Zentrifugen, Tuttlingen Germany) for 5 min at 6000 rpm. The supernatant was transferred to a new tube and the precipitated proteins were washed with 100 µl ice-cold acetonitrile. The supernatants were combined and analysed by radio-iTLC. The percentage [^{68}Ga]Ga-DOTA-P1 bound to serum proteins was calculated using the radioactivity measurements of the protein pellet and the supernatant from each sample were

determined gamma radiation counting (Hidex Gamma Counter AMG, Turku, Finland). Samples were corrected for decay and between replicates per time point. The protein binding is expressed as a percentage of the total activity measured.

4.3 Results

4.3.1 Confocal microscopy

Since the sizes of FITC and DOTA are similar and both were conjugated to the N-terminus of P1, it was deemed sufficient to use FITC-P1 in confocal microscopy to validate binding of a modified P1 (in later stages being [^{68}Ga]Ga-DOTA-P1) to FCR-3-iRBCs. As it is known that the membrane of iRBCs is permeable to small molecules, non-specific FITC-conjugated peptide (FITC-C1) was used as a control to validate that the binding of P1 to the iRBC was specific (Figure 4.2).

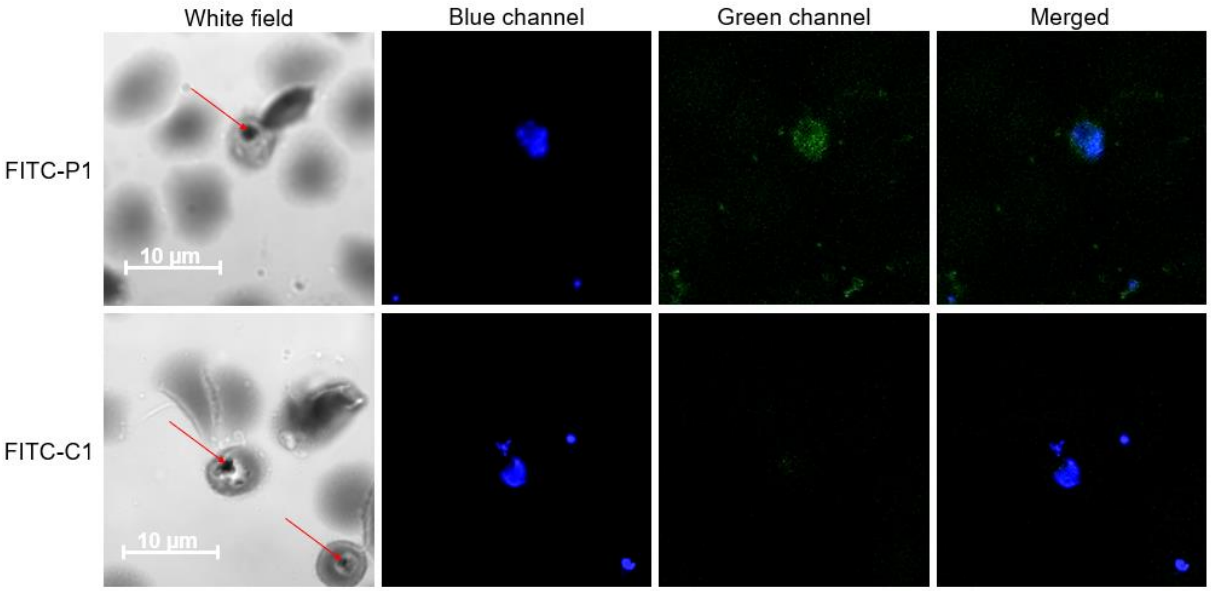

Figure 4.2. Confocal microscopic evaluation of FITC-P1 and FITC-C1 binding to FCR-3-iRBC. Parasite nuclei were stained with Hoechst and visualized through the blue channel. The FITC-conjugated P1 (FITC-P1), visualized through green channel, bound to T-iRBCs. However, the FITC-conjugated C1 (FITC-C1) did not bind to T-iRBCs. The channels were merged for overlayed display and co-localization. The white field was used to confirm the haemozoin crystal (indicated by the red arrows) to distinguish T-iRBCs (containing a haemozoin crystal) from uninfected RBCs. Images were acquired with a Zeiss Axiocam 506 mono camera controlled with Zeiss ZEN 3.2 blue edition software (Carl Zeiss GmbH, Jena, Germany). ImageJ version 1.52v open-source software (National Institutes of Health, Bethesda, MA, USA) was used for optimizing the image display (blue channel images displayed value = 20-126; green channel images displayed value = 6-120) and merging of channels.

FITC-P1 binding was specific to T-iRBCs, with no binding to uninfected RBCs. The absence of binding of FITC-C1 to T-iRBCs further supported the finding that FITC-P1's binding to T-iRBCs was specific.

4.3.2 Radiolabelling

The adopted radiolabelling method achieved effective radiolabelling (RCY >99%) of both DOTA-P1 and DOTA-C1 (Figure 4.3) within 10-15 min incubation.

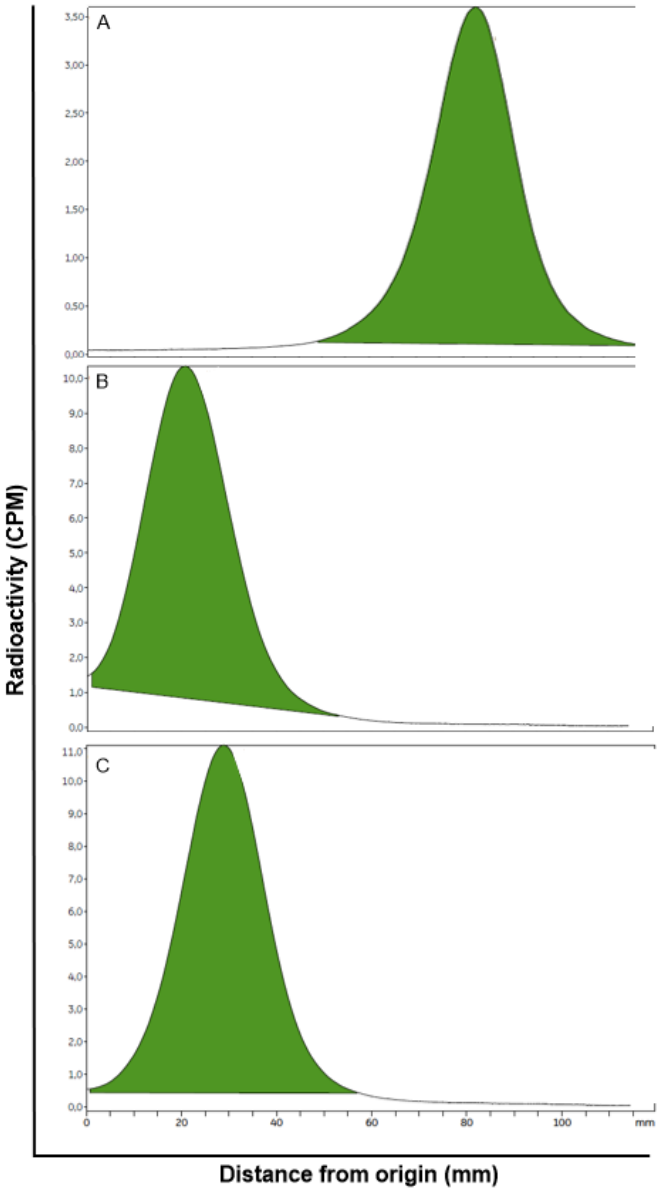

Figure 4.3. Radio-iTLC resolution analysis. SG-iTLC strips were spotted with 1 µl of sample (origin = 10 mm) and allowed to develop for 8 min in 0.1 M sodium citrate; pH 5.0 (solvent front = 100 mm). The strips were dried and subjected to gamma detection on a MiniGITA single thin-layer chromatography scanner yielding in chromatograms for radio-peak identification and quality of compound separation (resolution). Radio-peak integration utilized Gina X Software and "area under the curve" quantification (counts per minute) was performed to calculate the percentage radiochemical purity. Representative samples for A) 100% free, ionic [^{68}Ga]-activity and B) 100% [^{68}Ga]Ga-DOTA-P1 and C) [^{68}Ga]Ga-DOTA-C1 are displayed.

The iTLC method sufficiently separated free [^{68}Ga]$GaCl_3$ species migrating with the solvent front (R*f* = 0.85-0.95) while the radioactivity detected for [^{68}Ga]Ga-DOTA-P1

/C1 remained close to the origin (R*f* = 0.10-0.15) and could be used for calculation of %RCP (Figure 4.3). For both DOTA-peptides the results of multiple manual radiolabelling runs are summarised in Table 4.1.

Table 4.1 Summary of ^{68}Ga-radiolabelling results

Parameter	Criteria[#]	[^{68}Ga]Ga-DOTA-P1	[^{68}Ga]Ga-DOTA-C1
Eluted generator activity (MBq)		633 ± 72	678 ± 78
Germanium-68 (%)	0.001	0.00031 ± 0.00016	0.00037 ± 0.00011
Added activity / labelling (MBq)	>200	282 ± 39	308 ± 27
DOTA-peptide (nmol/mL)		22.7	20.0
Radiolabelling pH	3.0-5.0	3.7 ± 0.2	3.7 ± 0.3
Free ^{68}Ga-species(%)*	<5.0	3.2 ± 0.8	1.0 ± 0.3
^{68}Ga-Losses (%)**		7.7 ± 1.0	9.6 ± 2.4
^{68}Ga-Labelling efficiency (%)***		88 ± 11	85 ± 9
Preparation time (min)		32 ± 6	34 ± 3
RCP (%)	>95	99.8 ± 0.2	98.9 ± 0.6
RCY – EOR (MBq)		152 ± 13	144 ± 14
Molar activity (GBq/µmol)	>1.0	6.7 ± 0.5	9.1 ± 0.7

Footnotes: if not stated otherwise, results are expressed as mean ± SEM (n=4); RCY) radiochemical yield; EOR) end of radiosynthesis; RCP) radiochemical purity determined by radio-ITLC analysis. Results were calculated from radioactivity *) SG-iTLC peak quantification; **) losses considered as residual radioactivity adhered to empty syringes and material, the empty vial used for radiolabelling and non-revocable SPE-C18L activity; ***) decay-corrected value against all activity measurements, i.e., product activity relative to the sum of activity recovered after the SPE-C18L process: all liquid fractions, residual activity in empty syringes, the SPE-C18L material and in the empty vial used for radiolabelling. #) Criteria are followed according to European Pharmacopoeia 8.8-10.

Following eluate fractionation, the elutable activity yielded in 2 mL ranged from 82-90% of the total generator activity per elution in 10 ml HCl. This ^{68}Ga-activity (561-705 MBq / 600-756 MBq) was adequate to be used further for labelling (Table 4.1). Of this, a volume of 1 mL ^{68}Ga-activity was of sufficient quality (low ^{68}Ge-breakthrough ≤ 0.0006) and activity concentration (240-320 MBq/mL and 280-335 MBq/mL) to be utilized straightforward for the radiolabelling of either DOTA-P1 or DOTA-C1, respectively. Radiolabelling did not demonstrate any significant differences between [^{68}Ga]Ga-DOTA-P1 and [^{68}Ga]Ga-DOTA-C1 with a RCP exceeding 97% for both. Within about 30 min, efficient preparations (incl. purification) of [^{68}Ga]Ga-DOTA-P1 (LE = 77-99%) and [^{68}Ga]Ga-DOTA-C1 (LE = 76-94%) at a concentration of 22.7

nmol/mL and 20.0 nmol/mL was achieved, respectively. Average losses of radioactivity to material used in the radiosynthesis was favourably low (<10%), which resulted in acceptable molar activities (>1.0 GBq/µmol) for preclinical application.

4.3.3 ^{68}Ga-complexation constancy

The constancy ^{68}Ga regarding the complexation within [^{68}Ga]Ga-DOTA-P1 and [^{68}Ga]Ga-DOTA-C1 was tested by way of analysing reoccurring ^{68}Ga-species (i.e.; determining changes to the %RCP) following prolonged incubation of: 1) crude [^{68}Ga]Ga-DOTA-P1 /C1 (kept at pH 4.0), 2) crude [^{68}Ga]Ga-DOTA-P1 /C1 (pH 7.0-7.5; adjusted with 2 M NaOH), 3) crude [^{68}Ga]Ga-DOTA-P1 (pH 6.5; diluted 1:4 with PBS (pH 7.4)), and 4) SPE-C18L-purified [^{68}Ga]Ga-DOTA-P1 (pH 5.5). Samples were kept either at 4°C, room temperature (RT), or 37°C for up to 120 min. The summary of the results is provided in Table 4.2.

Table 4.2. Summary of results on radiometal complexation constancy

		RCP (%)							
Test	**Temp**	**[^{68}Ga]Ga-DOTA-P1** Incubation time (min)				**[^{68}Ga]Ga-DOTA-C1** Incubation time (min)			
		0	30	60	120	0	30	60	120
1	4°C	→	→	→	→	→	→	→	→
1	RT	→	→	→	→	→	→	→	→
1	37°C	→	→	→	→	→	→	→	→
2	4°C	→	→	→	→	→	↘	→	→
2	RT	→	→	→	→	→	↘	→	→
2	37°C	→	↘	→	→	→	↘	→	→
3	4°C	→	→	→	→	-	-	-	-
3	RT	→	→	→	→	-	-	-	-
3	37°C	→	→	→	→	-	-	-	-
4	37°C	→	→	→	→	-	-	-	-

Footnotes: 1) crude [^{68}Ga]Ga-DOTA-P1 /-C1 (kept at pH 4.0); 2) crude [^{68}Ga]Ga-DOTA-P1 /-C1 (pH 7.0-7.5; adjusted with 2 M NaOH); 3) crude) [^{68}Ga]Ga-DOTA-P1 /C1 (pH 6.5; diluted 1:4 with PBS (pH 7.4)), and 4) SPEC18L-purified [^{68}Ga]Ga-DOTA-P1 (pH 5.5). RCP) Radiochemical purity calculated from iTLC analysis (SG-iTLC / 0.1 M sodium citrate pH 5.0); Temp) temperature during incubation period; RT) incubation at room temperature; →) measured RCP remained constant ≥ 95%; ↘) RCP <95% and significantly decreased compared to previous value. -) values not determined.

The first test formulations of crude [^{68}Ga]Ga-DOTA-P1 and [^{68}Ga]Ga-DOTA-C1 remained stable at all tested temperatures up to the maximum incubation period (Table 4.2; 1). At test 2 formulation, following adjustments to neutral pH, [^{68}Ga]Ga-DOTA-P1 remained stable at either RT or 4°C over 120 min (RCP >99%), however, at 37°C, the RCP decreased after 30 min (RCP >60%) but remained constant thereafter (Table 4.2; 2). Conversely, crude [^{68}Ga]Ga-DOTA-C1 was unstable at any of the temperatures with the RCP decreasing to <40% at 37°C (Table 4.2; 2). Because of its compromised complexation constancy occurring for test formulation 2 at 37°C, [^{68}Ga]Ga-DOTA-P1 was re-assessed in a neutralizing PBS solution (Table 4.2; 3) which demonstrated a RCP >95% for all temperatures and incubation periods (Table 4.2; 3). Specifically, prior to assessing the [^{68}Ga]Ga-DOTA-P1's *in vitro* binding characteristics to RBCs and serum proteins it is essential to remove all the salt content from the crude product. Therefore, only [^{68}Ga]Ga-DOTA-P1 was SPEC18L-purified, the ethanol contents evaporated (product solution was challenged at pH 5.5, containing <5% ethanol) before assessing its stability at 37°C over 120 min (Table 4.2; 4). No significant re-occurrence of free ^{68}Ga-species (<5%) was calculated.

4.3.4 Blood cell binding and serum analysis

In context of malaria pathology, blood cell binding is a precondition to confirm the degree of interaction for [^{68}Ga]Ga-DOTA-P1 with uninfected erythrocytes (RBCs). [^{68}Ga]Ga-DOTA-P1 treatment of whole blood and subsequent fractionation allowed determining the radioactivity associated with serum *vs.* RBC as displayed in Figure 4.4.

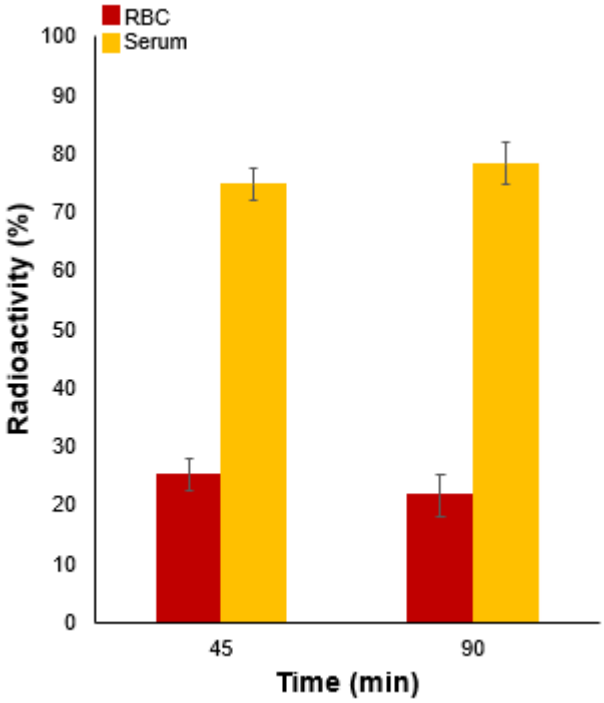

Figure 4.4. Erythrocyte binding of [^{68}Ga]Ga-DOTA-P1. [^{68}Ga]Ga-DOTA-P1 was incubated with whole blood samples at room temperature. Samples (n=3) were taken after 45 min and 90 min of incubation. The radioactivity measured in both fractions was decay corrected for the replicates and between time points. The red blood cell (RBC) and serum fraction is expressed as a percentage of the total activity measured (%) ± SD.

After 45 min of incubation 25 ± 3% and 75 ± 3% [^{68}Ga]Ga-DOTA-P1 activity was recovered in the RBC fraction and the serum fraction, respectively. The percentage [^{68}Ga]Ga-DOTA-P1 remained constant over 90 min (P=0.09; n=3) (Figure 4.4).

To better understand the binding properties of [^{68}Ga]Ga-DOTA-P1, the percentage of bound compound to serum proteins was determined at different time points (Figure 4.5). [^{68}Ga]Ga-DOTA-P1 radioactivity was found to 88 ± 3% bound to serum proteins whereas 12.1 ± 3% remained in the serum supernatant fraction (after only 30 min of incubation). There was no significant increase in protein binding from 30 min to 60 min incubation (P=0.10; n=3).

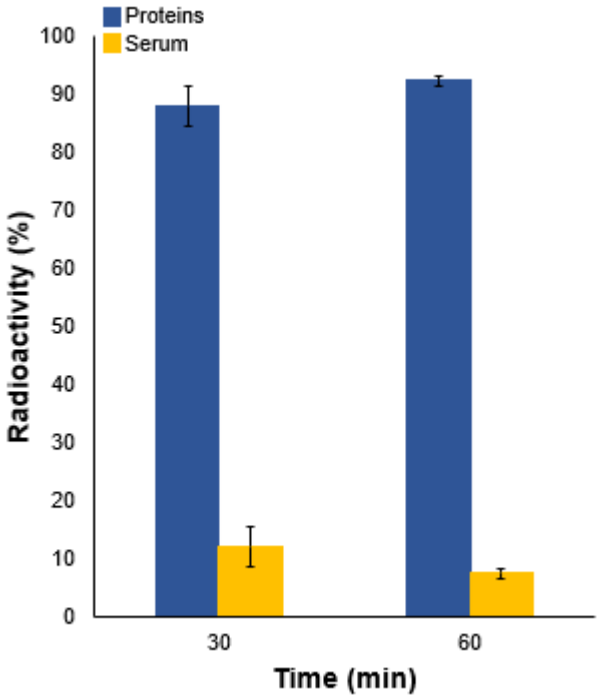

Figure 4.5. Protein binding of [^{68}Ga]Ga-DOTA-P1. [^{68}Ga]Ga-DOTA-P1 was incubated with serum at room temperature. Samples (n=3) were taken after 30 min and 60 min and the serum proteins were precipitated. The protein binding is expressed as a percentage of the total activity measured (%) ± SD.

The fraction containing the unbound [^{68}Ga]Ga-DOTA-P1 (e.g., the protein-free serum supernatant) was further analysed by radio-iTLC to assess the potential *in vivo* stability of [^{68}Ga]Ga-DOTA-P1. After 60 min incubation, the compound maintained a RCP >99% indicating that the compound had no metabolic decay in this time.

4.4 Discussion

Radiolabelled peptides serve as powerful tools for diagnostic imaging and radiotherapy of cancer and various infectious diseases [258]. Peptides have been successfully labelled with various radionuclides of which ^{68}Ga has become a particular popular PET radiometal isotope. Commercially available benchtop ^{68}Germanium/^{68}Gallium-generators have allowed research facilities and hospitals access to daily in-house ^{68}Ga supply to align it with efficient PET imaging [259]. Additionally, the short half-life of ^{68}Ga ($t_{1/2}$ = 68 min) allows for a reduced radiation exposure and permits repeated imaging. This radioactive half-life of also corresponds to the biological half-life of most peptides [260, 261].

As P1 is a relatively small peptide (~1 kDa), even a small structural change within the peptide could influence its targeting properties. Therefore, before commencing with radiolabelling, confocal microscopy was carried out to evaluate whether a FITC-modified P1 would maintain its binding capability to T-iRBC (herein the FCR-3 strain was used). The concept for this study hinges on the assumption that DOTA and FITC have a similar molecular weight and structure and either modification could potentially affect the binding capacity of P1. The results indicated that FITC-P1 bound specifically to FCR-3 T-iRBCs; however, the linear non-specific peptide (control) FITC-C1 lacked similar binding to T-iRBCs.

Various chelators have been reported regarding their effective incorporation for ^{68}Ga, however, DOTA was selected in this study since it is the most utilized bifunctional chelator for ^{68}Ga and has a well-renowned acceptance in the clinical setting. For instance, [^{68}Ga]Ga-DOTA-TOC has been approved by the Food and Drug Administration (FDA) in 2019 as the first ^{68}Ga-radiopharmaceutical for imaging of somatostatin receptor-positive gastro-enteropancreatic neuroendocrine tumours [262]. The knowledge reported on DOTA, being an organic molecule consisting of a central 12-membered tetra-aza ring which is an excellent chelating moiety for radiometal binding, yielded in several DOTA-peptides being rapidly and efficiently labelled with ^{68}Ga. Radiolabelling DOTA does, however, has limitations which are mainly linked to slower radiolabelling kinetics and high activation energies necessary for its complexation [260]. Prolonged heating of up to 95°C is often essential to get higher labelling efficiencies, in turn, this limits its use with heat sensitive vectors like

mAbs. However, in this study, DOTA has facilitated efficient labelling of P1 and C1 in as little as 12 min. It remains to be determined whether lower vector molarities and/or periods of incubation would allow for a similar performance.

Routine preparation of ^{68}Ga-labelled DOTA-radiopharmaceuticals generally involves elution of ^{68}Ga activity from a generator, pre-treatment of eluate radioactivity (i.e., to removal of impurities or pH adjustment), and an incubation period allowing for ^{68}Ga to be complexed by the peptide-chelator precursor during heating. The subsequent step often will include elimination of unreacted ^{68}Ga-species and/or buffering salts, and formulation of the radiopharmaceutical to physiological acceptable condition – ready compliant for potential *in vivo* administration (e.g., intravenous bolus injection of the formulated radiopharmaceutical) [263]. Those various steps may be a challenge to the radiopharmaceutical's stability which therefore is considerable parameter to be ascertained of during its development phase. This study presented radiolabelling conditions that provided [^{68}Ga]Ga-DOTA-P1 that meets the criteria for a product release. It remained stable at various short-term benchtop conditions, thus for instant warranting administration to several animals or justify further *in vitro* testing. Additionally, in most cases, the superior RCY did not require purification of [^{68}Ga]Ga-DOTA-P1 from any free ^{68}Ga and the removal of buffering salts with the SepPak cartridge was effective. Long labelling reactions and additional purification steps can pose a limitation when it comes to radionuclides with such a short half-life such as ^{68}Ga. [^{68}Ga]Ga-DOTA-P1 also demonstrated more robust RCP when exposed to challenging conditions than [^{68}Ga]Ga-DOTA-C1. This could be attributed to the higher structural stability of cyclised peptides ([^{68}Ga]Ga-DOTA-P1) *vs.* linear peptides ([^{68}Ga]Ga-DOTA-C1).

A major drawback often experienced with radiolabelled peptides can be their low metabolic stability due to proteases and peptidases activity present in most tissues [264, 265]. However, their stability can be improved, for instance by cyclisation of the peptide (such as it was opted for in this study) or designing the peptide with non-biodegradable peptide bonds, terminal capping (N-acetylation or C-amidation) or by replacing natural amino acid derivatives with stable unnatural amino acids or D-isomers [247, 264, 266]. To assess the potential *in vivo* stability of [^{68}Ga]Ga-DOTA-P1, the compound's stability and distribution in whole blood and serum was assessed. After 60 min incubation, the compound maintained a >99% RCP and therefore no

improvements to the compound were considered at this point. In drug development, the free drug hypothesis has been widely used as an indication to prioritise a compound for *in vivo* studies [267]. This theory states that only free drug (not bound to serum proteins) can reach the target site, i.e., only the free drug concentration is responsible for the pharmacological effect/activity of the compound [268, 269]. The *in vitro* binding of a protein/drug to serum proteins does have an effect on the pharmacokinetics and pharmacodynamics of a drug; however, it does not necessarily indicate the availability of a drug at the site of action [268, 270]. In the case where a radiolabelled peptide is used as an imaging tracer, binding to serum proteins have shown to enhance the half-life of the tracer and thereby improving the pharmacokinetics and imaging efficiency [271]. The high percentage of [^{68}Ga]Ga-DOTA-P1 bound to serum proteins is therefore not of much concern for future *in vivo* studies, however, a serum protein binding assay may be recommended to determine the actual proteins that [^{68}Ga]Ga-DOTA-P1 is associated with. Because malaria is a blood-borne disease, it was important to assess the binding of [^{68}Ga]Ga-DOTA-P1 to uninfected RBC. The binding of [^{68}Ga]Ga-DOTA-P1 to T-iRBCs *in vitro* was not assessed in this study considering that these results would differ tremendously in an *in vivo* setup. The binding behaviour to RBCs and *in vitro* integrity of the radiolabelled product would be a prerequisite that pre-clinical evaluation of [^{68}Ga]Ga-DOTA-P1 can commence as part of future studies. It is recommended that the scope for further investigations on [^{68}Ga]Ga-DOTA-P1 will require to address the need for suitable small animal models and focus on overcoming the lack of biosafety laboratory environment to perform *in vivo* experiments with malaria-infected animals. need

Herein, positive, confirmative binding properties of FITC-P1 to T-iRBCs, a straightforward radiolabelling protocol for [^{68}Ga]Ga-DOTA-P1 along with its radioisotopic metal constancy under various challenging conditions, high serum stability and its low-level RBC binding properties are presented. The results appropriately support the tracer to be recommended for pre-clinical assessment as part of its prospective development. Considering that [^{68}Ga]Ga-DOTA-P1 will demonstrate favourable biodistribution in healthy mice, it would be of high value to evaluate the tracer in animals infected with *P. falciparum*.

Chapter 5

Concluding discussion

If left untreated, *P. falciparum* predominantly progresses to SM which can result in death [1, 272]. SM is a multisystem disease with various host- and pathogen-related factors influencing the development, and therefore the clinical manifestations of SM can differ from patient to patient [64, 273, 274]. Although numerous studies have been conducted on SM and some key findings have enabled a better understanding of the disease, there are still several knowledge gaps regarding the complex mechanisms underlying the pathophysiology of malaria. Investigations set out to further comprehend SM pathogenesis have thus far mainly relied on post-mortem examinations (organ pathology e.g., cerebral tissue analysis in cases of CM) and analyses of experimental malaria in animal models [133, 136, 275, 276]. While such post-mortem evaluations were helpful and revealed important findings that improved the understanding the parasite pathogenesis, they are limited to samples obtained only at the terminal stage of the disease. Unfortunately, researchers are yet not given the ability to investigate the longitudinal pathogenesis in real time [277].

In terms of laboratory animal models, mice strains are very widely used, however, there are numerous differences reported when comparing human and murine malaria [278-280]. Non-human primate models exhibit more similar pathological features to human SM, however, the use of larger animals is expensive and often ethically difficult to justify [281-283]. All these shortcomings evidently urging for novel strategies that would enable studying SM patients instantaneously and thereby provide valued pieces of an in-depth understanding of the complex malaria pathology.

Real-time *in vivo* imaging, a non-invasive technique in nuclear medicine, indeed allows to detect and/or track longitudinal pathophysiological changes in humans and animals at a cellular level [284]. Regarding infectious diseases, molecular imaging procedures can assist in diagnosis and localization of the infectious foci, assessment of the host's reaction and interaction with the pathogen. In addition, it allows the monitoring of disease progression, fast tracking of drug development, or is of valuable assistance in

treatment planning [285]. In particular, the use of PET-imaging as a targeted molecular imaging technique provides a three-dimensional, holistic view into the whole body with superior sensitivity and specificity. In the past 50 years nuclear imaging has already been successfully used in studying infectious diseases and thereby improved global healthcare in clinical practice [179, 181, 286]. To the best of our knowledge, to date there are no *P. falciparum*-specific radiotracers that have been developed. In the absence of SM-associated radiotracers the body of literature referring to malaria imaging has been limited to [^{18}F]FDG-PET imaging – a non-specific technique unable to distinguish between different infectious diseases, cancers, or inflammatory processes. This current nuclear imaging technique could lead to misdiagnosis of SM and thereby delay the onset of treatment of the patient. Any improvements towards the development of *P. falciparum*-specific tracers would allow nuclear imaging to have a significant impact on clinical diagnosis of SM and grasping factors associated with the severity.

Therefore, this study aims to provide *P. falciparum*-specific radiotracer candidates for potentially imaging SM *in vivo* with non-invasive PET-imaging. Discovering or further characterizing molecules that are capable of targeting a disease-specific expression of cellular surface structures can be considered a suitable strategy to develop such radiotracers for molecular imaging.

Although SM is a multifactorial disease, there is a convincing body of evidence from clinical studies (e.g., retinal sequestration visible in CM) and post-mortem evaluations that major manifestations of SM are caused by parasite sequestration that can lead to significant organ dysfunction [287-289]. Therefore, this study set out to develop the first candidate radiotracers specific to *P. falciparum*-iRBCs in late asexual stages that are known to sequester in tissues and ultimately cause SM.

Immuno-PET utilising ^{89}Zr-radiolabelled antibody-based molecules has been regarded as a desirable strategy in radiochemistry to foster eventual PET imaging of malaria. Our efficient radiosynthesis protocol achieved [^{89}Zr]Zr-Pf-Fab and [^{89}Zr]Zr-IIIB6 in appropriate quality suitable for further pre-clinical characterisation including the exclusive demonstration of PET image-derived, real-time pharmacokinetics and *in vivo* (dynamic image-guided) biodistribution. Unlike [^{89}Zr]Zr-IIIB6, the key value of [^{89}Zr]Zr-Pf-Fab was hinged on its rapid elimination from organs at risk for malaria

(spleen, lungs, and liver). Hence, these favourably-low radiotracer levels are prerequisites for significant target-to-non-target ratios congruently occurring with malaria infection. The *in vivo* [^{89}Zr]Zr-Pf-Fab characterisation achieved in this work is unreported in literature and opens the opportunity to utilize its PET imaging properties towards malaria-infected mice, thereby validating whether this radiotracer meets the criteria as a malaria imaging agent for clinical trial investigations. Due to the evident differences between human malaria and murine malaria, using a humanised mouse model infected with *P. falciparum* would be a possible key for success for additional pre-clinical evaluation of [^{89}Zr]Zr-Pf-Fab considering its preparation for human investigations. Such humanised mice have already been proven successful to study human diseases [290-296]. In particular, the NOD/SCID/IL2Rγ^{null} (NSG) mouse model has several characteristics that would be useful furthering our study, for instance NSG mice are receptive to human erythrocytes and *P. falciparum* parasites without the need for a lengthy pre-adaptation of the animals to the parasites [297, 298]. Previously, these mice have shown a high reproducibility with consistent parasitaemia patterns amongst grouped animals. In addition, NSG mice are known to reach high parasitaemia levels, show rapid growth of healthy parasites, and exhibit partial sequestration with development of gametocyte sexual stages [297]. Hereby, [^{89}Zr]Zr-Pf-Fab's capability to detect and trace iRBCs may be suited in NSG mice to identify its full potential as an imaging agent. Our results also support a recommendation of [^{89}Zr]Zr-Pf-Fab for first in-human studies given that both, a tracer safety pharmacology profiling, and the GMP-compliant preparation, are available. In addition, [^{89}Zr]Zr-Pf-Fab-PET imaging may serve as an excellent tool for malaria drug and/or vaccine development, both pre-clinically and clinically. For drug development, [^{89}Zr]Zr-Pf-Fab-PET imaging could enable repeated monitoring of malaria progression or response to treatment non-invasively [299].

Other strategies for introducing new radiotracers to molecular imaging suggest the use of *in vitro* display technologies over hybridoma technology due to several advantages such as high adaptability and large-scale throughput. Phage display technology is a unique tool that allows for an easy, inexpensive, and robust production of recombinant antibody fragments (including scFvs). In addition to their economic production, in particular scFvs demonstrate favourable pharmacokinetic patterns and reduced immunogenicity compared to mAbs [203, 300]. Potential *in vivo* applications for scFvs

are highlighted towards studying protein functions, assisting with drug delivery, and *in vivo* imaging [204, 301-303]. The growing popularity and significance of scFv as biomarkers for *in vivo* applications encouraged our study to focus on the discovery of scFvs specific towards *P. falciparum*-infected erythrocytes. Previously, the development of *P. falciparum*-specific scFvs relied on biopanning against unique malaria expressed proteins, i.e., surface antigens that are otherwise not represented during their natural and healthy state of a blood cell [217-219]. Also, by technically narrowing the panning process towards a single antigen, the scFv discovery is greatly limited to circumstances in which this individual antigen is expressed (a predicament for *in vivo* imaging of the malaria parasite that expresses variant antigens throughout its life cycle). Building on the advantages of scFvs-based *in vivo* tracers, our study set out to screen antibody phage libraries for scFvs that bind to whole live *P. falciparum*-infected erythrocytes. However, technical challenges by way of working with live parasites was evident from early on. By attempting to keep the T-iRBC in the most natural state during our ELISA-based screening strategies, poor cell immobilisation and high background signal remained the main constraints in detecting T-iRBC-specific scFvs. Additionally, the anti-c-myc antibody bound to T-iRBCs (as seen by confocal microscopy, Figure 3.12); thereby pointing out the insufficiency of using this antibody, and perhaps any other antibodies, as detection tool for scFvs. It should be considered that longitudinal stress put on the T-iRBCs (e.g., culturing parasites to a high parasitaemia, magnetic enrichment of T-iRBCs, long incubation times in PBS (lack of nutrients contained in complete culture medium) could have led to pronounced altering of the T-iRBC membrane to the highly permeable state, and thereby possibly allowed the antibody to enter the T-iRBC. This theory was supported (see chapter 4) by the fact that, under normal culturing conditions, a much smaller molecule (herein the linear peptide FITC-C1) does not enter and bind non-specifically to T-iRBCs. Evidently for future investigations, concerns are raised to avoid putting the parasite under too much strain during the selection process, i.e., reviewing issues on reaching the required parasite quantity, the magnetic enrichment process yielding the T-iRBCs, and the validity of the numerous wash steps could allow for better assay parameters. The limitation in this objective therefore remains in the detection mechanism and strategy used for screening for scFv clones [304]. On this note, other investigations have accomplished scFv-based tracers with excellent potential to be used further in the clinical setting [305, 306].

In fact, PET-imaging procedures are not restricted to antibody-based radiotracers. For instance, peptide-based radiopharmaceuticals have also proven successful in staging and localisation of diseases and, due to their favourable pharmacokinetics, are in some cases preferred over antibodies [307]. In this study, the *P. falciparum*-reactive peptide, P1, was radiolabelled and evaluated as a future candidate radiotracer for *in vivo* imaging of malaria or antimalarial drug development. To match the short *in vivo* circulation time of peptides, the short-lived radioisotope, ^{68}Ga was chosen as a radionuclide for P1. Our rapid, but consistent, and high-quality radiosynthesis of [^{68}Ga]Ga-DOTA-P1 granted further characterisation of this radiotracer, such as tracer serum stability and binding properties to erythrocytes. In addition to the selective binding of FITC-P1 to T-iRBCs, superior serum stability of [^{68}Ga]Ga-DOTA-P1 encourages future pre-clinical characterisation using [^{68}Ga]Ga-DOTA-P1-PET imaging. It will allow for image-guided pharmacokinetics and *in vivo* biodistribution of [^{68}Ga]Ga-DOTA-P1 in healthy mice which may further motivate for pre-clinical evaluation of [^{68}Ga]Ga-DOTA-P1 in malaria-infected mice.

In addition, to further justify the *in vivo* characterisation of [^{68}Ga]Ga-DOTA-P1, this radiotracer could be evaluated for binding to human cells that are usually involved in SM. The anticipated clinical need for [^{68}Ga]Ga-DOTA-P1 hinges on its low unspecific uptake and fast clearance from organs known for parasite sequestration, which will promise high value and prospects for accurate PET-imaging of malaria pathology. Furthermore, given [^{68}Ga]Ga-DOTA-P1 meets the criteria regarding tracer sensitivity and accuracy for SM, its use can be further expanded as a tool for malaria drug and/or vaccine development.

In vivo applications of disease-targeting peptides are obviously not limited to nuclear or molecular imaging alone. Peptides can furthermore be valuable in therapeutic field, either by directly treating the disease (e.g., inhibiting essential cellular activities, activating an immune response, or induce cell death) or by assisting in drug delivery and thereby increasing the drug's efficiency (e.g., peptides may act as delivering agents when conjugated to small-molecule drugs) [308-310]. Such peptide conjugates have also been explored and discovered in the malaria research to study their anti-malarial activities[311]. Their anti-malarial properties hereby hinge on their ability to either permeabilise or lyse the iRBC membrane, inhibit parasite invasion into RBCs and/or inhibit essential mechanisms for parasite survival (e.g., inhibiting haemoglobin

digestion) [253, 312-315]. P1 has been explored for its potential to serve as a drug delivery peptide. By conjugating a synthetic haemolytic peptide to P1, the growth of the parasites were significantly inhibited and the antimalarial activity enhanced when compared to unconjugated peptides [221]. With such a conjugated P1 derivative growth of the parasites was significantly inhibited and the antimalarial activity enhanced when compared to the unconjugated peptide. Although the compound's inhibitory activity was not sufficient be motivated for further testing as an ani-malarial drug itself, P1 will be investigated as a drug delivery peptide for other (more potent) anti-malarial drugs.

Even though a faster clearance and easier tissue penetration of radiotracers (e.g., smaller fragment antibodies and peptides) are usually beneficial for *in vivo* imaging, one should consider that extended pharmacological half-lives of full-length antibodies could allow longitudinal imaging and thereby provide the framework of gathering information on the pathological development of a disease. Although this scenario could provide vital information about the host-pathogen interactions resulting in SM, the drawback of full length mAbs remains in their extensive hepatic accumulation and consequently causing a high radiation burden in this organ. If research is aimed to focus on liver-sequestering parasites, repeated injections of the smaller fragments or peptides could be more advantages. Nevertheless, it depends on how the pharmacokinetics of these different probes may change in the presence of a *P. falciparum*-infection.

The achievement in this work is not merely limited to malaria. Co-infection of malaria and other diseases leads to the worsening of the clinical outcomes [316-319]. For Africa in particular, the prevalence of malaria and TB and/or HIV/AIDS coinfection put a high burden on the developing countries [318, 320-322]. *P. falciparum*-specific tracers could have a great value in patients suffering from SM with co-morbidities by permitting fast clinical diagnosis, better understanding of co-infection's interferences with treatments, and thereby may decrease the mortality associated with these co-infections.

The findings presented in this work demonstrate the pioneering development of *P. falciparum*-specific radiotracers for prospective nuclear imaging in a clinical setting or recommended use in future investigations of SM and/or malaria drug development.

Our probe development toward imaging of SM may be useful to expand the understanding of the pathology, influence clinical diagnosis and assess treatment. Major contributions to the drug development field may be cautiously assumed (e.g., the evaluation of pharmacological effects related to drug mechanism). In alignment with the use of these probes for drug discovery, significant benefits regarding the choice of anti-malarial therapy and lower mortality rate may be conceivable. Given further preclinical development, these probes, in particular [^{89}Zr]Zr-Fab but also [^{68}Ga]Ga-DOTA-P1, could substantially increase the knowledge on SM and ultimately allow clinicians to opt for using non-invasive, whole-body imaging of patients presenting with SM. Further investigations, focusing on malaria-disease related applications, both preclinical and clinical are permitted and proposed.

References

1. Brejt, J.A. and L.M. Golightly, *Severe malaria: update on pathophysiology and treatment.* Current opinion in infectious diseases, 2019. **32**(5): p. 413-418.
2. WHO. *World Malaria Report*. 2020 [cited 2020 29 August]; Available from: https://www.who.int/teams/global-malaria-programme/reports/world-malaria-report-2020.
3. Fried, M. and P.E. Duffy, *Malaria during pregnancy.* Cold Spring Harbor perspectives in medicine, 2017. **7**(6): p. a025551.
4. Walloch, P., et al., *Pentafluoro-3-hydroxy-pent-2-en-1-ones potently inhibit FNT-type lactate transporters from all five human-pathogenic Plasmodium species.* ChemMedChem, 2021. **16**(8): p. 1283.
5. White, N., *Plasmodium knowlesi: the fifth human malaria parasite*. 2008, The University of Chicago Press.
6. Derbie, A., et al., *Therapeutic efficacy of artemether-lumefantrine (Coartem®) for the treatment of uncomplicated falciparum malaria in Africa: a systematic review.* Journal of Parasitology Research, 2020. **2020**.
7. Frischknecht, F. and K. Matuschewski, *Plasmodium sporozoite biology.* Cold Spring Harbor Perspectives in Medicine, 2017. **7**(5): p. a025478.
8. Silvie, O., et al., *Interactions of the malaria parasite and its mammalian host.* Current opinion in microbiology, 2008. **11**(4): p. 352-359.
9. Bannister, L. and G. Mitchell, *The ins, outs and roundabouts of malaria.* Trends in parasitology, 2003. **19**(5): p. 209-213.
10. Gaur, D., D.G. Mayer, and L.H. Miller, *Parasite ligand–host receptor interactions during invasion of erythrocytes by Plasmodium merozoites.* International journal for parasitology, 2004. **34**(13-14): p. 1413-1429.
11. Girard, M.P., et al., *A review of human vaccine research and development: malaria.* Vaccine, 2007. **25**(9): p. 1567-1580.
12. Josling, G.A. and M. Llinás, *Sexual development in Plasmodium parasites: knowing when it's time to commit.* Nature Reviews Microbiology, 2015. **13**(9): p. 573-587.
13. Tibúrcio, M., et al., *A switch in infected erythrocyte deformability at the maturation and blood circulation of Plasmodium falciparum transmission stages.* Blood, The Journal of the American Society of Hematology, 2012. **119**(24): p. e172-e180.
14. Joice, R., et al., *Plasmodium falciparum transmission stages accumulate in the human bone marrow.* Science translational medicine, 2014. **6**(244): p. 244re5-244re5.
15. Neveu, G. and C. Lavazec, *Erythrocyte Membrane Makeover by Plasmodium falciparum Gametocytes.* Frontiers in Microbiology, 2019. **10**(2652).
16. Guttery, D.S., et al., *Commit and transmit: molecular players in Plasmodium sexual development and zygote differentiation.* Trends in parasitology, 2015. **31**(12): p. 676-685.
17. van Schaijk, B.C., et al., *Type II fatty acid biosynthesis is essential for Plasmodium falciparum sporozoite development in the midgut of Anopheles mosquitoes.* Eukaryotic cell, 2014. **13**(5): p. 550-559.
18. Bennink, S., M.J. Kiesow, and G. Pradel, *The development of malaria parasites in the mosquito midgut.* Cellular microbiology, 2016. **18**(7): p. 905-918.

19. Venugopal, K., et al., *Plasmodium asexual growth and sexual development in the haematopoietic niche of the host.* Nature Reviews Microbiology, 2020. **18**(3): p. 177-189.
20. Bartoloni, A. and L. Zammarchi, *Clinical aspects of uncomplicated and severe malaria.* Mediterranean journal of hematology and infectious diseases, 2012. **4**(1).
21. Coban, C., M.S.J. Lee, and K.J. Ishii, *Tissue-specific immunopathology during malaria infection.* Nature Reviews Immunology, 2018. **18**(4): p. 266.
22. Patel, H., C. Dunican, and A.J. Cunnington, *Predictors of outcome in childhood Plasmodium falciparum malaria.* Virulence, 2020. **11**(1): p. 199-221.
23. Ishioka, H., et al., *Sequestration and red cell deformability as determinants of hyperlactatemia in falciparum malaria.* The Journal of infectious diseases, 2016. **213**(5): p. 788-793.
24. Schofield, L. and G.E. Grau, *Immunological processes in malaria pathogenesis.* Nature Reviews Immunology, 2005. **5**(9): p. 722-735.
25. Deroost, K., et al., *The immunological balance between host and parasite in malaria.* FEMS microbiology reviews, 2016. **40**(2): p. 208-257.
26. de Azevedo-Quintanilha, I.G., et al., *Haem oxygenase protects against thrombocytopaenia and malaria-associated lung injury.* Malaria Journal, 2020. **19**(1): p. 1-16.
27. Wassmer, S.C., et al., *Investigating the pathogenesis of severe malaria: a multidisciplinary and cross-geographical approach.* The American journal of tropical medicine and hygiene, 2015. **93**(3_Suppl): p. 42-56.
28. Buffet, P.A., et al., *The pathogenesis of Plasmodium falciparum malaria in humans: insights from splenic physiology.* Blood, The Journal of the American Society of Hematology, 2011. **117**(2): p. 381-392.
29. Balaji, S., R. Deshmukh, and V. Trivedi, *Severe malaria: Biology, clinical manifestation, pathogenesis and consequences.* Journal of Vector Borne Diseases, 2020. **57**(1): p. 1.
30. Looareesuwan, S., et al., *Erythrocyte survival in severe falciparum malaria.* Acta tropica, 1991. **48**(4): p. 263-270.
31. Matthews, K., et al., *Microfluidic analysis of red blood cell deformability as a means to assess hemin-induced oxidative stress resulting from Plasmodium falciparum intraerythrocytic parasitism.* Integrative Biology, 2017. **9**(6): p. 519-528.
32. Kurtzhals, J., et al., *Reversible suppression of bone marrow response to erythropoietin in Plasmodium falciparum malaria.* British journal of haematology, 1997. **97**(1): p. 169-174.
33. Jakeman, G., et al., *Anaemia of acute malaria infections in non-immune patients primarily results from destruction of uninfected erythrocytes.* Parasitology, 1999. **119**(2): p. 127-133.
34. Gallo, V., et al., *Simultaneous determination of phagocytosis of Plasmodium falciparum-parasitized and non-parasitized red blood cells by flow cytometry.* Malaria journal, 2012. **11**(1): p. 1-11.
35. Goka, B.Q., et al., *Complement binding to erythrocytes is associated with macrophage activation and reduced haemoglobin in Plasmodium falciparum malaria.* Transactions of the Royal Society of Tropical Medicine and Hygiene, 2001. **95**(5): p. 545-549.

36. Waitumbi, J.N., et al., *Red cell surface changes and erythrophagocytosis in children with severe Plasmodium falciparum anemia.* Blood, The Journal of the American Society of Hematology, 2000. **95**(4): p. 1481-1486.
37. Moxon, C.A., et al., *New insights into malaria pathogenesis.* Annual Review of Pathology: Mechanisms of Disease, 2020. **15**: p. 315-343.
38. White, N.J., *Malaria parasite clearance.* Malaria journal, 2017. **16**(1): p. 88.
39. Mohan, K. and M. Stevenson, *Dyserythropoiesis and severe anaemia associated with malaria correlate with deficient interleukin-12 production.* British journal of haematology, 1998. **103**(4): p. 942-949.
40. Casals-Pascual, C., et al., *Suppression of erythropoiesis in malarial anemia is associated with hemozoin in vitro and in vivo.* Blood, 2006. **108**(8): p. 2569-2577.
41. Jadhav, V.Y., et al., *CEREBRAL MALARIA: NEUROPATHOGENESIS AND INNOVATIVE THERAPEUTIC APPROACHES.* Journal of Advanced Scientific Research, 2020. **11**.
42. Siddiqui, A.J., et al., *Neurological disorder and psychosocial aspects of cerebral malaria: what is new on its pathogenesis and complications? A minireview.* Folia Parasitologica, 2020. **67**: p. 015.
43. Bernabeu, M., et al., *Binding heterogeneity of Plasmodium falciparum to engineered 3D brain microvessels is mediated by EPCR and ICAM-1.* MBio, 2019. **10**(3).
44. Nishanth, G. and D. Schlüter, *Blood–brain barrier in cerebral malaria: Pathogenesis and therapeutic intervention.* Trends in parasitology, 2019. **35**(7): p. 516-528.
45. Sahu, P.K., et al., *Pathogenesis of cerebral malaria: new diagnostic tools, biomarkers, and therapeutic approaches.* Frontiers in cellular and infection microbiology, 2015. **5**: p. 75.
46. Silva, G.B.d.J., et al., *Kidney involvement in malaria: an update.* Revista do Instituto de Medicina Tropical de Sao Paulo, 2017. **59**: p. e53-e53.
47. Quirino, T.d.C., et al., *Lung aeration in experimental malaria-associated acute respiratory distress syndrome by SPECT/CT analysis.* Plos one, 2020. **15**(5): p. e0233864.
48. Quintanilha, I.G., et al. *Haem oxygenase protects against thrombocytopaenia and malaria-associated lung injury*. 2020. BMC.
49. Mackintosh, C.L., J.G. Beeson, and K. Marsh, *Clinical features and pathogenesis of severe malaria.* Trends in parasitology, 2004. **20**(12): p. 597-603.
50. Gupta, S., et al., *Malaria and the Heart: JACC State-of-the-Art Review.* Journal of the American College of Cardiology, 2021. **77**(8): p. 1110-1121.
51. Ssenkusu, J.M., et al., *Long-term behavioral problems in children with severe malaria.* Pediatrics, 2016. **138**(5).
52. Mbengue, A., X.Y. Yam, and C. Braun-Breton, *Human erythrocyte remodelling during P lasmodium falciparum malaria parasite growth and egress.* British journal of haematology, 2012. **157**(2): p. 171-179.
53. Tilley, L., M.W. Dixon, and K. Kirk, *The Plasmodium falciparum-infected red blood cell.* The international journal of biochemistry & cell biology, 2011. **43**(6): p. 839-842.
54. Starnes, G.L. and A.P. Waters, *Home improvements: how the malaria parasite makes the red blood cell home sweet home.* Journal of molecular cell biology, 2010. **2**(1): p. 11-13.

55. Nilsson, S., *Exported proteins of the malaria parasite Plasmodium falciparum.* 2011.
56. Spielmann, T., et al., *Molecular make-up of the Plasmodium parasitophorous vacuolar membrane.* International Journal of Medical Microbiology, 2012. **302**(4-5): p. 179-186.
57. Counihan, N.A., et al., *How malaria parasites acquire nutrients from their host.* Frontiers in Cell and Developmental Biology, 2021. **9**: p. 582.
58. Dalapati, T. and J.M. Moore, *Hemozoin: a Complex Molecule with Complex Activities.* Current Clinical Microbiology Reports, 2021: p. 1-16.
59. De Niz, M., et al., *Progress in imaging methods: insights gained into Plasmodium biology.* Nature Reviews Microbiology, 2017. **15**(1): p. 37-54.
60. Goldberg, D.E., et al., *Hemoglobin degradation in the malaria parasite Plasmodium falciparum: an ordered process in a unique organelle.* Proceedings of the National Academy of Sciences, 1990. **87**(8): p. 2931-2935.
61. Krugliak, M., J. Zhang, and H. Ginsburg, *Intraerythrocytic Plasmodium falciparum utilizes only a fraction of the amino acids derived from the digestion of host cell cytosol for the biosynthesis of its proteins.* Molecular and biochemical parasitology, 2002. **119**(2): p. 249-256.
62. Kapishnikov, S., et al., *Malaria Pigment Crystals: The Achilleso Heel of the Malaria Parasite.* ChemMedChem, 2021. **16**: p. 1515-1532.
63. Matthews, K.M., E.L. Pitman, and T.F. de Koning-Ward, *Illuminating how malaria parasites export proteins into host erythrocytes.* Cellular microbiology, 2019. **21**(4): p. e13009.
64. Mahamar, A., et al., *Host factors that modify Plasmodium falciparum adhesion to endothelial receptors.* Scientific reports, 2017. **7**(1): p. 1-8.
65. Kirk, K. and A.M. Lehane, *Membrane transport in the malaria parasite and its host erythrocyte.* Biochemical Journal, 2014. **457**(1): p. 1-18.
66. Beck, J.R. and C.-M. Ho, *Transport mechanisms at the malaria parasite-host cell interface.* PLoS Pathogens, 2021. **17**(4): p. e1009394.
67. de Koning-Ward, T.F., et al., *Plasmodium species: master renovators of their host cells.* Nature Reviews Microbiology, 2016. **14**(8): p. 494-507.
68. Mesén-Ramírez, P., et al., *EXP1 is critical for nutrient uptake across the parasitophorous vacuole membrane of malaria parasites.* PLoS biology, 2019. **17**(9): p. e3000473.
69. Hanssen, E., et al., *Whole cell imaging reveals novel modular features of the exomembrane system of the malaria parasite, Plasmodium falciparum.* International journal for parasitology, 2010. **40**(1): p. 123-134.
70. Oh, S.S., et al., *Plasmodium falciparum erythrocyte membrane protein 1 is anchored to the actin–spectrin junction and knob-associated histidine-rich protein in the erythrocyte skeleton.* Molecular and biochemical parasitology, 2000. **108**(2): p. 237-247.
71. Cooke, B.M., et al., *Protein trafficking in Plasmodium falciparum-infected red blood cells.* Trends in parasitology, 2004. **20**(12): p. 581-589.
72. Li, H., et al., *Mechanics of diseased red blood cells in human spleen and consequences for hereditary blood disorders.* Proceedings of the National Academy of Sciences, 2018. **115**(38): p. 9574-9579.
73. Dhangadamajhi, G., S.K. Kar, and M. Ranjit, *The survival strategies of malaria parasite in the red blood cell and host cell polymorphisms.* Malaria research and treatment, 2010. **2010**.

74. Li, I.W.S. and L.C.P. Cheung, *How Not to Miss a Case of Malaria in Emergency Department in Malaria Non-Endemic Areas? Practical Approach & Experiences in Hong Kong.* Open Journal of Emergency Medicine, 2016. **4**(04): p. 93.
75. Yam, X.Y., et al., *Three is a crowd–new insights into rosetting in Plasmodium falciparum.* Trends in parasitology, 2017. **33**(4): p. 309-320.
76. Janes, J.H., et al., *Investigating the host binding signature on the Plasmodium falciparum PfEMP1 protein family.* PLoS pathogens, 2011. **7**(5): p. e1002032.
77. Lalchhandama, K., *Plasmodium falciparum erythrocyte membrane protein 1.* WikiJournal of Medicine, 2017. **4**(1): p. 1.
78. Goel, S., et al., *RIFINs are adhesins implicated in severe Plasmodium falciparum malaria.* Nature medicine, 2015. **21**(4): p. 314-317.
79. Niang, M., et al., *STEVOR is a Plasmodium falciparum erythrocyte binding protein that mediates merozoite invasion and rosetting.* Cell host & microbe, 2014. **16**(1): p. 81-93.
80. Tibúrcio, M., et al., *Erythrocyte remodeling by Plasmodium falciparum gametocytes in the human host interplay.* Trends in parasitology, 2015. **31**(6): p. 270-278.
81. Dinko, B. and G. Pradel, *Immune evasion by Plasmodium falciparum parasites: converting a host protection mechanism for the parasite' s benefit.* Advances in Infectious Diseases, 2016. **6**(2): p. 82-95.
82. Gardner, M.J., et al., *Genome sequence of the human malaria parasite Plasmodium falciparum.* Nature, 2002. **419**(6906): p. 498-511.
83. Wahlgren, M., S. Goel, and R.R. Akhouri, *Variant surface antigens of Plasmodium falciparum and their roles in severe malaria.* Nature Reviews Microbiology, 2017. **15**(8): p. 479-491.
84. Smith, J.D., et al., *Malaria's deadly grip: cytoadhesion of P lasmodium falciparum-infected erythrocytes.* Cellular microbiology, 2013. **15**(12): p. 1976-1983.
85. Moxon, C.A., G.E. Grau, and A.G. Craig, *Malaria: modification of the red blood cell and consequences in the human host.* British journal of haematology, 2011. **154**(6): p. 670-679.
86. Cheng, Q., et al., *stevor and rif are Plasmodium falciparum multicopy gene families which potentially encode variant antigens.* Molecular and biochemical parasitology, 1998. **97**(1-2): p. 161-176.
87. Petter, M., I. Bonow, and M.-Q. Klinkert, *Diverse expression patterns of subgroups of the rif multigene family during Plasmodium falciparum gametocytogenesis.* PloS one, 2008. **3**(11): p. e3779.
88. Lee, W.-C. and L. Rénia, *Sticking for a cause: the falciparum malaria parasites cytoadherence paradigm.* Frontiers in immunology, 2019. **10**: p. 1444.
89. McRobert, L., et al., *Distinct trafficking and localization of STEVOR proteins in three stages of the Plasmodium falciparum life cycle.* Infection and immunity, 2004. **72**(11): p. 6597-6602.
90. Mousa, A., et al., *The impact of delayed treatment of uncomplicated P. falciparum malaria on progression to severe malaria: A systematic review and a pooled multicentre individual-patient meta-analysis.* PLoS medicine, 2020. **17**(10): p. e1003359.
91. Sahu, P.K., et al., *Pathogenesis of cerebral malaria: new diagnostic tools, biomarkers, and therapeutic approaches.* Frontiers in Cellular and Infection Microbiology, 2015. **5**(75).

92. Plewes, K., et al., *Correlation of biomarkers for parasite burden and immune activation with acute kidney injury in severe falciparum malaria.* Malaria journal, 2014. **13**(1): p. 1-10.
93. van Wolfswinkel, M.E., et al., *Neutrophil gelatinase-associated lipocalin (NGAL) predicts the occurrence of malaria-induced acute kidney injury.* Malaria journal, 2016. **15**(1): p. 1-8.
94. Lewallen, S., et al., *Retinal findings predictive of outcome in cerebral malaria.* Transactions of the Royal Society of Tropical Medicine and Hygiene, 1996. **90**(2): p. 144-146.
95. Beare, N.A., et al., *Redefining cerebral malaria by including malaria retinopathy.* Future microbiology, 2011. **6**(3): p. 349-355.
96. Bhardwaj, N., et al., *Clinicopathological study of potential biomarkers of Plasmodium falciparum malaria severity and complications.* Infection, Genetics and Evolution, 2020. **77**: p. 104046.
97. Varo, R., et al., *Adjunctive therapy for severe malaria: a review and critical appraisal.* Malaria journal, 2018. **17**(1): p. 1-18.
98. Gordon, O., et al., *Molecular imaging: A novel tool to visualize pathogenesis of infections in situ.* MBio, 2019. **10**(5): p. e00317-19.
99. Lauber, D.T., et al., *State of the art in vivo imaging techniques for laboratory animals.* Laboratory animals, 2017. **51**(5): p. 465-478.
100. Hunter, P., *Illuminating human disease: The potential of in vivo imaging for preclinical research and diagnostics.* EMBO reports, 2019. **20**(10): p. e49195.
101. Wallyn, J., et al., *Biomedical Imaging: Principles, Technologies, Clinical Aspects, Contrast Agents, Limitations and Future Trends in Nanomedicines.* Pharmaceutical research, 2019. **36**(6).
102. Wallyn, J., et al., *Biomedical Imaging: Principles, Technologies, Clinical Aspects, Contrast Agents, Limitations and Future Trends in Nanomedicines.* Pharmaceutical Research, 2019. **36**(6): p. 78.
103. Koo, V., P. Hamilton, and K. Williamson, *Non-invasive in vivo imaging in small animal research.* Analytical Cellular Pathology, 2006. **28**(4): p. 127-139.
104. Stradiotti, P., et al., *Metal-related artifacts in instrumented spine. Techniques for reducing artifacts in CT and MRI: state of the art.* European Spine Journal, 2009. **18**(1): p. 102-108.
105. Greer III, L.F. and A.A. Szalay, *Imaging of light emission from the expression of luciferases in living cells and organisms: a review.* Luminescence: the journal of biological and chemical luminescence, 2002. **17**(1): p. 43-74.
106. Siciliano, G. and P. Alano, *Enlightening the malaria parasite life cycle: bioluminescent Plasmodium in fundamental and applied research.* Frontiers in microbiology, 2015. **6**: p. 391.
107. Pirovano, G., et al., *Optical imaging modalities: principles and applications in preclinical research and clinical settings.* Journal of Nuclear Medicine, 2020. **61**(10): p. 1419-1427.
108. Contag, C.H. and B.D. Ross, *It's not just about anatomy: in vivo bioluminescence imaging as an eyepiece into biology.* Journal of Magnetic Resonance Imaging: An Official Journal of the International Society for Magnetic Resonance in Medicine, 2002. **16**(4): p. 378-387.
109. Ghoroghchian, P.P., M.J. Therien, and D.A. Hammer, *In vivo fluorescence imaging: a personal perspective.* Wiley Interdisciplinary Reviews: Nanomedicine and Nanobiotechnology, 2009. **1**(2): p. 156-167.

110. Heppert, J.K., et al., *Comparative assessment of fluorescent proteins for in vivo imaging in an animal model system.* Molecular biology of the cell, 2016. **27**(22): p. 3385-3394.
111. Calvo-Alvarez, E., et al., *Infrared fluorescent imaging as a potent tool for in vitro, ex vivo and in vivo models of visceral leishmaniasis.* PLoS neglected tropical diseases, 2015. **9**(3): p. e0003666.
112. Nagaya, T., et al., *Fluorescence-guided surgery.* Frontiers in oncology, 2017. **7**: p. 314.
113. Sivasubramanian, M., Y. Hsia, and L.-W. Lo, *Nanoparticle-facilitated functional and molecular imaging for the early detection of cancer.* Frontiers in molecular biosciences, 2014. **1**: p. 15.
114. MacPherson, D.S., et al., *A brief overview of metal complexes as nuclear imaging agents.* Dalton Transactions, 2019. **48**(39): p. 14547-14565.
115. Ametamey, S.M., M. Honer, and P.A. Schubiger, *Molecular imaging with PET.* Chemical reviews, 2008. **108**(5): p. 1501-1516.
116. Wu, M. and J. Shu, *Multimodal molecular imaging: current status and future directions.* Contrast media & molecular imaging, 2018. **2018**.
117. Ganguly, B., et al., *Some physical aspects of positron annihilation tomography: A critical review.* Journal of radioanalytical and nuclear chemistry, 2009. **279**(2): p. 685-698.
118. Sathekge, M., A. Maes, and C. Van de Wiele. *FDG-PET imaging in HIV infection and tuberculosis*. in *Seminars in nuclear medicine*. 2013. Elsevier.
119. Sinharay, S. and D.A. Hammoud, *Brain PET imaging: value for understanding the pathophysiology of HIV-Associated Neurocognitive Disorder (HAND).* Current HIV/AIDS Reports, 2019. **16**(1): p. 66-75.
120. Ruth, T.J., *The uses of radiotracers in the life sciences.* Reports on Progress in Physics, 2008. **72**(1): p. 016701.
121. Gutfilen, B. and G. Valentini, *Radiopharmaceuticals in nuclear medicine: recent developments for SPECT and PET studies.* BioMed research international, 2014. **2014**.
122. Sturm, A., et al., *Manipulation of host hepatocytes by the malaria parasite for delivery into liver sinusoids.* science, 2006. **313**(5791): p. 1287-1290.
123. Frevert, U., et al., *Intravital observation of Plasmodium berghei sporozoite infection of the liver.* PLoS biology, 2005. **3**(6): p. e192.
124. Amino, R., et al., *Quantitative imaging of Plasmodium transmission from mosquito to mammal.* Nature medicine, 2006. **12**(2): p. 220-224.
125. Cabrales, P. and L.J. Carvalho, *Intravital microscopy of the mouse brain microcirculation using a closed cranial window.* JoVE (Journal of Visualized Experiments), 2010(45): p. e2184.
126. Ferrer, M., et al., *Intravital microscopy of the spleen: quantitative analysis of parasite mobility and blood flow.* Journal of visualized experiments: JoVE, 2012(59).
127. Ploemen, I.H., et al., *Visualisation and quantitative analysis of the rodent malaria liver stage by real time imaging.* PloS one, 2009. **4**(11): p. e7881.
128. Miller, J.L., et al., *Quantitative bioluminescent imaging of pre-erythrocytic malaria parasite infection using luciferase-expressing Plasmodium yoelii.* PloS one, 2013. **8**(4): p. e60820.
129. Siciliano, G. and P. Alano, *Enlightening the malaria parasite life cycle: bioluminescent Plasmodium in fundamental and applied research.* Frontiers in Microbiology, 2015. **6**(391).

130. Mwakingwe, A., et al., *Noninvasive real-time monitoring of liver-stage development of bioluminescent Plasmodium parasites.* The Journal of infectious diseases, 2009. **200**(9): p. 1470-1478.
131. LaCrue, A.N., et al., *4 (1 H)-Quinolones with liver stage activity against Plasmodium berghei.* Antimicrobial agents and chemotherapy, 2013. **57**(1): p. 417-424.
132. Franke-Fayard, B., et al., *Simple and sensitive antimalarial drug screening in vitro and in vivo using transgenic luciferase expressing Plasmodium berghei parasites.* International journal for parasitology, 2008. **38**(14): p. 1651-1662.
133. Franke-Fayard, B., A.P. Waters, and C.J. Janse, *Real-time in vivo imaging of transgenic bioluminescent blood stages of rodent malaria parasites in mice.* Nature protocols, 2006. **1**(1): p. 476-485.
134. Othman, A.S., et al., *The use of transgenic parasites in malaria vaccine research.* Expert review of vaccines, 2017. **16**(7): p. 685-697.
135. Salman, A.M., et al., *Generation of transgenic rodent malaria parasites expressing human malaria parasite proteins*, in *Malaria Vaccines*. 2015, Springer. p. 257-286.
136. Foquet, L., et al., *Plasmodium falciparum liver stage infection and transition to stable blood stage infection in liver-humanized and blood-humanized FRGN KO mice enables testing of blood stage inhibitory antibodies (reticulocyte-binding protein homolog 5) in vivo.* Frontiers in immunology, 2018. **9**: p. 524.
137. Mohanty, S., et al., *Magnetic resonance imaging during life: the key to unlock cerebral malaria pathogenesis?* Malaria journal, 2014. **13**(1): p. 1-8.
138. Patankar, T.F., et al., *Adult cerebral malaria: prognostic importance of imaging findings and correlation with postmortem findings.* Radiology, 2002. **224**(3): p. 811-816.
139. Newton, C., et al., *Brain swelling and ischaemia in Kenyans with cerebral malaria.* Archives of disease in childhood, 1994. **70**(4): p. 281-287.
140. Mohanty, S., et al., *Magnetic resonance imaging of cerebral malaria patients reveals distinct pathogenetic processes in different parts of the brain.* MSphere, 2017. **2**(3): p. e00193-17.
141. Kim, E.M., et al., *Abdominal computed tomography findings of malaria infection with Plasmodium vivax.* The American journal of tropical medicine and hygiene, 2010. **83**(6): p. 1202.
142. Jang, J.Y., et al., *CT Findings of Malarial Spleens.* Journal of the Korean Society of Radiology, 2009. **61**(4): p. 241-247.
143. Bonnard, P., et al., *Splenic infarction during acute malaria.* Transactions of the Royal Society of Tropical Medicine and Hygiene, 2005. **99**(1): p. 82-86.
144. Kim, A., et al., *A case of symptomatic splenic infarction in vivax malaria.* The Korean journal of parasitology, 2007. **45**(1): p. 55.
145. Tonolini, M. and R. Bianco, *Nontraumatic splenic emergencies: cross-sectional imaging findings and triage.* Emergency radiology, 2013. **20**(4): p. 323-332.
146. Elzein, F., et al., *Pulmonary manifestation of Plasmodium falciparum malaria: Case reports and review of the literature.* Respiratory medicine case reports, 2017. **22**: p. 83-86.
147. Kawai, S., et al., *Enhancement of splenic glucose metabolism during acute malarial infection: correlation of findings of FDG-PET imaging with pathological changes in a primate model of severe human malaria.* The American journal of tropical medicine and hygiene, 2006. **74**(3): p. 353-360.

148. Sugiyama, M., et al., *Cerebral metabolic reduction in severe malaria: fluorodeoxyglucose-positron emission tomography imaging in a primate model of severe human malaria with cerebral involvement.* The American journal of tropical medicine and hygiene, 2004. **71**(5): p. 542-545.
149. Woodford, J., et al., *Positron emission tomography and magnetic resonance imaging in experimental human malaria to identify organ-specific changes in morphology and glucose metabolism: A prospective cohort study.* PLoS medicine, 2021. **18**(5): p. e1003567.
150. Pettersson, F., et al., *Whole-body imaging of sequestration of Plasmodium falciparum in the rat.* Infection and immunity, 2005. **73**(11): p. 7736-7746.
151. Zhang, Y., H. Hong, and W. Cai, *PET tracers based on Zirconium-89.* Current radiopharmaceuticals, 2011. **4**(2): p. 131-139.
152. Fu, R., et al., *Antibody fragment and affibody immunoPET imaging agents: Radiolabelling strategies and applications.* ChemMedChem, 2018. **13**(23): p. 2466-2478.
153. Kristensen, L.K., et al., *Site-specifically labeled 89Zr-DFO-trastuzumab improves immuno-reactivity and tumor uptake for immuno-PET in a subcutaneous HER2-positive xenograft mouse model.* Theranostics, 2019. **9**(15): p. 4409.
154. Wei, W., et al., *ImmunoPET: Concept, Design, and Applications.* Chemical Reviews, 2020. **120**(8): p. 3787-3851.
155. Dammes, N. and D. Peer, *Monoclonal antibody-based molecular imaging strategies and theranostic opportunities.* Theranostics, 2020. **10**(2): p. 938.
156. Vermeulen, K., et al. *Design and challenges of radiopharmaceuticals*. in *Seminars in nuclear medicine*. 2019. Elsevier.
157. Sarko, D., et al., *Bifunctional chelators in the design and application of radiopharmaceuticals for oncological diseases.* Current medicinal chemistry, 2012. **19**(17): p. 2667-2688.
158. Van de Voorde, M., et al., *Radiochemical processing of nuclear-reactor-produced radiolanthanides for medical applications.* Coordination Chemistry Reviews, 2019. **382**: p. 103-125.
159. Schroeder Jr, H.W. and L. Cavacini, *Structure and function of immunoglobulins.* Journal of Allergy and Clinical Immunology, 2010. **125**(2): p. S41-S52.
160. Holliger, P. and P.J. Hudson, *Engineered antibody fragments and the rise of single domains.* Nature biotechnology, 2005. **23**(9): p. 1126-1136.
161. Roopenian, D.C. and S. Akilesh, *FcRn: the neonatal Fc receptor comes of age.* Nature reviews immunology, 2007. **7**(9): p. 715-725.
162. Monnier, P.P., R.J. Vigouroux, and N.G. Tassew, *In vivo applications of single chain Fv (variable domain)(scFv) fragments.* Antibodies, 2013. **2**(2): p. 193-208.
163. Dewulf, J., et al., *Development of Antibody Immuno-PET/SPECT Radiopharmaceuticals for Imaging of Oncological Disorders—An Update.* Cancers, 2020. **12**(7): p. 1868.
164. Xenaki, K.T., S. Oliveira, and P.M. van Bergen En Henegouwen, *Antibody or antibody fragments: implications for molecular imaging and targeted therapy of solid tumors.* Frontiers in immunology, 2017. **8**: p. 1287.
165. Henrich, T.J., P.Y. Hsue, and H. VanBrocklin, *Seeing Is Believing: Nuclear Imaging of HIV Persistence.* Frontiers in Immunology, 2019. **10**: p. 2077.

166. Peltek, O.O., et al., *Current outlook on radionuclide delivery systems: from design consideration to translation into clinics.* Journal of nanobiotechnology, 2019. **17**(1): p. 1-34.
167. Roe, C.M., et al., *Alzheimer disease and cognitive reserve: variation of education effect with carbon 11–labeled Pittsburgh Compound B uptake.* Archives of neurology, 2008. **65**(11): p. 1467-1471.
168. Vlassenko, A.G. and M.E. Raichle, *Brain aerobic glycolysis functions and Alzheimer's disease.* Clinical and translational imaging, 2015. **3**(1): p. 27-37.
169. Baron, J.-C. and T. Jones, *Oxygen metabolism, oxygen extraction and positron emission tomography: historical perspective and impact on basic and clinical neuroscience.* Neuroimage, 2012. **61**(2): p. 492-504.
170. Motta-Ribeiro, G.C., et al., *Deterioration of regional lung strain and inflammation during early lung injury.* American journal of respiratory and critical care medicine, 2018. **198**(7): p. 891-902.
171. Cornelis, F.H., et al., *Long–Half-Life 89Zr-Labeled Radiotracers Can Guide Percutaneous Biopsy Within the PET/CT Suite Without Reinjection of Radiotracer.* Journal of Nuclear Medicine, 2018. **59**(3): p. 399-402.
172. Asiedu, K.O., et al., *Bone marrow cell trafficking analyzed by 89Zr-oxine positron emission tomography in a murine transplantation model.* Clinical Cancer Research, 2017. **23**(11): p. 2759-2768.
173. Truillet, C., et al., *Noninvasive measurement of mTORC1 signaling with 89Zr-transferrin.* Clinical Cancer Research, 2017. **23**(12): p. 3045-3052.
174. Dietlein, F., et al., *An 89Zr-labeled PSMA tracer for PET/CT imaging of prostate cancer patients.* Journal of Nuclear Medicine, 2021.
175. Matthews, P.M., et al., *Positron emission tomography molecular imaging for drug development.* British journal of clinical pharmacology, 2012. **73**(2): p. 175-186.
176. *Proceedings of the World Molecular Imaging Congress 2016, New York, New York, September 7-10, 2016: General Abstracts.* Molecular Imaging and Biology, 2016. **18**(2): p. 1-1278.
177. Signore, A., et al., *Immuno-imaging to predict treatment response in infection, inflammation and oncology.* Journal of clinical medicine, 2019. **8**(5): p. 681.
178. Bailly, C., et al., *Immuno-PET for clinical theranostic approaches.* International journal of molecular sciences, 2017. **18**(1): p. 57.
179. Rolle, A.-M., et al., *ImmunoPET/MR imaging allows specific detection of Aspergillus fumigatus lung infection in vivo.* Proceedings of the National Academy of Sciences, 2016. **113**(8): p. E1026-E1033.
180. Santangelo, P.J., et al., *Whole-body immunoPET reveals active SIV dynamics in viremic and antiretroviral therapy–treated macaques.* Nature methods, 2015. **12**(5): p. 427-432.
181. Wiehr, S., et al., *New pathogen-specific immunoPET/MR tracer for molecular imaging of a systemic bacterial infection.* Oncotarget, 2016. **7**(10): p. 10990.
182. Duvenhage, J., et al., *Molecular imaging of a zirconium-89 labeled antibody targeting Plasmodium falciparum–infected human erythrocytes.* Molecular Imaging and Biology, 2020. **22**(1): p. 115-123.
183. Tan, J., et al., *A LAIR1 insertion generates broadly reactive antibodies against malaria variant antigens.* Nature, 2016. **529**(7584): p. 105-109.
184. Holland, J.P., et al., *89Zr-DFO-J591 for immunoPET of prostate-specific membrane antigen expression in vivo.* Journal of Nuclear Medicine, 2010. **51**(8): p. 1293-1300.

185. Vosjan, M.J., et al., *Conjugation and radiolabeling of monoclonal antibodies with zirconium-89 for PET imaging using the bifunctional chelate p-isothiocyanatobenzyl-desferrioxamine.* Nature protocols, 2010. **5**(4): p. 739-743.
186. Deri, M.A., et al., *PET imaging with 89Zr: from radiochemistry to the clinic.* Nuclear medicine and biology, 2013. **40**(1): p. 3-14.
187. Raavé, R., et al., *Direct comparison of the in vitro and in vivo stability of DFO, DFO* and DFOcyclo* for 89 Zr-immunoPET.* European journal of nuclear medicine and molecular imaging, 2019. **46**(9): p. 1966-1977.
188. Wooten, A., et al., *Routine production of 89Zr using an automated module.* Applied Sciences, 2013. **3**(3): p. 593-613.
189. Pandit-Taskar, N., et al., *First-in-human imaging with 89Zr-Df-IAB2M anti-PSMA minibody in patients with metastatic prostate cancer: pharmacokinetics, biodistribution, dosimetry, and lesion uptake.* Journal of Nuclear Medicine, 2016. **57**(12): p. 1858-1864.
190. Viola-Villegas, N.T., et al., *Noninvasive imaging of PSMA in prostate tumors with 89Zr-labeled huJ591 engineered antibody fragments: the faster alternatives.* Molecular pharmaceutics, 2014. **11**(11): p. 3965-3973.
191. La, M.T., V.H. Tran, and H.-K. Kim, *Progress of coordination and utilization of Zirconium-89 for positron emission tomography (PET) studies.* Nuclear medicine and molecular imaging, 2019. **53**(2): p. 115-124.
192. Fischer, G., et al., *89Zr, a radiometal nuclide with high potential for molecular imaging with PET: chemistry, applications and remaining challenges.* Molecules, 2013. **18**(6): p. 6469-6490.
193. Beckman, R.A., L.M. Weiner, and H.M. Davis, *Antibody constructs in cancer therapy: protein engineering strategies to improve exposure in solid tumors.* Cancer, 2007. **109**(2): p. 170-179.
194. Duncan, J.R., T.M. Behr, and S.J. DeNardo, *Intracellular fate of radiometals.* The Journal of Nuclear Medicine, 1997. **38**(5): p. 829.
195. Tsai, S., et al., *Metabolism and renal clearance of 111In-labeled DOTA-conjugated antibody fragments.* Bioconjugate chemistry, 2001. **12**(2): p. 264-270.
196. Duncan, J.R., T.M. Behr, and S.J. DeNardo, *Intracellular fate of radiometals.* Journal of Nuclear Medicine, 1997. **38**(5): p. 829-829.
197. Suzuki, C., et al., *Preferential cleavage of a tripeptide linkage by enzymes on renal brush border membrane to reduce renal radioactivity levels of radiolabeled antibody fragments.* Journal of medicinal chemistry, 2018. **61**(12): p. 5257-5268.
198. Xiong, C., et al., *Metformin reduces renal uptake of radiotracers and protects kidneys from radiation-induced damage.* Molecular pharmaceutics, 2019. **16**(2): p. 808-815.
199. Ekblad, T., et al., *Development and preclinical characterisation of 99m Tc-labelled Affibody molecules with reduced renal uptake.* European journal of nuclear medicine and molecular imaging, 2008. **35**(12): p. 2245-2255.
200. Adumeau, P., et al., *Site-specifically labeled immunoconjugates for molecular imaging—part 1: cysteine residues and glycans.* Molecular imaging and biology, 2016. **18**(1): p. 1-17.
201. Zaroff, S. and G. Tan, *Hybridoma technology: the preferred method for monoclonal antibody generation for in vivo applications*. 2019, Future Science.

202. Ahmad, Z.A., et al., *scFv antibody: principles and clinical application.* Clinical and developmental immunology, 2012. **2012**.
203. Bates, A. and C.A. Power, *David vs. Goliath: the structure, function, and clinical prospects of antibody fragments.* Antibodies, 2019. **8**(2): p. 28.
204. Kobayashi, N., et al., *Toward in vivo imaging of heart disease using a radiolabeled single-chain Fv fragment targeting tenascin-C.* Analytical chemistry, 2011. **83**(23): p. 9123-9130.
205. Lu, R.-M., et al., *Single chain anti-c-Met antibody conjugated nanoparticles for in vivo tumor-targeted imaging and drug delivery.* Biomaterials, 2011. **32**(12): p. 3265-3274.
206. Mullen, L.M., et al., *Phage display in the study of infectious diseases.* Trends in microbiology, 2006. **14**(3): p. 141-147.
207. Benedek, O., et al., *Identification of laminin-binding motifs of Yersinia pestis plasminogen activator by phage display.* International journal of medical microbiology, 2005. **295**(2): p. 87-98.
208. Tohidkia, M.R., et al., *Molecular considerations for development of phage antibody libraries.* Journal of drug targeting, 2012. **20**(3): p. 195-208.
209. Ledsgaard, L., et al., *Basics of antibody phage display technology.* Toxins, 2018. **10**(6): p. 236.
210. Rami, A., et al., *An overview on application of phage display technique in immunological studies.* Asian Pacific Journal of Tropical Biomedicine, 2017. **7**(7): p. 599-602.
211. Frei, J. and J. Lai, *Protein and antibody engineering by phage display.* Methods in enzymology, 2016. **580**: p. 45-87.
212. Koivunen, E., et al., *Identification of receptor ligands with phage display peptide libraries.* Journal of Nuclear Medicine, 1999. **40**(5): p. 883-888.
213. Van Wyngaardt, W., et al., *A large semi-synthetic single-chain Fv phage display library based on chicken immunoglobulin genes.* BMC biotechnology, 2004. **4**(1): p. 6.
214. Arbabi Ghahroudi, M., et al., *Selection and identification of single domain antibody fragments from camel heavy-chain antibodies.* FEBS letters, 1997. **414**(3): p. 521-526.
215. O'Brien, P., et al., *Generation of native bovine mAbs by phage display.* Proceedings of the National Academy of Sciences, 1999. **96**(2): p. 640-645.
216. Li, Y., J. Kilpatrick, and G.C. Whitelam, *Sheep monoclonal antibody fragments generated using a phage display system.* Journal of immunological methods, 2000. **236**(1-2): p. 133-146.
217. Adda, C.G., et al., *Isolation of peptides that mimic epitopes on a malarial antigen from random peptide libraries displayed on phage.* Infection and immunity, 1999. **67**(9): p. 4679-4688.
218. Cheng, X.-J., et al., *Production of high-affinity human monoclonal antibody fab fragments to the 19-kilodalton C-terminal merozoite surface protein 1 of Plasmodium falciparum.* Infection and immunity, 2007. **75**(7): p. 3614-3620.
219. Keizer, D.W., et al., *Structures of phage-display peptides that bind to the malarial surface protein, apical membrane antigen 1, and block erythrocyte invasion.* Biochemistry, 2003. **42**(33): p. 9915-9923.
220. Kim, S.-H., et al., *Single-chain antibody fragment specific for Plasmodium vivax Duffy binding protein.* Clinical and Vaccine Immunology, 2007. **14**(6): p. 726-731.

221. Eda, K., S. Eda, and I.W. Sherman, *Identification of peptides targeting the surface of Plasmodium falciparum-infected erythrocytes using a phage display peptide library.* The American journal of tropical medicine and hygiene, 2004. **71**(2): p. 190-195.
222. Foord, A.J., et al., *Production and application of recombinant antibodies to foot-and-mouth disease virus non-structural protein 3ABC.* Journal of immunological methods, 2007. **321**(1-2): p. 142-151.
223. Wemmer, S., et al., *Chicken scFvs and bivalent scFv-CH fusions directed against HSP65 of Mycobacterium bovis.* Biologicals, 2010. **38**(3): p. 407-414.
224. Fehrsen, J., et al., *Serogroup-reactive and type-specific detection of bluetongue virus antibodies using chicken scFvs in inhibition ELISAs.* Journal of virological methods, 2005. **129**(1): p. 31-39.
225. Trager, W. and J.B. Jensen, *Human malaria parasites in continuous culture.* Science, 1976. **193**(4254): p. 673-675.
226. Lambros, C. and J.P. Vanderberg, *Synchronization of Plasmodium falciparum erythrocytic stages in culture.* The Journal of parasitology, 1979: p. 418-420.
227. Coronado, L.M., et al., *Separation of Plasmodium falciparum late stage-infected erythrocytes by magnetic means.* Journal of visualized experiments: JoVE, 2013(73).
228. Mata-Cantero, L., et al., *Magnetic isolation of Plasmodium falciparum schizonts iRBCs to generate a high parasitaemia and synchronized in vitro culture.* Malaria journal, 2014. **13**(1): p. 1-9.
229. Fahr, W. and A. Frenzel, *Phage Display and Selections on Cells*, in *Phage Display*. 2018, Springer. p. 321-330.
230. Hust, M., et al., *Improved microtitre plate production of single chain Fv fragments in Escherichia coli.* New Biotechnology, 2009. **25**(6): p. 424-428.
231. Tohidkia, M.R., et al., *Improved soluble ScFv ELISA screening approach for antibody discovery using phage display technology.* SLAS DISCOVERY: Advancing Life Sciences R&D, 2017. **22**(8): p. 1026-1034.
232. Rakabe, M., W. Van Wyngaardt, and J. Fehrsen, *Chicken single-chain antibody fragments directed against recombinant VP7 of bluetongue virus.* Food and agricultural immunology, 2011. **22**(3): p. 283-295.
233. Ch'ng, A.C.W., et al., *A high-throughput magnetic nanoparticle-based semi-automated antibody phage display biopanning*, in *Human Monoclonal Antibodies*. 2019, Springer. p. 377-400.
234. Reyna-Bello, A., M.C. Eleizalde, and A.M. Silva, *Assessment of Chromogen Suitability in ELISA for the Detection of Anaplasmosis and Trypanosomosis.* Journal of immunoassay & immunochemistry, 2007. **28**(1): p. 1-11.
235. Nikfarjam, S., et al., *Successful application of whole cell panning for isolation of phage antibody fragments specific to differentiated gastric cancer cells.* Advanced pharmaceutical bulletin, 2019. **9**(4): p. 624.
236. Schirrmann, T., et al., *Phage display for the generation of antibodies for proteome research, diagnostics and therapy.* Molecules, 2011. **16**(1): p. 412-426.
237. Reiersen, H., et al., *Screening human antibody libraries against carcinoma cells by affinity purification and polymerase chain reaction.* Journal of immunological methods, 2008. **330**(1-2): p. 44-56.
238. Noronha, E.J., et al., *Limited diversity of human scFv fragments isolated by panning a synthetic phage-display scFv library with cultured human melanoma cells.* The Journal of Immunology, 1998. **161**(6): p. 2968-2976.

239. Hans, R., et al., *Development and validation of immunoassay for whole cell detection of Brucella abortus and Brucella melitensis.* Scientific reports, 2020. **10**(1): p. 1-13.
240. Heitner, T., et al., *Selection of cell binding and internalizing epidermal growth factor receptor antibodies from a phage display library.* Journal of immunological methods, 2001. **248**(1-2): p. 17-30.
241. Pouvelle, B., et al., *Direct access to serum macromolecules by intraerythrocytic malaria parasites.* Nature, 1991. **353**(6339): p. 73-75.
242. Lown, P.S. and B.J. Hackel, *Magnetic Bead-Immobilized Mammalian Cells Are Effective Targets to Enrich Ligand-Displaying Yeast.* ACS combinatorial science, 2020. **22**(5): p. 274-284.
243. Min, B., et al., *Semi-Automated Cell Panning for Efficient Isolation of FGFR3-Targeting Antibody.* International Journal of Molecular Sciences, 2021. **22**(12): p. 6240.
244. Zhang, P., et al., *Peptide-based nanoprobes for molecular imaging and disease diagnostics.* Chemical Society Reviews, 2018. **47**(10): p. 3490-3529.
245. Li, X., et al., *New frontiers in molecular imaging using peptide-based radiopharmaceuticals for prostate cancer.* Frontiers in Chemistry, 2020. **8**: p. 1106.
246. Lee, S., J. Xie, and X. Chen, *Peptide-based probes for targeted molecular imaging.* Biochemistry, 2010. **49**(7): p. 1364-1376.
247. Okarvi, S.M., *Peptide-based radiopharmaceuticals: Future tools for diagnostic imaging of cancers and other diseases.* Medicinal research reviews, 2004. **24**(3): p. 357-397.
248. Rautenbach, M., et al., *Inhibition of malaria parasite blood stages by tyrocidines, membrane-active cyclic peptide antibiotics from Bacillus brevis.* Biochimica et Biophysica Acta (BBA)-Biomembranes, 2007. **1768**(6): p. 1488-1497.
249. Sinha, S., et al., *Systematic review: insight into antimalarial peptide.* International Journal of Peptide Research and Therapeutics, 2016. **22**(3): p. 325-340.
250. Chaianantakul, N., et al., *Antimalarial effect of cell penetrating peptides derived from the junctional region of Plasmodium falciparum dihydrofolate reductase-thymidylate synthase.* Peptides, 2020. **131**: p. 170372.
251. Conroy, T., et al., *Total synthesis and antimalarial activity of symplostatin 4.* Organic letters, 2010. **12**(23): p. 5576-5579.
252. Torrent, M., et al., *Antimicrobial peptide action on parasites.* Current drug targets, 2012. **13**(9): p. 1138-1147.
253. Gelhaus, C., et al., *The antimicrobial peptide NK-2, the core region of mammalian NK-lysin, kills intraerythrocytic Plasmodium falciparum.* Antimicrobial agents and chemotherapy, 2008. **52**(5): p. 1713-1720.
254. Choi, S.-J., et al., *Isolation and characterization of Psalmopeotoxin I and II: two novel antimalarial peptides from the venom of the tarantula Psalmopoeus cambridgei.* FEBS letters, 2004. **572**(1-3): p. 109-117.
255. Mokaleng, B.B., et al., *Synthesis, 68Ga-radiolabeling, and preliminary in vivo assessment of a depsipeptide-derived compound as a potential PET/CT infection imaging agent.* BioMed research international, 2015. **2015**.
256. Rossouw, D.D. and W.A. Breeman, *Scaled-up radiolabelling of DOTATATE with 68Ga eluted from a SnO2-based 68Ge/68Ga generator.* Applied Radiation and Isotopes, 2012. **70**(1): p. 171-175.

257. Ebenhan, T., et al., *Peptide synthesis, characterization and 68Ga-radiolabeling of NOTA-conjugated ubiquicidin fragments for prospective infection imaging with PET/CT.* Nuclear medicine and biology, 2014. **41**(5): p. 390-400.
258. Adil, A.-N. and S. Fanti, *Radiolabelled peptides in diagnosis and therapy: an introduction*. 2012, Springer.
259. Fani, M., J.P. Andre, and H.R. Maecke, *68Ga-PET: a powerful generator-based alternative to cyclotron-based PET radiopharmaceuticals.* Contrast media & molecular imaging, 2008. **3**(2): p. 53-63.
260. Jackson, J.A., et al., *Bioconjugates of chelators with peptides and proteins in nuclear medicine: historical importance, current innovations, and future challenges.* Bioconjugate chemistry, 2020. **31**(3): p. 483-491.
261. Banerjee, S.R. and M.G. Pomper, *Clinical applications of Gallium-68.* Applied Radiation and Isotopes, 2013. **76**: p. 2-13.
262. Hennrich, U. and M. Benešová, *[68Ga] Ga-DOTA-TOC: the first FDA-approved 68Ga-radiopharmaceutical for PET imaging.* Pharmaceuticals, 2020. **13**(3): p. 38.
263. Tsionou, M.I., et al., *Comparison of macrocyclic and acyclic chelators for gallium-68 radiolabelling.* RSC advances, 2017. **7**(78): p. 49586-49599.
264. Wynendaele, E., et al., *Development of peptide and protein based radiopharmaceuticals.* Current pharmaceutical design, 2014. **20**(14): p. 2250-2267.
265. Okarvi, S., *Peptide-based radiopharmaceuticals and cytotoxic conjugates: potential tools against cancer.* Cancer treatment reviews, 2008. **34**(1): p. 13-26.
266. Koopmans, K. and A. Glaudemans, *Rationale for the use of radiolabelled peptides in diagnosis and therapy.* European journal of nuclear medicine and molecular imaging, 2012. **39**(1): p. 4-10.
267. Chen, C., et al., *Applicability of free drug hypothesis to drugs with good membrane permeability that are not efflux transporter substrates: A microdialysis study in rats.* Pharmacology research & perspectives, 2020. **8**(2): p. e00575.
268. Smith, D.A., L. Di, and E.H. Kerns, *The effect of plasma protein binding on in vivo efficacy: misconceptions in drug discovery.* Nature reviews Drug discovery, 2010. **9**(12): p. 929-939.
269. Di, L., K. Riccardi, and D. Tess, *Evolving approaches on measurements and applications of intracellular free drug concentration and Kpuu in drug discovery.* Expert Opinion on Drug Metabolism & Toxicology, 2021(just-accepted).
270. Trainor, G.L., *The importance of plasma protein binding in drug discovery.* Expert opinion on drug discovery, 2007. **2**(1): p. 51-64.
271. Chen, K., J. Xie, and X. Chen, *RGD-human serum albumin conjugates as efficient tumor targeting probes.* Molecular imaging, 2009. **8**(2): p. 7290.2009. 00011.
272. Jensen, A.R., Y. Adams, and L. Hviid, *Cerebral Plasmodium falciparum malaria: The role of PfEMP1 in its pathogenesis and immunity, and PfEMP1-based vaccines to prevent it.* Immunological reviews, 2020. **293**(1): p. 230-252.
273. Dondorp, A.M., et al., *The relationship between age and the manifestations of and mortality associated with severe malaria.* Clinical Infectious Diseases, 2008. **47**(2): p. 151-157.
274. Band, G., et al., *Imputation-based meta-analysis of severe malaria in three African populations.* PLoS genetics, 2013. **9**(5): p. e1003509.

275. Medana, I.M., et al., *Axonal injury in cerebral malaria.* The American journal of pathology, 2002. **160**(2): p. 655-666.
276. Milner Jr, D.A., et al., *Supraorbital postmortem brain sampling for definitive quantitative confirmation of cerebral sequestration of Plasmodium falciparum parasites.* Journal of Infectious Diseases, 2012. **205**(10): p. 1601-1606.
277. Shikani, H.J., et al., *Cerebral malaria: we have come a long way.* The American journal of pathology, 2012. **181**(5): p. 1484-1492.
278. Franke-Fayard, B., et al., *Murine malaria parasite sequestration: CD36 is the major receptor, but cerebral pathology is unlinked to sequestration.* Proceedings of the National Academy of Sciences, 2005. **102**(32): p. 11468-11473.
279. Cabrales, P., et al., *Murine cerebral malaria is associated with a vasospasm-like microcirculatory dysfunction, and survival upon rescue treatment is markedly increased by nimodipine.* The American journal of pathology, 2010. **176**(3): p. 1306-1315.
280. White, N.J., et al., *The murine cerebral malaria phenomenon.* Trends in parasitology, 2010. **26**(1): p. 11-15.
281. Ameri, M., *Laboratory diagnosis of malaria in nonhuman primates.* Veterinary clinical pathology, 2010. **39**(1): p. 5-19.
282. Pasini, E.M. and C.H. Kocken, *Parasite-host interaction and pathophysiology studies of the human relapsing malarias Plasmodium vivax and Plasmodium ovale infections in non-human primates.* Frontiers in Cellular and Infection Microbiology, 2020. **10**.
283. Joyner, C., J.W. Barnwell, and M.R. Galinski, *No more monkeying around: primate malaria model systems are key to understanding Plasmodium vivax liver-stage biology, hypnozoites, and relapses.* Frontiers in microbiology, 2015. **6**: p. 145.
284. Sun, X., et al., *Peptide-based imaging agents for cancer detection.* Advanced drug delivery reviews, 2017. **110**: p. 38-51.
285. Jain, S.K., *The promise of molecular imaging in the study and treatment of infectious diseases.* Molecular imaging and biology, 2017. **19**(3): p. 341-347.
286. Ebenhan, T., et al., *Preclinical evaluation of 68Ga-labeled 1, 4, 7-triazacyclononane-1, 4, 7-triacetic acid-ubiquicidin as a radioligand for PET infection imaging.* Journal of Nuclear Medicine, 2014. **55**(2): p. 308-314.
287. Cunnington, A.J., et al., *Comparison of parasite sequestration in uncomplicated and severe childhood Plasmodium falciparum malaria.* Journal of Infection, 2013. **67**(3): p. 220-230.
288. Haldar, K., et al., *Malaria: mechanisms of erythrocytic infection and pathological correlates of severe disease.* Annu. Rev. Pathol. Mech. Dis., 2007. **2**: p. 217-249.
289. Barrera, V., et al., *Neurovascular sequestration in paediatric P. falciparum malaria is visible clinically in the retina.* Elife, 2018. **7**: p. e32208.
290. Knop, J., et al., *Staphylococcus aureus infection in humanized mice: a new model to study pathogenicity associated with human immune response.* The Journal of infectious diseases, 2015. **212**(3): p. 435-444.
291. Denton, P.W. and J.V. Garcia, *Mucosal HIV-1 transmission and prevention strategies in BLT humanized mice.* Trends in microbiology, 2012. **20**(6): p. 268-274.

292. Melkus, M.W., et al., *Humanized mice mount specific adaptive and innate immune responses to EBV and TSST-1.* Nature medicine, 2006. **12**(11): p. 1316-1322.
293. Pardi, N., et al., *Administration of nucleoside-modified mRNA encoding broadly neutralizing antibody protects humanized mice from HIV-1 challenge.* Nature communications, 2017. **8**(1): p. 1-8.
294. England, C.G., et al., *89 Zr-labeled nivolumab for imaging of T-cell infiltration in a humanized murine model of lung cancer.* European journal of nuclear medicine and molecular imaging, 2018. **45**(1): p. 110-120.
295. Frias-Staheli, N., et al., *Utility of humanized BLT mice for analysis of dengue virus infection and antiviral drug testing.* Journal of virology, 2014. **88**(4): p. 2205-2218.
296. Ernst, W., *Humanized mice in infectious diseases.* Comparative immunology, microbiology and infectious diseases, 2016. **49**: p. 29-38.
297. Arnold, L., et al., *Analysis of innate defences against Plasmodium falciparum in immunodeficient mice.* Malaria journal, 2010. **9**(1): p. 1-12.
298. Jiménez-Díaz, M.B., et al., *Improved murine model of malaria using Plasmodium falciparum competent strains and non-myelodepleted NOD-scid IL2R γ null mice engrafted with human erythrocytes.* Antimicrobial agents and chemotherapy, 2009. **53**(10): p. 4533-4536.
299. Cunha, L., et al., *The role of molecular imaging in modern drug development.* Drug Discovery Today, 2014. **19**(7): p. 936-948.
300. Freise, A.C. and A.M. Wu, *In vivo imaging with antibodies and engineered fragments.* Molecular immunology, 2015. **67**(2): p. 142-152.
301. Tassew, N.G., et al., *Sustained in vivo inhibition of protein domains using single-chain Fv recombinant antibodies and its application to dissect RGMa activity on axonal outgrowth.* Journal of Neuroscience, 2009. **29**(4): p. 1126-1131.
302. Pasche, N., et al., *The antibody-based delivery of interleukin-12 to the tumor neovasculature eradicates murine models of cancer in combination with paclitaxel.* Clinical Cancer Research, 2012. **18**(15): p. 4092-4103.
303. Basu, K., et al., *Why recombinant antibodies—benefits and applications.* Current opinion in biotechnology, 2019. **60**: p. 153-158.
304. Diebolder, P., et al., *Preclinical Evaluation of an Engineered Single-Chain Fragment Variable-Fragment Crystallizable Targeting Human CD44.* Journal of Nuclear Medicine, 2021. **62**(1): p. 137-143.
305. Frigerio, B., et al., *Anti-PSMA 124 I-scFvD2B as a new immuno-PET tool for prostate cancer: preclinical proof of principle.* Journal of Experimental & Clinical Cancer Research, 2019. **38**(1): p. 1-8.
306. Nawaz, S., et al., *Simple, mild, one-step labelling of proteins with gallium-68 using a tris (hydroxypyridinone) bifunctional chelator: a 68 Ga-THP-scFv targeting the prostate-specific membrane antigen.* EJNMMI research, 2017. **7**(1): p. 1-9.
307. Malviya, G., et al., *Radiolabelled peptides and monoclonal antibodies for therapy decision making in inflammatory diseases.* Current pharmaceutical design, 2008. **14**(24): p. 2401-2414.
308. Lian, Z. and T. Ji, *Functional peptide-based drug delivery systems.* Journal of Materials Chemistry B, 2020. **8**(31): p. 6517-6529.

309. Baig, M.H., et al., *Peptide based therapeutics and their use for the treatment of neurodegenerative and other diseases.* Biomedicine & Pharmacotherapy, 2018. **103**: p. 574-581.
310. Wang, Y., et al., *Peptide–drug conjugates as effective prodrug strategies for targeted delivery.* Advanced drug delivery reviews, 2017. **110**: p. 112-126.
311. Aguiar, L., et al., *Coupling the antimalarial cell penetrating peptide TP10 to classical antimalarial drugs primaquine and chloroquine produces strongly hemolytic conjugates.* Molecules, 2019. **24**(24): p. 4559.
312. Efron, L., et al., *Direct interaction of dermaseptin S4 aminoheptanoyl derivative with intraerythrocytic malaria parasite leading to increased specific antiparasitic activity in culture.* Journal of Biological Chemistry, 2002. **277**(27): p. 24067-24072.
313. Stolze, S.C., et al., *The antimalarial natural product symplostatin 4 is a nanomolar inhibitor of the food vacuole falcipains.* Chemistry & biology, 2012. **19**(12): p. 1546-1555.
314. Krugliak, M., et al., *Antimalarial activities of dermaseptin S4 derivatives.* Antimicrobial agents and chemotherapy, 2000. **44**(9): p. 2442-2451.
315. Lesmes, L.P., et al., *A C-terminal cationic fragment derived from an arginine-rich peptide exhibits in vitro antibacterial and anti-plasmodial activities governed by its secondary structure properties.* Peptides, 2009. **30**(12): p. 2150-2160.
316. Kamya, M.R., et al., *Effect of HIV-1 infection on antimalarial treatment outcomes in Uganda: a population-based study.* The Journal of infectious diseases, 2006. **193**(1): p. 9-15.
317. Flateau, C., G. Le Loup, and G. Pialoux, *Consequences of HIV infection on malaria and therapeutic implications: a systematic review.* The Lancet infectious diseases, 2011. **11**(7): p. 541-556.
318. Chukwuanukwu, R.C., et al., *Modulation of the immune response to Mycobacterium tuberculosis during malaria/M. tuberculosis co-infection.* Clinical & Experimental Immunology, 2017. **187**(2): p. 259-268.
319. Simon, G., *Impacts of neglected tropical disease on incidence and progression of HIV/AIDS, tuberculosis, and malaria: scientific links.* International Journal of Infectious Diseases, 2016. **42**: p. 54-57.
320. Baluku, J.B., et al., *Prevalence of malaria and TB coinfection at a national tuberculosis treatment centre in Uganda.* Journal of tropical medicine, 2019. **2019**.
321. Lawn, S., *AIDS in Africa: the impact of coinfections on the pathogenesis of HIV-1 infection.* Journal of infection, 2004. **48**(1): p. 1-12.
322. Ter Kuile, F.O., et al., *The burden of co-infection with human immunodeficiency virus type 1 and malaria in pregnant women in sub-saharan Africa.* The American journal of tropical medicine and hygiene, 2004. **71**(2_suppl): p. 41-54.

Appendix

To quantitatively validate the PET/CT images and distribution of [^{89}Zr]Zr-Pf-Fab in the healthy BALB/c mice, systematic biodistribution studies were subsequently performed on various tissues/organs. After the final microPET/CT scan (24 h post-injection) the mice were euthanised and their organs/ tissues removed, weighed and the organ- or tissue-related activity was determined using an automated gamma counter (Hidex AMG, Turku, Finland). To evaluate the potential of [^{89}Zr]Zr-Pf-Fab as a malaria imaging agent, its accumulation in the selected organs were compared to the biodistribution of mice injected with [^{89}Zr]Zr-IIIB6 and [^{89}Zr]Zr-oxalate (Figure 2.10) [182] (Table A2).

Table A2. *P*-values determined by comparing organ uptake between healthy mice injected with [^{89}Zr]Zr-Pf-Fab, [^{89}Zr]Zr-IIIB6 (n=5) and [^{89}Zr]Zr-oxalate (n=4).

Organ	[^{89}Zr]Zr-Fab *vs*. [^{89}Zr]Zr-IIIB6	[^{89}Zr]Zr-Fab *vs*. [^{89}Zr]Zr-oxalate	[^{89}Zr]Zr-IIIB6 *vs*. [^{89}Zr]Zr-oxalate
Blood	0.4	1.2×10^{-5}	1.0×10^{-4}
Plasma	1.2×10^{-2}	6×10^{-2}	0.5
Heart	5×10^{-3}	9×10^{-7}	0.24
Lungs	2.3×10^{-2}	4×10^{-5}	0.6
Liver	5×10^{-2}	2.3×10^{-4}	0.4
Kidneys	1.1×10^{-4}	1.0×10^{-3}	0.18
Spleen	1.2×10^{-2}	2.3×10^{-5}	0.12
Stomach	7.0×10^{-5}	1.4×10^{-2}	1.6×10^{-3}
Small intestine	4×10^{-3}	1.9×10^{-5}	0.1
Large intestine	4×10^{-5}	8×10^{-4}	0.1
Muscle	8×10^{-2}	6×10^{-4}	0.6
Femur	1.0×10^{-2}	8×10^{-6}	1.2×10^{-5}
Bladder	0.11	4×10^{-4}	0.29
Reproductive organs	5.6×10^{-5}	2.2×10^{-5}	0.6
Skin	1.4×10^{-2}	2.0×10^{-7}	8×10^{-4}

Footnotes: Following activity corrections for background and radioactive decay (standards were used to inter calibrate the two sets of equipment), the results were expressed in relation to the injected dose (ID) and adjusted for organ weight (% ID/g). Organ uptake was compared between all-time points and considered statistically significant if paired Student-t tests returned a *P*-value <0.05